UNIVERSITÀ
DEGLI STUDI
FIRENZE

PhD in
Earth Science

CYCLE XXXIII

COORDINATOR Prof. Lorella Francalanci

SEISMIC INTERFEROMETRY AND VOLCANIC TREMOR LINKED TO EXPLOSIVE REGIMES

Doctoral Candidate

Dr. Lorenzo Innocenti

Supervisor

Prof. Maurizio Ripepe

Coordinator

Prof. Lorella Francalanci

Years 2017/2020

TABLE OF CONTENTS

LIST OF FIGURES

LIST OT TABLES

AKNOWLEDGMENTS

Alla mia famiglia, presente e futura, per aver creduto in me ed avermi sempre incoraggiato.

Ad Elena, senza la quale tutto, compreso questo, non sarebbe possibile.

ABSTRACT

The ability to measure in real-time information on changes of the elastic properties of the medium or on location of the seismic signal source are key parameters to forecast active ongoing processes. Cross-correlating seismic signals recorded at two stations is possible to retrieve Green's function. Depending on which part of seismic signal is analysed, the early part or the coda, it represents position of the source originating waves or elastic characteristics of the medium through which the seismic wave propagates.

Here I propose the methodology based on deconvolution technique to retrieve the Green's function. Results have been compared with other geophysical dataset in order to infer information on volcano dynamic showing a strong correlation with seasonal variations due to atmospheric temperature. This can be explained as due to partial changes in seismic velocity induced by the ambient temperature affecting the shallower layers. The strong correlation between interferometry and ambient temperature is a strong evidence of the high sensibility and reliability of the developed technique. Once this long-term effect has been removed, I correlate interferometric changes to volcanic activity and other geophysical parameters. The interferometry changes have been then filtered in two different frequency band which seem to be the best to perform evaluations of source position and medium characteristics variations at Stromboli volcano. According also to previous studies, given the recurrence of VLP signals in the seismic record, the delay-time and noise-coda waves on both frequency bands are strongly affected by local seismicity. Changes in the time lags between the green's functions are more reflecting changes in the delay times between the seismic events rather than changes in seismic velocity. In this case, interferometric analysis is rather reflecting changes in the position of the source. Interferometry shows in fact a very good correlation with changes in the polarization dip of the seismic VLP, revealing a strong link to changes in relative position of the seismic VLP source. In the second instance, no clear evidence of substantial medium variations in all analysed time period have been found.

Volcanic seismic tremor is a persistent ground vibration due to interaction between solid earth, atmosphere and hydrosphere. It consists of both volume waves and surface waves generated by movements of fluids, either gas or magma. Due to correlation to fluid dynamics of the volcano, seismic tremor seems to be an efficient tool for understanding the dynamics of the plumbing system. I have developed a new method to analyse seismic tremor by calculating the temporal periodicity of RMS amplitude variations using a Zero-crossing technique. Analysis of frequency of tremor amplitude show sudden and clear increases close to phases of intense activity related to major gas releases. In particular the tremor switched from harmonic to pulsating-spasmodic, with large amplitude variations about 10 days before the two paroxysms which occurred on 3 of July 2019 and 28 August 2019. This behaviour probably depends on magma flow and suggest that this technique can be a valuable predictor of intense eruptions.

I extended both interferometry and tremor analysis over a 4 years long dataset on 5 seismic stations. I analysed and compared results with other available geophysical datasets like seismic VLP signals and acoustic pressure of explosions.

1. INTRODUCTION

Explosive eruptions are a major source of hazard (Self, 2006). Unlike for other natural phenomena, such as landslide or other gravity driven phenomena, the volcanic risk can only partially be minimized by a careful use of the territory, with the definition of restricted areas. Indeed, many active volcanoes are highly populated areas, with > 5 Millions of people living on the flanks of active volcanoes worldwide, that could be affected by direct material fall out as well as gravity currents induced by the eruption such as pyroclastic flows or lahars. Moreover, volcanic activity can resume at quiescent volcanoes unexpectedly and even after hundreds of years, possibly affecting inhabited areas.

According to the different level of volcanic activity the risk related to volcanoes can be different involving different problems for our society. Effusive eruptions spreading lava flows over areas up to hundreds of squared kilometres are able to completely destroy local settlements and infrastructures but the risk of loss of life is small. Volcanic explosive eruptions can inject in the atmosphere millions of cubic meters of ash, gases and debris: their dispersal has impacted in several instances life on Earth. Moreover, ahead of the massive atmospheric ash injection, large volcanic plumes can collapse driving pyroclastic density currents (PDCs) down the volcano's flanks that are among the most hazardous volcanic processes, able to produce total destruction and death at several kilometres around the volcanic edifice (Cole, et al., 2015).

For this reason, volcano surveillance is often the only solution to reduce the risk and dedicated volcano monitoring has experienced a strong increase in the last decades worldwide, with the aim to detect precursors of eruptive activity that might allow the prompt evacuation of inhabitants of possibly affected areas. It is clear how the response of civil protection and decision-making agencies is strongly dependent on the knowledge of ongoing processes at an eruptive volcano and for this reason monitoring networks, techniques and procedures have been exponentially improving in the last few decades.

Among the different geophysical signals produced by volcanic activity, seismic signal is the most efficient precursor, being directly related to processes acting in the solid earth (Einarsson, 2018). An increased number of VT earthquakes is a clear indication of magma movement that is possibly leading to an eruption. At Kelud volcano, in Indonesia, more than 100000 people were evacuated after the onset of seismic activity before the February 14, 2014 eruption. This allowed to dramatically reduce the effect of the eruption that caused the death of only 7 people, despite the shockwave was felt up to 180 km from the volcano and up to 5 cm ash up to 200 km from the vent (Wunderman, 2014).

At open conduit system seismic analysis can reveal transition in the source mechanisms and therefore being used to identify periods of increased hazard. At Stromboli volcano, for example, VT activity is very limited (Gambino & Scaltrito, 2018) and, despite clearly suggesting a deep magma movement leading possibly to an increased hazard, its applicability is very limited. Nevertheless, continuous seismic monitoring is performed and allows to track the position of the seismic source of VLP events (Ripepe, et al., 2015; Valade, et al., 2016) produced by explosive dynamics and to monitor time variation of volcanic tremor. These were used to define a conceptual model of

explosive dynamics at Stromboli (Ripepe, et al., 2005) and are used routinely for volcano hazard assessments. Here increased explosive activity at Stromboli volcano, is considered as a possible precursor of eruptive activity and hence also to paroxysmal events (Ripepe, et al., 2015) that represent the higher risk at Stromboli. However, the most recent paroxysms at Stromboli volcano occurred without any clearly evident precursors (Ripepe, et al., in press), highlighting the need for new monitoring approaches. Indeed, any additional information on the characteristics of the source mechanisms or on the stress field possibly reflected by the seismic velocity structure of the volcanic edifice (Haney, et al., 2014) is useful to improve our understanding of the volcanic dynamics at open vent volcanoes and to consequently improve hazard assessments.

This thesis aims to specifically address this topic and investigate new approaches of the analysis of seismic signals at Stromboli to possibly identify transitions between regimes of different explosive levels. I investigated the use of seismic interferometry, and its ability to provide information of a changing source process or a changing propagation medium. In particular I developed an algorithm with Matlab to evaluate time variation of the green function at Stromboli volcano and compared them with other seismological evidences of migration of the position of the seismic sources. Moreover, I carefully investigated volcanic tremor, by developing new algorithm, and compared that with the occurrence of the 2019 paroxysms.

In Chapter 2, I first introduce Stromboli volcano, its typical activity and most hazardous paroxysmal events that represent the major source of risks for tourists that daily used to visit the summit craters. Here I also describe in detail the main features of seismic signals recorded at Stromboli volcano, that consists both on VLP seismic transients produced by discrete explosive events and sustained volcanic tremor produced by persistent degassing activity.

In Chapter 3, I investigate seismic interferometry and its possible applications in volcanic environments. Here I present in detail an algorithm developed in Matlab specifically in my PhD research project and compare that with the freely available MSNoise. To test and validated the Matlab algorithm, I applied that on a different dataset, collected at Misti volcano.

In Chapter 4, I apply interferometric analysis on 4 years of seismic data collected at Stromboli volcano by considering all couple of stations from a 6 stations seismic network and present trends and time variations of the obtained Green Functions. I also present an analysis of volcanic tremor able to highlight the time variation of tremor fluctuations.

In Chapter 5, the main findings at Stromboli volcano are discussed. In particular I found that results from the seismic interferometry analysis, that is affected by external temperature, is nicely matching the position of the VLP seismic source, as shown by the polarization ellipsoid of the VLP 3 component ground displacement, suggesting how this procedure might be used to track changes of the explosive source position. Encouraging results are obtained with the newly developed analysis of volcanic tremor, that is showing a clear increase before the paroxysms clearly suggesting a change in the degassing regime preceding the hazardous events.

Despite still open questions remain, results achieved during my PhD research project and summarized in this thesis open new perspective for seismic monitoring at open conduit active volcanoes, that might provide at Stromboli and possibly at volcanoes sharing a similar dynamics new information for a batter risk assessment.

2. STROMBOLI VOLCANO

2.1. GEOLOGICAL AND VOLCANOLOGICAL OUTLINES

Stromboli volcano is the northernmost island of the Aeolian archipelago in the southern Tyrrenian Sea (Figure 1). The tectonic setting of the area is related to the plate convergence regime between Africa and Europe (Goes, et al., 2004), and consists of a complex conjunction of three main sectors associated with transgressive and extensional regimes (Ventura, 2013).

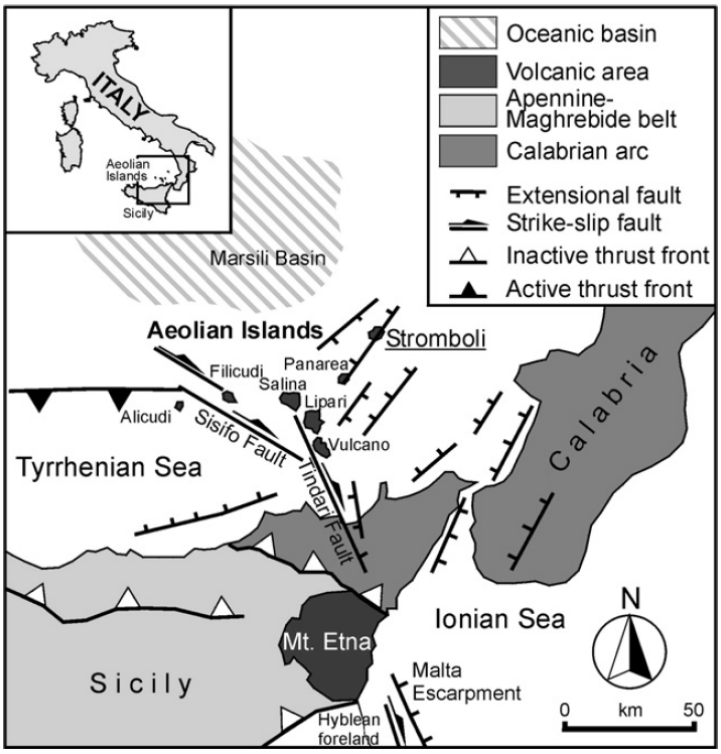

Figure 1. Location of the Stromboli volcano within the Aeolian archipelago in the southern Tyrrhenian Sea, and main tectonic features of the area. From Corazzato, et al., 2008.

The western sector (Alicudi and Filicudi islands) is characterized by an ongoing compressional dynamic, whereas the eastern sector (Panarea and Stromboli islands) is characterized by extensional dynamics related to the rapidly extending Marsili oceanic basin and the south-eastward migration of the Calabrian arc. The central sector (Vulcano, Lipari and Salina islands) is interpreted as "the transfer zone" between the above described compressional and extensional domains (Ventura, 2013). Recent active volcanism concentrated along a NNW-SSE lithospheric discontinuity is related to continental rift magmatism promoted by the mantle upwelling that started about 1 My ago (De Astis, et al., 2003; Ventura, 2013).

The island of Stromboli belongs to a late Quaternary, NE-SW trending large volcanic structure consisting of basalts, basaltic-andesites and andesites (Francalanci, et al., 1999). This complex includes a small island located northeast (Strombolicchio), and a submerged centre located to the south (Cavoni) from the main Stromboli edifice (Hornig-Kjarsgaard, et al., 1993). Stromboli is a composite large volcanic edifice about 120 ky old that rise for a total height of about 3200 m above the basin floor, with a subaerial tip 924 m height above sea level (Gillot & Keller, 1993; Kokelaar & Romagnoli, 1995). It was formed by building and destructive phases that involved several volcanic edifices during six main periods of activity. The lithostratigraphic units emplaced during these periods are: 1) Paleostromboli I (Cavoni synthem); 2) Paleostromboli II (Gramigna synthem); 3) Paleostromboli III (Gramigna synthem); 4) Lower, Middle and Upper Vancori (Frontone and Vancori synthems); 5) Neostromboli (Fossetta synthem); 6) Recent Stromboli (Pizzo, Fili di Baraona and Sciara synthems) (Rosi, 1980; Francalanci, 1987; Hornig-Kjarsgaard, et al., 1993; Pasquarè, et al., 1993). These volcanic units are reported in figure (Figure 2).

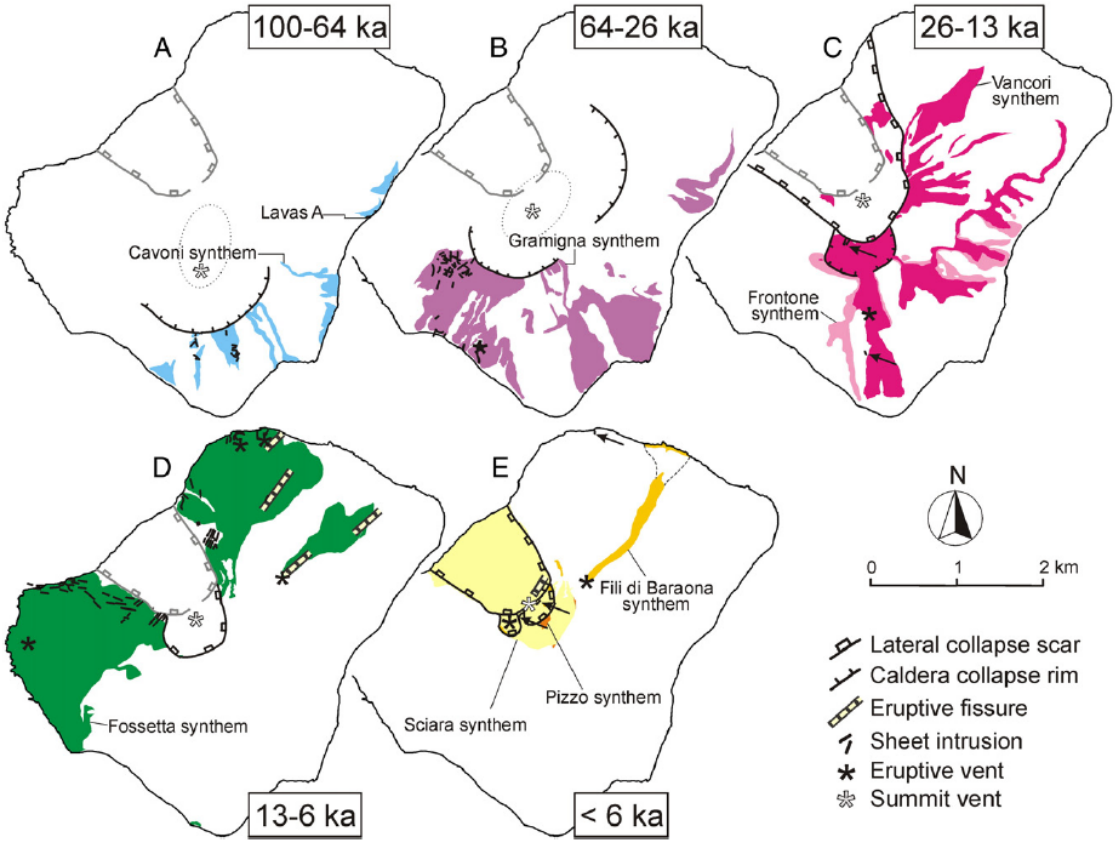

Figure 2. Reconstruction of the different sheet intrusion phases and their space distribution, from (Corazzato, et al., 2008). The present Sciara del Fuoco scar is reported for spatial reference at each stage. Area of outcrop of the volcanic products belonging to the related synthem is reported for each stage. (A) During the Paleostromboli I period (85 – 64 ka), sheets intruded into the Cavoni synthem rocks along the southern outer flank of the Paleostromboli I caldera rim. (B) At the end of the Paleostromboli II and III periods (64 – 26 ka), sheet intrusions cut the Gramigna synthem volcanics and concentrated in the Vallone di Rina area, showing the prevailing NE–SW and subordinate N–S tectonic control on the shallow magmatic system. (C) During the Vancori period (26 – 13 ka), sheet intrusions into Frontone and Vancori synthems are poorly exposed, but again show the NE and N-trending directions. (D) After the paleo-Sciara del Fuoco lateral collapse at the end of the Vancori period (13 ka), sheets intruded the Neostromboli edifice (Fossetta synthem, 13 – 6 ka) striking parallel to the collapse scar and to the NE-striking regional tectonic trend. Several NE-trending eruptive fissures affected the north-eastern flank of the Neostromboli cone. (E) The Recent Stromboli period (Pizzo, Fili di Baraona and Sciara synthems; (< 6 ka) is characterized by a shallow NE-striking intrusion activity feeding the summit vents. Few lateral eruptive vents in the north-eastern flank are also present.

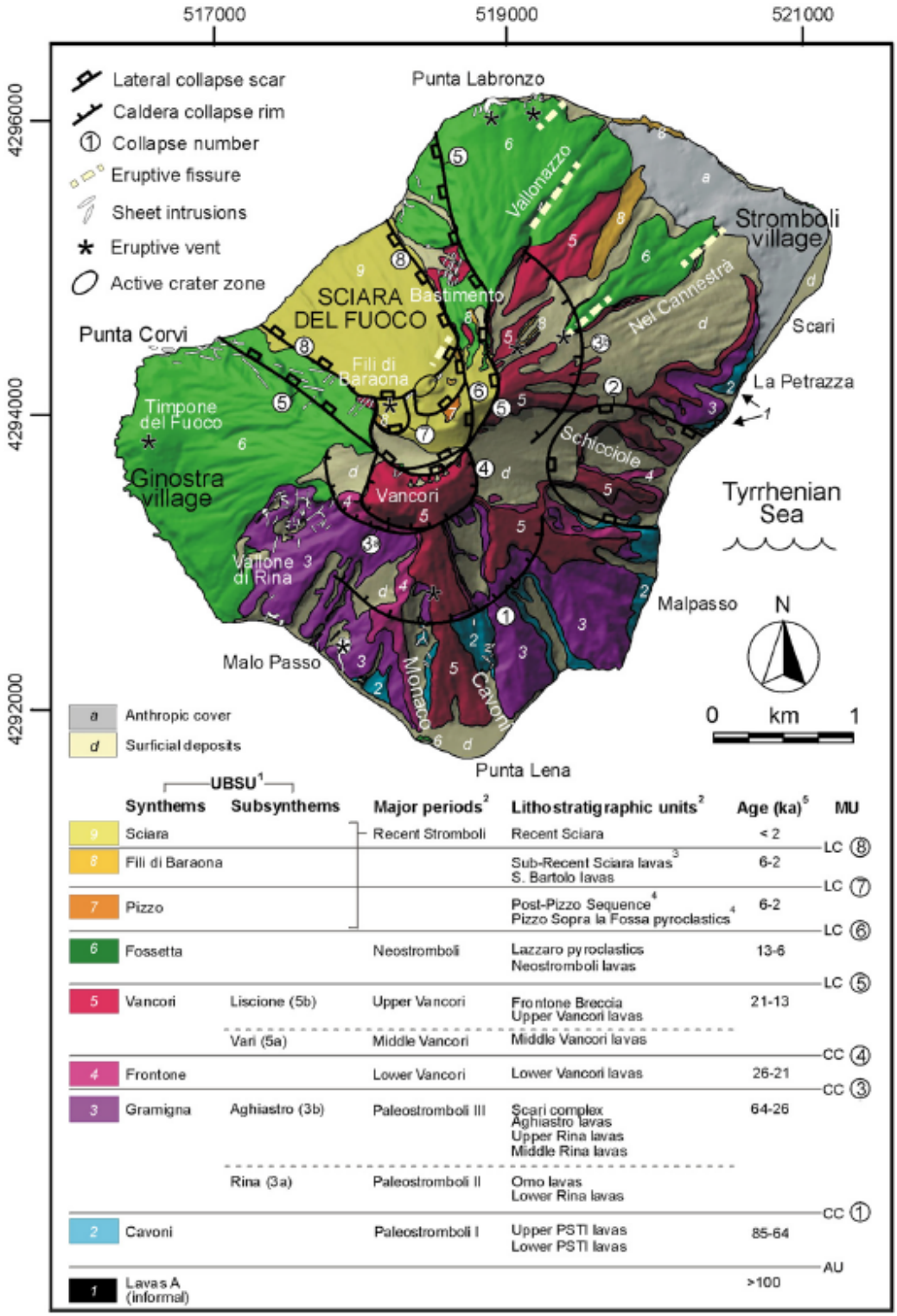

Figure 3. Simplified geologic map of Stromboli island showing the main stratigraphic units (UBSU, based on (Tibaldi, et al., 2009), *with indication of caldera and sector collapse traces, sheet intrusions, eruptive fissures and vents. UTM coordinates in meters.*

A simplified geological map (Tibaldi, et al., 2009) is reported in figure (Figure 3) where synthems and periods are correlated with lithostratigraphic units and age. During the last 100 ky, Stromboli volcano has experienced eight caldera and lateral collapse episodes that have caused structural modifications (Pasquarè, et al., 1993; Tibaldi, et al., 1994; Tibaldi, 2001), as well as changes in the

location of volcanic centres, in its magma compositions (Francalanci, 1987; Francalanci, et al., 1989; Francalanci, et al., 1993) and activity. Summit vertical collapses of caldera type have predominantly characterized the earlier stages of evolution, while in the past 13 ky four lateral sector collapses have affected the north-western flank generating the Sciara del Fuoco (Tibaldi, 2001). These last four lateral collapses (Figure 4) have been reconstructed by (Tibaldi, 2001), with volumes spanning from 0.73 to 2.23 km^3.

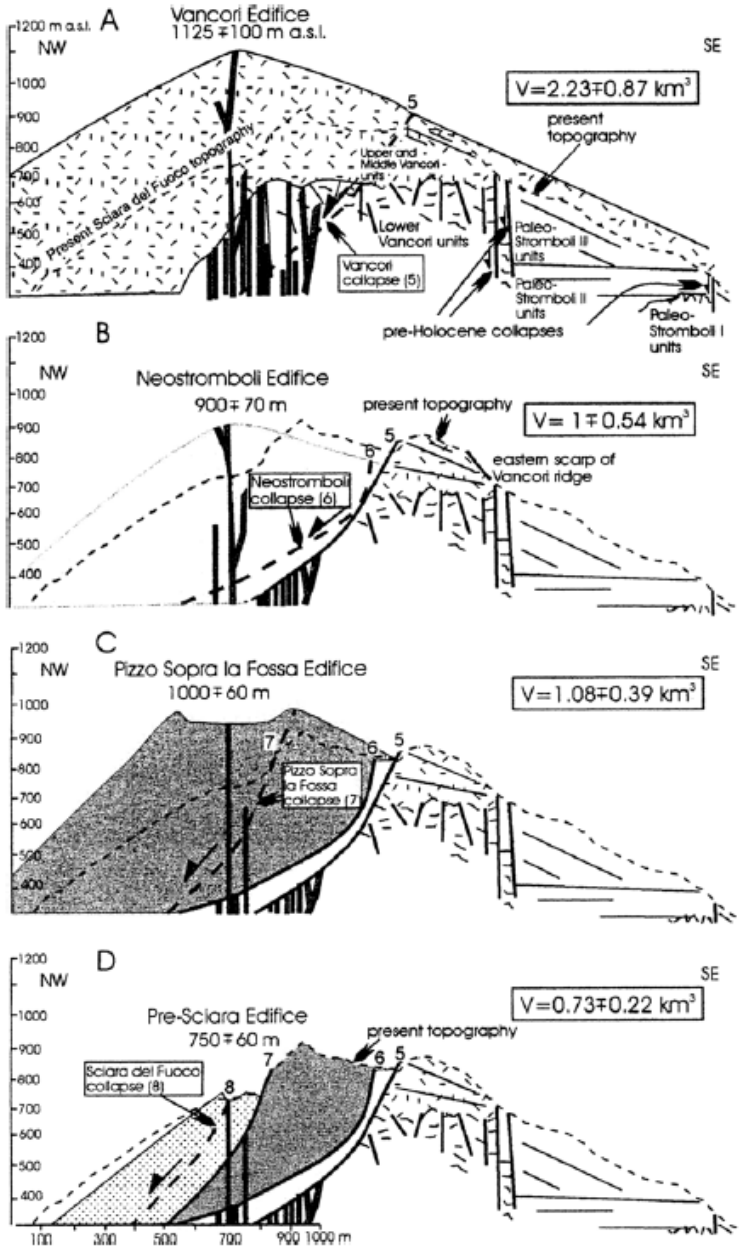

Figure 4. Geological cross sections (NW-SE) of the main successive lateral collapses occurred at Stromboli, from (Tibaldi, 2001). It is possible to note that the oldest lateral collapse (5) interested the highest edifice. The following collapses (6, 7, and 8), in fact, have shallower sliding surfaces and affected smaller pre-collapse edifices involving decreasing volumes.

These authors deduced that the oldest sector collapse affected the highest (1125±100 m high) and larger edifice (Vancori). Successive sector collapses took place when the new cone created inside the earlier collapse and the edifice reached a similar height and volume (Tibaldi, 2001). Therefore, the growing volcano mass can be considered as a major factor of lateral collapses (Tibaldi, 2001). The three oldest sliding surfaces (Upper Vancori, Neostromboli and Pizzo Sopra la Fossa) did cut the main magma conduit, whereas the upper scarp of the last collapse (Sciara del Fuoco) coincided with the conduit location.

During the last 2 ky, the eruptive activity at Stromboli volcano was characterised by a persistent explosive activity that was concentrated within the crater area and partially filled the Sciara del Fuoco, that was covered by volcaniclastic layers (composed by lava, spatter layers, scoria and ash layers) as well as chaotic accumulation of bombs and blocks (Kokelaar & Romagnoli, 1995; Rosi, et al., 2000; Tommasi, et al., 2005). A dynamic process of erosion and sedimentary transport, controlled by the slope angle (33° - 38°), continuously remodelled the morphology and funnels material from the subaerial to the submarine level (Kokelaar & Romagnoli, 1995). This process appears to be more effective along the steepest portion of the slope and along the shoreline, as a consequence of the sea's action (Marsella, et al., 2012). The Sciara del Fuoco extends to 700 m below sea level maintaining a continuity between the submarine and subaerial morphology. Then the slope decreases proceeding offshore and evolves in a channel (Figure 5) that reach 2000 m below sea level (Kokelaar & Romagnoli, 1995; Tommasi, et al., 2005).

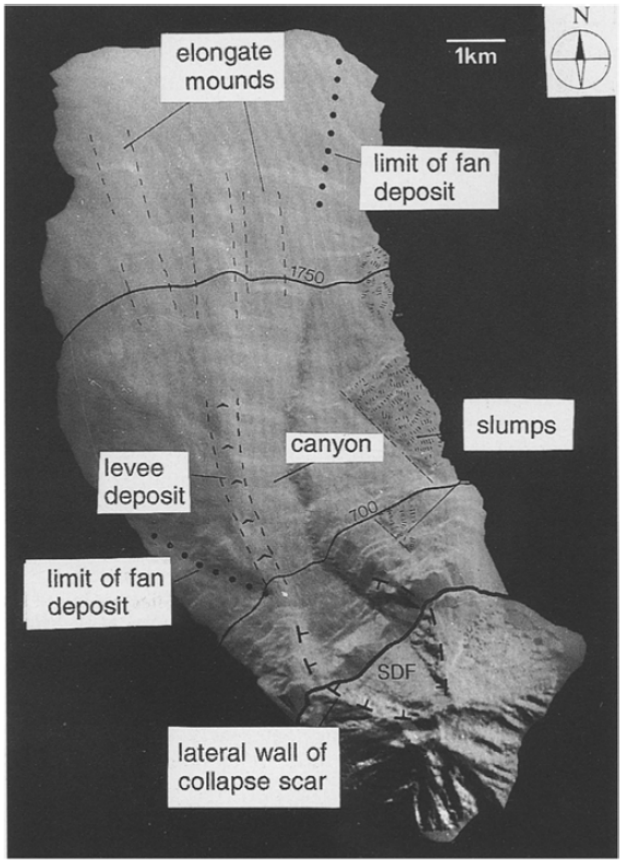

Figure 5. Shaded-relief model of the north-west flank of Stromboli, from (Kokelaar & Romagnoli, 1995). The main morphological and depositional features interpreted from bathymetric and seismo-acoustic data are reported. SDF indicate the Sciara del Fuoco slope.

The effusive activity highly contributes to the construction of the slope because the position of the main effusive vents, inside and outside the crater area, and their relative lava fields and flows emplacement, is enclosed in the Sciara del Fuoco. (Marsella, et al., 2012), have conducted a quantitative reconstruction of the morphological slope changes related to emplacement of lava flows and their successive erosion. By jointing historical maps, orthophotos and digital elevation models has been reconstructed the map of the lava flows emplaced onto the Sciara del Fuoco (Figure 6) from 1941 to 2007 (Marsella, et al., 2012).

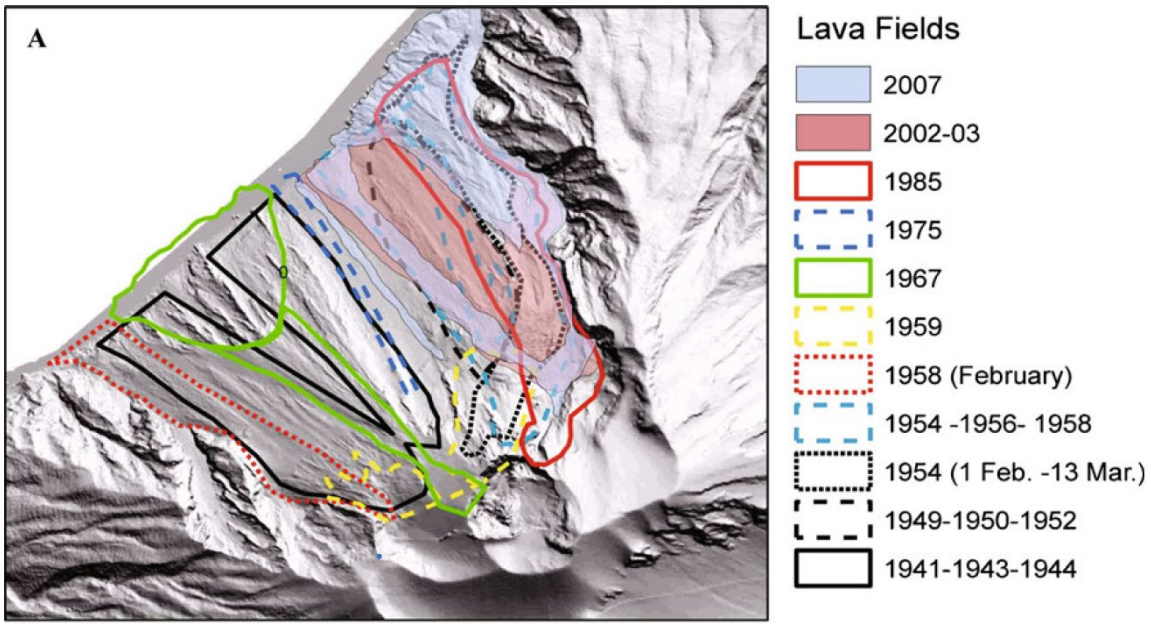

Figure 6. Lava fields along the Sciara del Fuoco, attributed to the different eruptions in the period 1941–2007, from (Marsella, et al., 2012). This reconstruction was performed using a multi-temporal topographic dataset, extracted from historical maps, aerial photogrammetric and Airborne Laser Scanner surveys.

Notably, in the last century the location of the eruptive vent feeding the flank effusive activity has suffered a shifting from the southwest to northwest sector of Sciara del Fuoco (Marsella, et al., 2012). Most of the eruptions that affected the southwest side are characterized by lava flows of modest thickness and lava fields spread along and usually do not reach the sea. This may be related to low effusion rates associated with these effusive episodes (Marsella, et al., 2012). Alternatively, the northwest sector was characterized by massive lava fields that often reach the coastline and propagate below sea level. Generally, the most relevant lava flows are effused from vents located at the base of the crater terrace at elevations usually higher than 600 m. This behaviour can be seen as the expression of a dike intrusion mechanism, which breaches the craters area and guides the lava flows along the lateral slopes of the escarpment. Actually, the northwest side of the slope represents a preferential path for the last lava effusions (Marsella, et al., 2012).

2.2. EXPLOSIVE REGIMES

Stromboli is an open conduit volcano and is well known for its persistent "strombolian" activity that has been lasting for millennia (Rosi, et al., 2000). This is characterized by a sustained explosive activity of mild intensity (Figure 7a), with emission of ash and scoriae up to a height of ~100-200 m above the crater terrace repeating regularly in time at a rate ranging between 4 and 12 explosions/hour (Ripepe, et al., 2009) with a typical value of ~7.8 events/hour (Delle Donne, et al., 2006; Patrick, et al., 2007). During normal activity the average magma supply rate from depth is 0.1-0.5 m^3/s (Ripepe, et al., 2005; Marsella, et al., 2012). This steady-state activity may show cyclic variations that are strictly related to the magma level within the open conduit. A low level is typical of periods with few and weak explosions, whereas a high magma level causes frequent and energetic strombolian explosions (Rosi, et al., 2013).

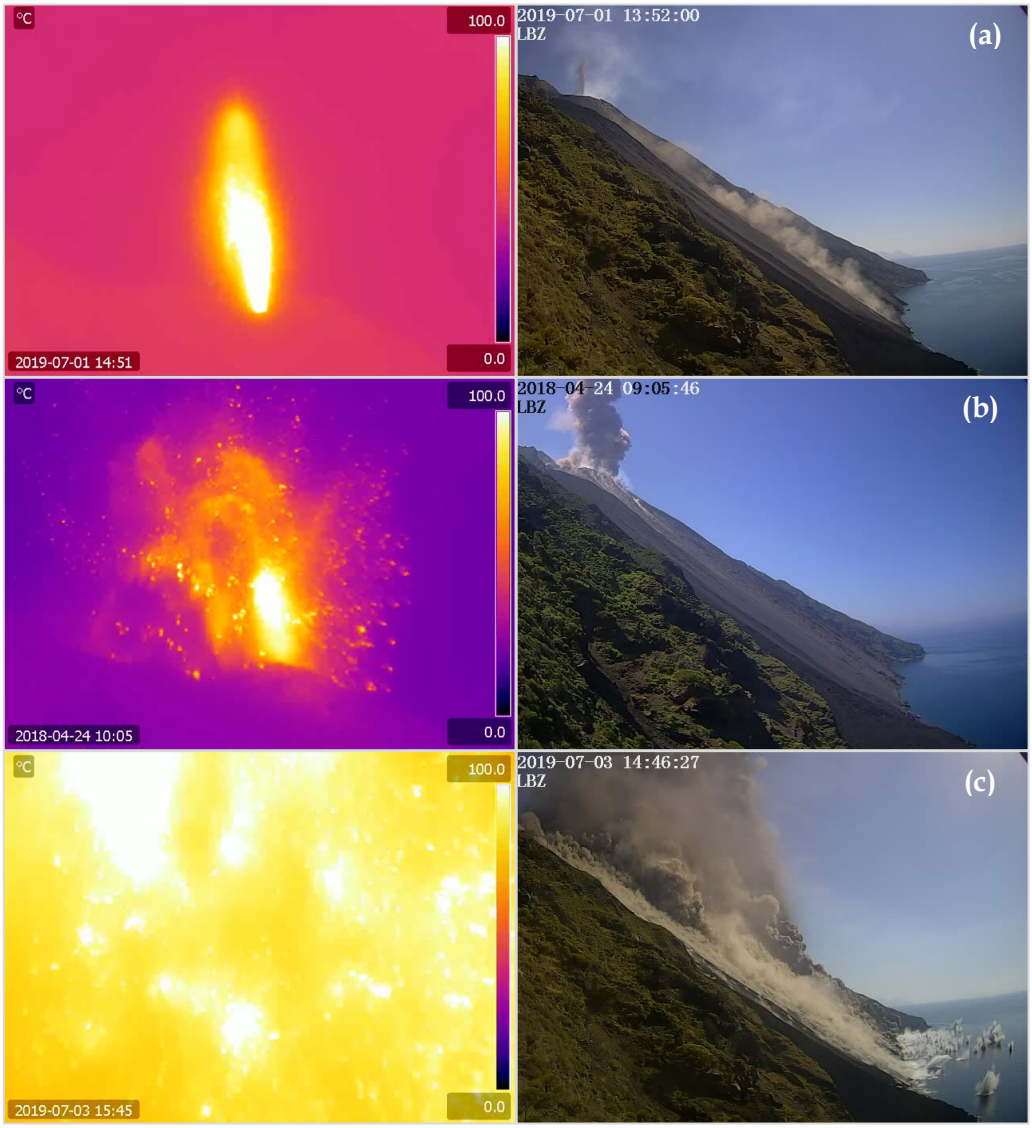

Figure 7. Snapshots from the thermal camera installed at station ROC at a distance of ~450 m from the NE crater and from the visible camera installed at station LBZ at ~1500 m from the crater terrace. Images show a Typical explosive event (a) a Major explosion (b) and the Paroxysm of July, 3, 2020 (c).

Ordinary explosive activity at Stromboli volcano has been extensively studied with multiple geophysical observations, spanning from ground deformation and seismicity (Genco & Ripepe, 2010; Chouet, et al., 2003), infrasound acoustics (Vergniolle, et al., 1996; Ripepe, et al., 2001), infrared thermometry (Patrick, et al., 2007; Delle Donne & Ripepe, 2012) and videogrammetry (Genco, et al., 2014).

This ordinary activity at Stromboli is seldom punctuated by major explosions and paroxysms (Barberi, et al., 1993; Rosi, et al., 2000) (Figure 7b, c).

Major explosions are discrete explosive events, significantly more powerful than the ordinary explosions, able to generate convecting columns up to 1-2 km and affecting with decimetre-sized blocks and scoriae the summit areas of the volcano. Typical occurrence of major explosions is ~2 events/year (Barberi, et al., 1993). Major explosions, also referred to as small-scale paroxysms (Métrich, et al., 2009) or intermediate explosions (Andronico, et al., 2008) have been reported frequently also during the on-going activity of Stromboli volcano.

Paroxysms represent the largest-scale explosive events at Stromboli volcano being able to generate convecting plumes up to a high of 10 km and eject meter-sized blocks up to distances of 2 km from the vents thus possibly affecting the settled areas of Stromboli island. 25 events were recorded between 1558 and 1993 (Barberi, et al., 1993) and ahead of few geophysical distal records (Imbo, 1935) paroxysms were mostly described from analysis of the deposits and effects on the volcanic edifice (Perret, 1916). Before the eruptive crisis in the summer of 2019 the most recent events occurred on March, 15, 2007 and April, 5, 2003, during effusive activity within the Sciara del Fuoco driven by an effusive vent positioned at the base of the summit craters (Rosi, et al., 2006), recorded with multiple geophysical observations (Rosi, et al., 2006; Pistolesi, et al., 2011). The events drove eruptive plumes of 3 and 5 km respectively. On July, 3, 2019 and on August, 28, 2019, two paroxysmal events occurred without a previous effusive activity. It is accepted that this kind of events are driven by a different source mechanism, which implies magma fragmentation able to produce the observed eruptive columns (Rosi, et al., 2006; Pistolesi, et al., 2011). Moreover, petrology of ejecta suggests a much deeper source of the events being driven by deep magma batches rising mostly in closed system conditions (Métrich, et al., 2009).

Products erupted during the different kinds of explosions at Stromboli share the same magma composition but differ significantly in terms of the volatile content and amount of crystals. A low porphyritic (LP), shoshonitic magma is erupted during paroxysms as light, crystal-poor, golden pumices, while a high porphyritic (HP) shoshonitic magma is erupted as dark scoriae during the ordinary Strombolian activity. Such a different crystal and volatile content, texture and glassy matrix composition, suggest different conditions of crystallization, storage and magma ascent and allowed to derive a conceptual model of the feeding system of Stromboli volcano (Métrich, et al., 2009), which consists into a magma ponding zone extending vertically from 7 to 10 km depth and a shallow reservoir from 2 to 4 km depth below the craters, with two reservoirs being connected by dykes (Figure 8).The LP magma resides in the deep reservoir, while the shallow reservoir is characterized by a degassed HP magma mush.

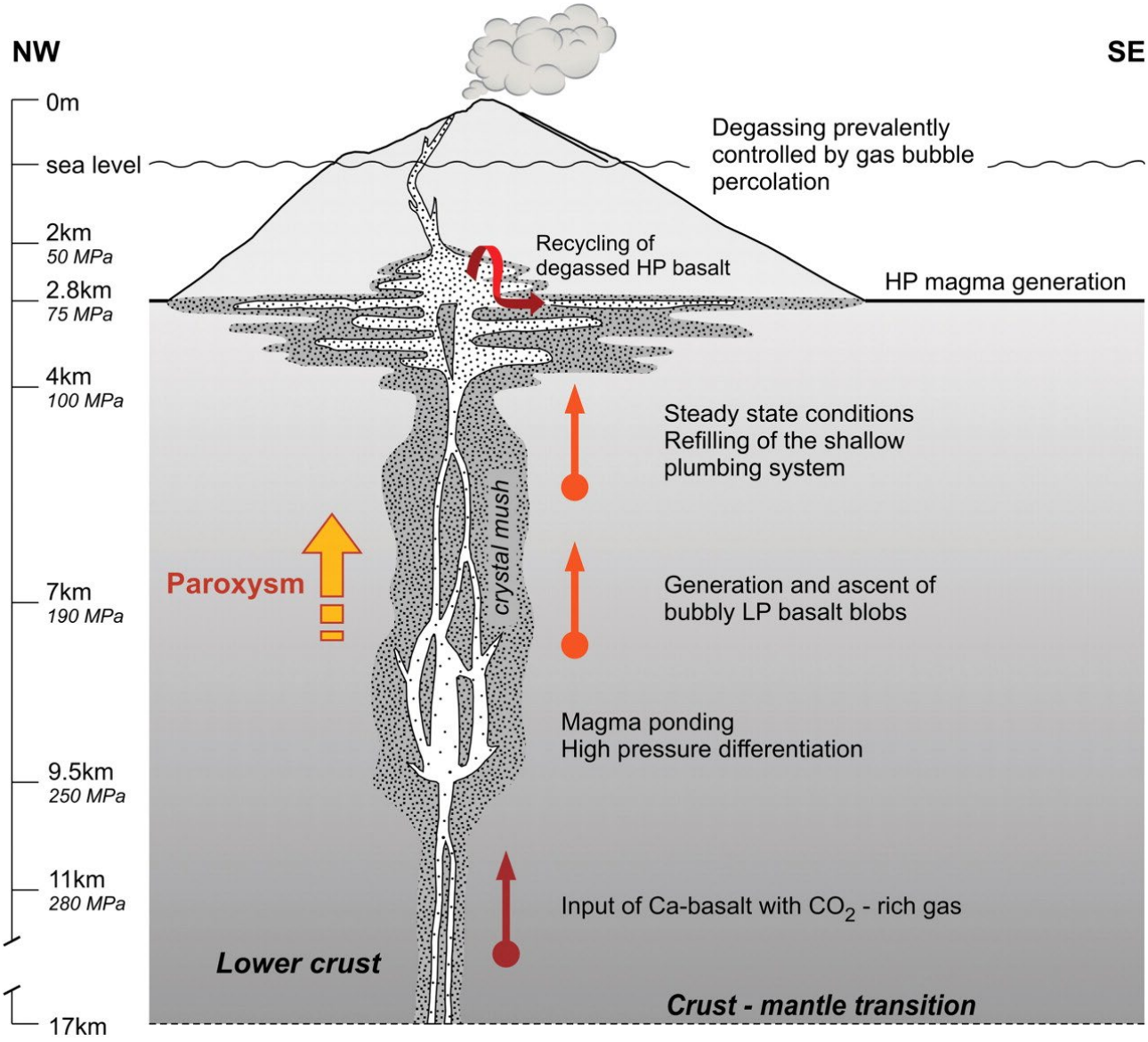

Figure 8. Interpretative model of the plumbing system of Stromboli based on the melt compositions, the crystal textures and the chemistry of Stromboli pumice and scoria samples. The geometry of the conduits within the uppermost 1 km – imaged as two complex dike systems underlying the summit craters with a sharp change in fracture dip at 80 and 280 m, respectively, below sea level (Chouet, et al., 2013) – is oversimplified. LP and HP basalts refer to low and high-porphyritic magmas, respectively, according to Francalanci, et al., 2004. From Métrich, et al., 2009.

Such a conceptual model is in general agreement with the different source mechanisms inferred for Strombolian explosions and paroxysmal events. Strombolian explosions are believed being triggered within the shallow magma reservoir by two-phase flow dynamics of gas slugs/bubbles rising within the shallow magma (Parfitt, 2004). On the contrary paroxysmal explosions are believed to be driven by batches of deep LP magma rising mostly in closed conditions from a depth of 7-10 km through the resident crystal-rich, gas-poor magma, mingling with the HP magma in the shallow feeding system and reaching eventually fragmentation (Métrich, et al., 2009), which appears to be consistent with observed explosivity (Rosi, et al., 2006; Pistolesi, et al., 2011).

Periods of high level of strombolian activity may be accompanied by summit overflows. Most of these events typically last few hours, remain confined into the crater terrace and rarely involve the

upper part of the Sciara del Fuoco (Rosi, et al., 2013). Notably, during overflow episodes the explosive activity at the vents is typically not interrupted.

Otherwise, the flank effusive eruptions cause the ceasing of summit explosions and may occur every 5-10 years (Rosi, et al., 2000). These events are related to the opening of eruptive fissures or lateral effusive vents with a lava drainage from 0.4 to 13.8 Mm^3 during timespan of weeks to months (Marsella, et al., 2012; Valade, et al., 2016; Ripepe, et al., 2017). In the last 2000 years, lateral effusive vents were always positioned within the Sciara del Fuoco slope, where lava flows were confined, reached the coast and formed lava deltas (Rosi, et al., 2013). Generally, flank eruptions occur after periods characterized by an input of gas and magma input into the shallow portion of the plumbing system exceeding the volume ordinarily managed by the summit craters. The 2002-2003, 2007 and 2014 flank eruptions at Stromboli volcano have been explained in terms of a gravity-driven drainage of a shallow, degassed magma reservoir, located between the crater terrace and the effusive vent (Ripepe, et al., 2015; Valade, et al., 2016; Ripepe, et al., 2017).

The large variability of observed volcanic activity, with major and paroxysmal events punctuating ordinary explosive activity, and effusive events that might destabilize the Sciara del Fuoco, clearly highlight the need of a reliable monitoring system, to track changes in source term parameters that might indicate an increased hazard. This is particularly critical for Stromboli island, considering that during the summer months the coastline is crowded and that tens of thousands of tourists visit the summit area every year.

Since the 2002-2003 flank effusion, the continuous and real-time monitoring at Stromboli has been largely developed with the installation of geophysical and geochemical instruments devoted to volcano surveillance. Among the various monitored parameters, particular attention should be given to volcano seismicity, as it reflects directly the source mechanisms acting at depth and might provide precursors of increased volcanic activity useful to predict the occurrence of paroxysmal activity.

2.3. DATA ACQUISITION SYSTEM

Geophysical data used in this work has been acquired by the permanent monitoring network deployed since January 2003 by the Laboratorio di Geofisica Sperimantale (L.G.S.) of the University of Firenze (Ripepe, et al., 2004). The network, that was mostly developed after the 2002-2003 effusive eruption of Stromboli volcano, consists of a network of 5 broadband seismo-acoustic stations, all equipped with 24 bits Guralp CMD-DM24 digitiser, a Guralp CMG-40T broadband seismometer (30 s eigenperiod and sensitivity of 800 V/m/s) and a broadband infrasound sensor, 1 small aperture 5-elements infrasound array, 3 Pinnacle 5000 borehole tiltmeters, 2 FLIR thermal cameras, 2 visible cameras, 2 SO2 UV cameras and 2 tide gauges (Figure 9).

Such an integrated monitoring network allows to monitor and study the Strombolian explosive dynamics considering both the ground seismicity that mostly reflect the coupling of the volcanic

source term with the ground, as well as geophysical parameters, such as infrasound acoustic and infrared thermometry, that are produced when explosive event reaches the surface (Figure 10).

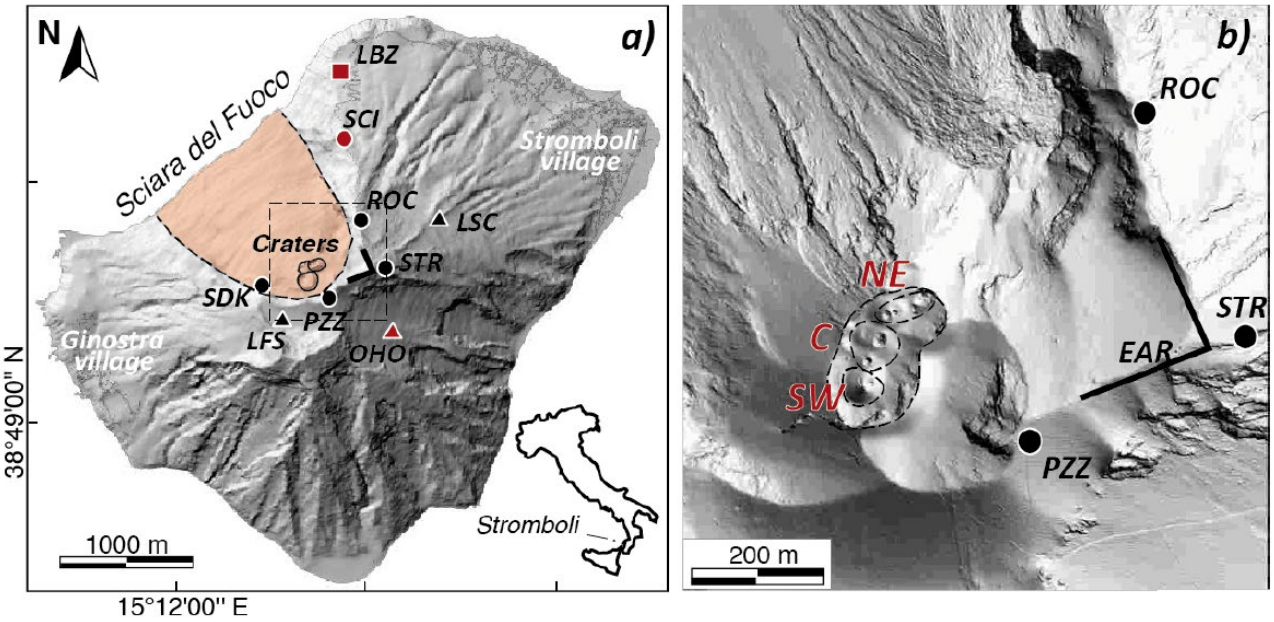

Figure 9. Shaded relief map of the Stromboli volcano. (a) Location of the geophysical sensors and extent of the Sciara del Fuoco slope (light brown). The broadband seismic station network used in this study consist of SCI, ROC, STR, PZZ, and SDK. Visible camera is LBZ. The borehole tiltmeters are LSC, OHO, LFS. (b) Location of the crater terrace and the main craters (SW southwest crater, C central crater, NE northeast crater) as they were until 3rd of July 2019. EAR indicates the infrasonic array location.

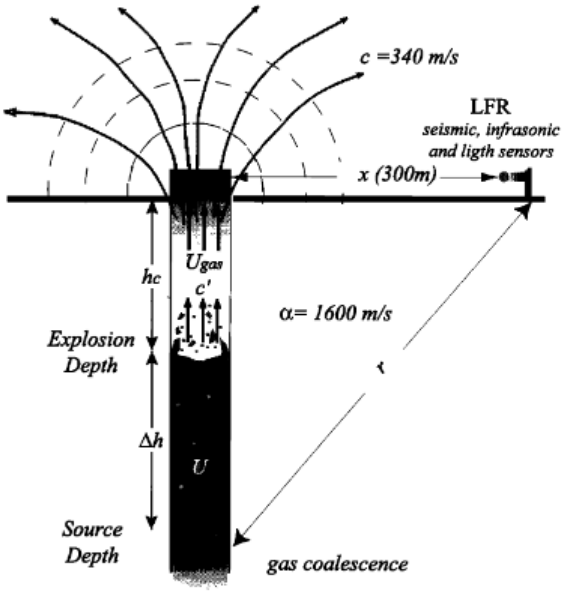

Figure 10. Schematic model of the magmatic conduit, where coalescence, rise and explosion of a gas slug can be investigated in terms of recorded seismic and infrasound signals that reflect respectively the formation in the conduit (seismic) and explosion at the surface (infrasound) of the gas bubble driving Strombolian explosion. From Ripepe, et al., 2001.

I focus in this thesis on seismic data to investigate variation of the seismic source in relation to explosive regimes. In particular, I investigated seismic tremor, that is a sustained signal related to degassing activity, and transient seismicity related to explosive events through seismic interferometry in relation to transition regime from ordinary activity to paroxysms. Therefore, among the different monitoring stations, I focused on seismic data collected by SCI, ROC, STR, PZZ and SDK stations (Figure 9).

List of geographical positions of stations as well as the distance among them is provided in the table below (

Table 1).

	Latitude	Longitude	Elevation (m a.s.l.)
SCI	38° 48' 03.84" N	15° 12' 57.69" E	510
ROC	38° 47' 51.11" N	15° 12' 58.29" E	713
STR	38° 47' 37.79" N	15° 13' 03.76" E	825
PZZ	38° 47' 32.02" N	15° 12' 57.95" E	770
SDK	38° 47' 35.62" N	15° 12' 27.32" E	650

Interstation distances (m)				
SCI	ROC	STR	PZZ	SDK
-	390	808	1000	1137
390	-	435	620	870
808	435	-	264	910
1000	620	264	-	768
1137	870	910	768	-

Table 1. Geographycal positions of stations and interdistances between stations.

All stations are located around crater terrace that would be desirable in order to evaluate changes inside enclosed area.

All stations are equipped with GPS antenna, provided with the digitiser, for absolute time syncronization. This is extremely important if the reasearch target is to evaluate velocity changes , i.e. arrival time changes, especially if the size of seismic network is small.

All acquired data are recorded locally and transmitted to the Centro Operativo Avanzato (COA) of the Department of National Civil Protection in the village of Stromboli. Data are then stored, archived and made available for real-time monitoring purposes.

2.4. SEISMIC SIGNALS RECORDED AT STROMBOLI VOLCANO

Seismic signals recorded at Stromboli volcano are dominated by discrete transients of small amplitude (< 10-5 m/s) and short duration (< 10 sec) produced by the ordinary strombolian explosions. This activity typically repeats every 2-5 minutes, over-imposing on background sustained volcanic tremor. The ordinary seismic activity is seldom punctuated by larger amplitude transients related to major explosions (1-2 times a year) and paroxysms, with 4 events recorded since April 2003 (refer to section 2.2 for a discussion on major explosions and paroxysms). Additionally, discrete seismic transients such as rockfalls, volcano tectonic events and regional tectonic earthquakes are recorded. These discrete transients over-impose on a persistent volcanic tremor.

2.4.1. SEISMIC SIGNALS OF EXPLOSIVE ACTIVITY

Persistent explosive activity at Stromboli volcano is associated with very long period (>3 s) seismic events (VLP) (Neuberg, et al., 1994), that are similarly reported on other basaltic explosive volcanoes worldwide (Nishimura, et al., 2000; Aster, et al., 2003). At Stromboli they are inferred to reflect a rapid expansion of a gas slug in the magma conduit, just before the explosion (Ripepe, et al., 2001; Chouet, et al., 2003). Semblance-based method has allowed location of the seismic source at 220 – 260 m beneath and 160 m northwest of the active vents (Chouet, et al., 2003). This shallow source repeats in time generating VLP seismic signals that cluster mainly into two classes each with surprisingly stable waveforms (Neuberg, et al., 1994; Chouet, et al., 1999; Chouet, et al., 2003). Seismic moment tensor inversion (Chouet, et al., 2003) and laboratory experiments (Ripepe, et al., 2001; James, et al., 2004) suggest indeed that VLP events can be explained by a volumetric expansion of a gas slug in the magmatic conduit followed by a downward force induced by the rapid gas expansion of the bubble as it approaches the magma-free-surface.

Analysis performed at Stromboli volcano reveal that VLP seismic events tend to cluster into two main classes of events, with stable waveforms, corresponding to explosive activity at the two (NE and SW) main active craters (Figure 11). Despite waveforms are changing slightly in the high frequency components, VLP signature of a single cluster is very stable in time (Figure 12), suggesting the existence of a repetitive, non-destructive source mechanism repeating in a stable position. Its detection and location are therefore reflecting the explosive source mechanism, and its changes through time might reflect changes of the explosive regime. The existence of VLP signals, even during effusive eruption when summit explosive activity was missing (Marchetti & Ripepe, 2005), was used to confirm that the explosive source process, related to gas coalescence, was still active but confined deep in the conduit (Marchetti & Ripepe, 2005).

The polarization ellipsoid of the VP component of the seismic signal has been used extensively to locate the seismic source at Stromboli (Chouet, et al., 2003). Despite the absolute location is still debated, as polarization ellipsoid, in terms of dip and azimuth, is not pointing directly to the active crater (Figure 13), its relative variation is reflecting a migration of the seismic source.

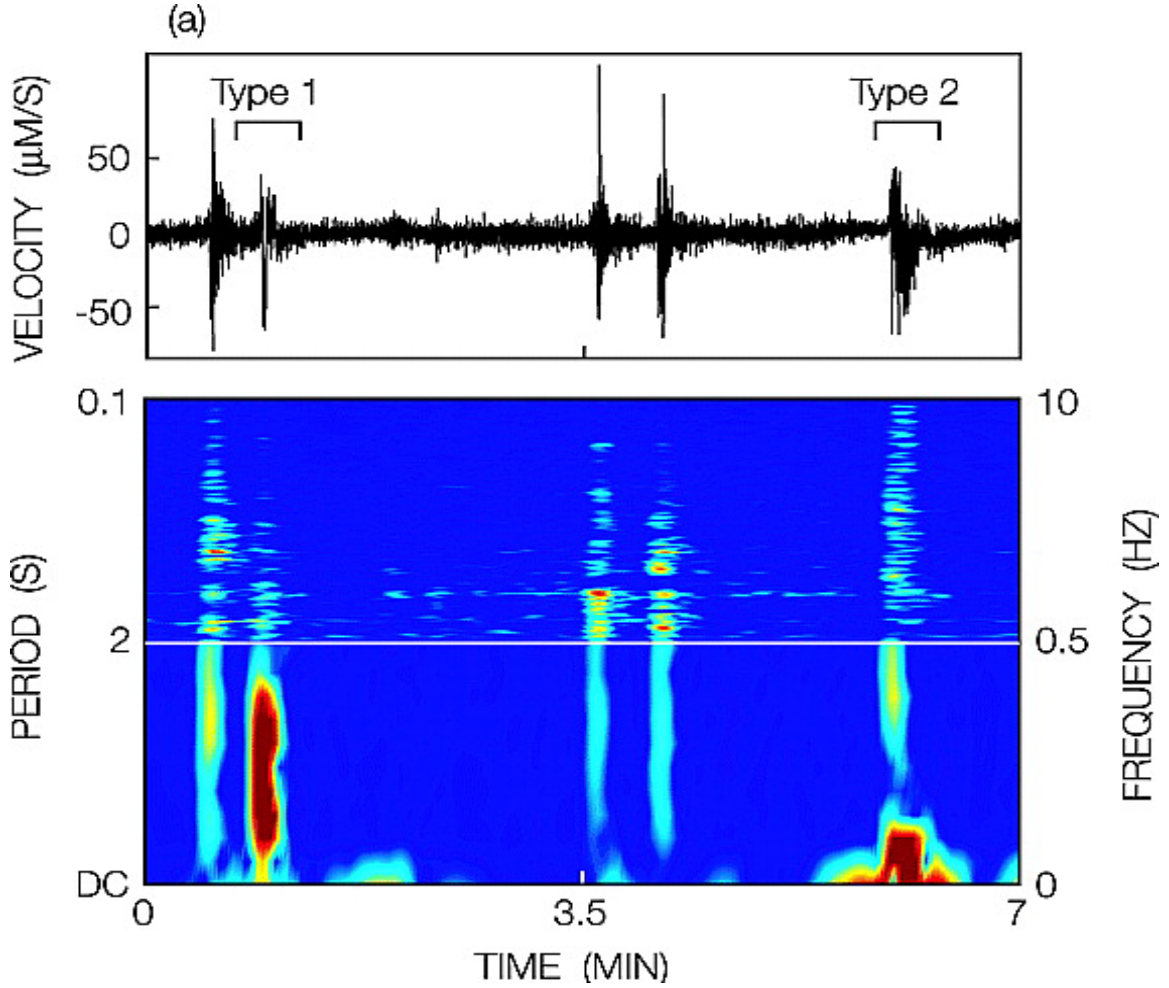

Figure 11: 7 minutes long sample of vertical seismic ground velocity recorded at Stromboli volcano and corresponding spectrogram showing the VLP spectral component of explosion quakes associated to the two main active craters. From Chouet, et al., 2003.

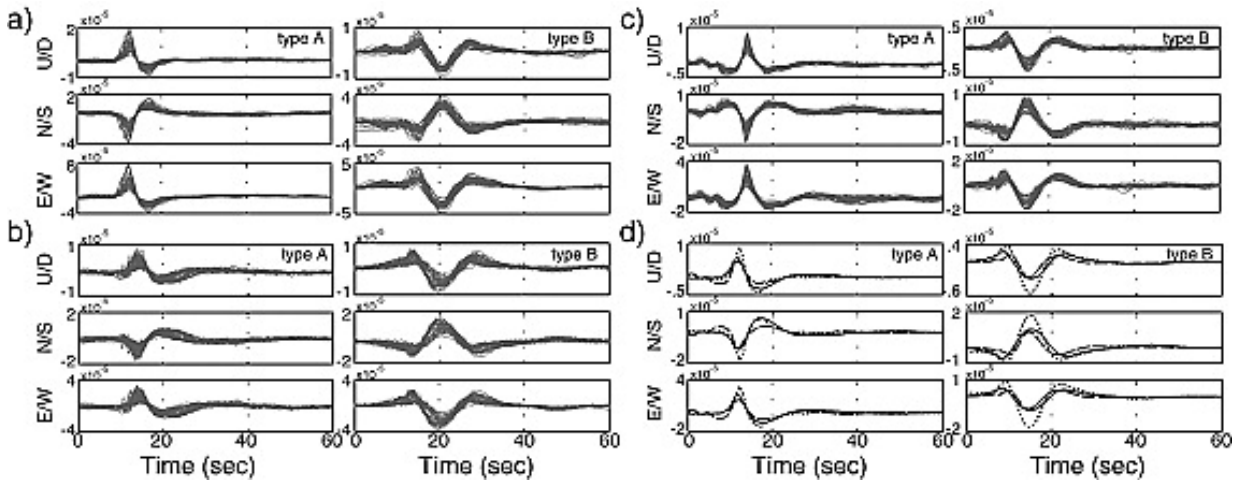

Figure 12: Stability of VLP seismic displacement for the two main clusters of events. From Marchetti & Ripepe, 2005.

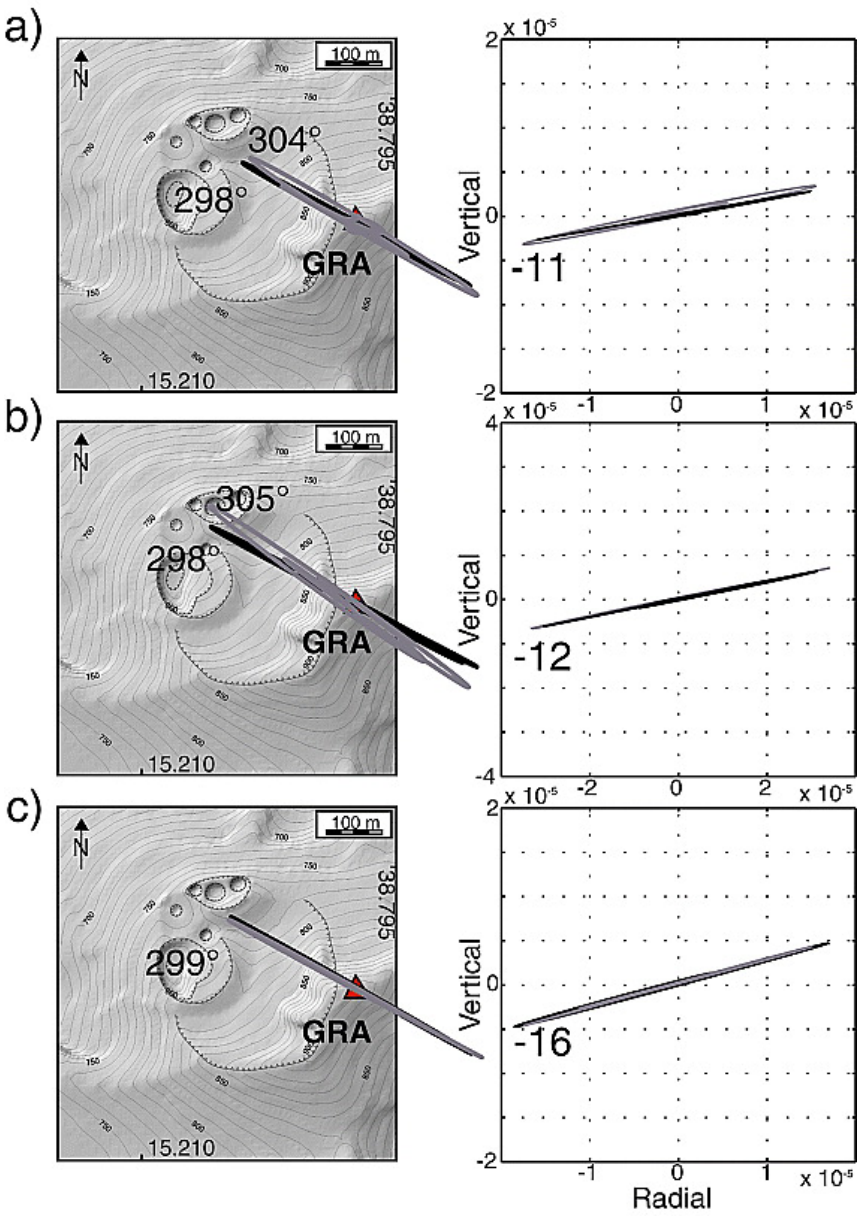

Figure 13: Polarization ellipsoid of VLP seismic ground displacement of the 2 clusters of events. The polarization ellipsoid, despite differing between the two events, is not pointing to the active craters. From Marchetti & Ripepe, 2005.

By considering 300,000 discrete seismic events recorded at Stromboli volcano, Ripepe et al., 2015 clearly showed how the dip of the ground displacement particle motion vector changed during the 2007 effusive eruption and how it matched on the long term, the variation of the elevation of the magma rim, suggesting how the VLP location is controlled by the magma level within the conduits. The authors eventually showed, how the dip of the particle motion vector was nicely fitting with the modelled magma discharge, indicating a gravity-driven magma discharge dynamic (Ripepe, et al., 2015).

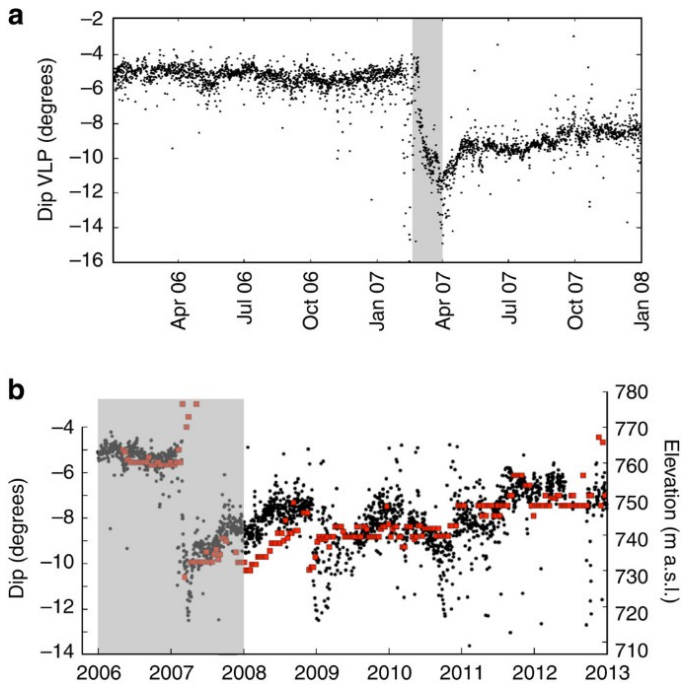

Figure 14: Dip of the particle motion vector of the VLP seismic displacement at Stromboli volcano during the 2007 effusive eruption (a). Comparison of the dip of the ground displacement (black dots) and elevation of the crater rim (red squares) as measured by a thermal camera (ROC in Figure 9) during a 7-year long time period between 2006 and 2013 (b). From Ripepe et al., 2015.

Results achieved at Stromboli, clearly indicate that a migration of the magma level within the conduit, can be tracked by the location of the VLP seismicity. This is done routinely by the analysis of the particle motion vector of the ground displacement, that is however strongly dependent on the position of the seismic station, with nice results observed only for station deployed at high elevation (Figure 15) or with semblance analysis performed with a network of stations (Chouet, et al., 2003).

In this thesis, I apply seismic interferometry to seismic data recorded at Stromboli and investigate results in relation to the VLP seismic signals, in order to evaluate the potential of seismic interferometry to investigate VLP seismicity compared to standard techniques.

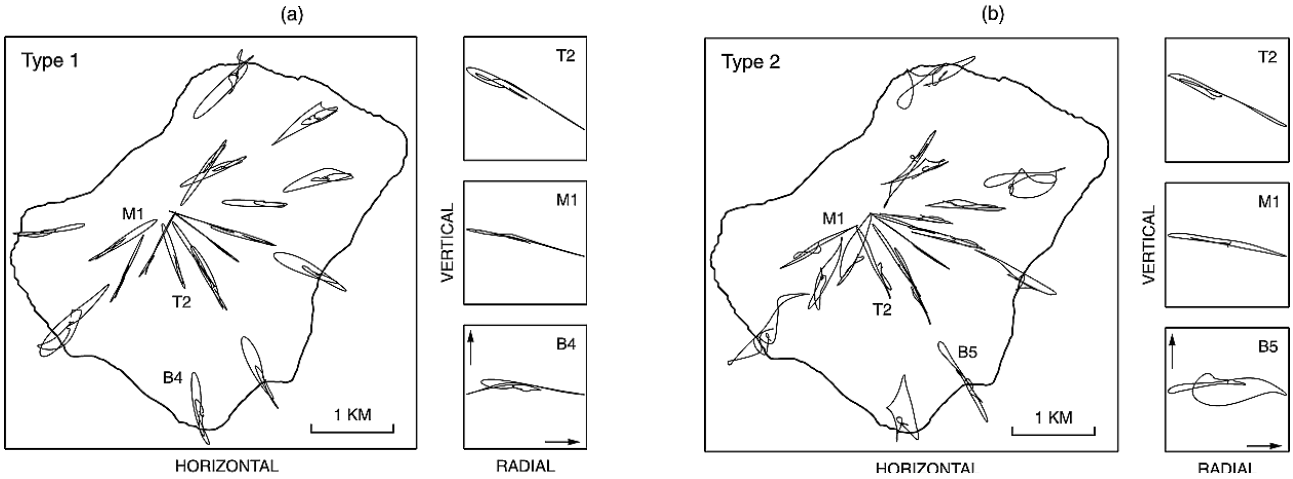

Figure 15: Polarization ellipsoid of the two clusters of seismic events as a function of station position on Stromboli volcano. The polarization ellipsoid is more scattered for stations deployed at lower altitude. From Chouet et al., 2003.

2.4.2. VOLCANIC TREMOR

Volcanic tremor is one of the most studied parameters to describe volcanic activity worldwide (Konstantinou & Schlindwein, 2003). Volcanic-tectonic earthquakes, earthquakes due to explosions, or other phenomena studied with seismic method have no similarities with volcanic tremor. Only geyser folds and geothermal activity seems to have a certain similarity (Nicholls & Rinehart, 1967; Douze & Sorrells, 1972).

Volcanic tremor was recorded for the first time during the Usu volcanic eruption (Omori, 1911) in 1910. Since then, tremor has soon acquired more and more popularity and many authors started to record repeatedly during the volcanic eruptions all over the word: Kilauea (Eaton & Richter, 1960); (Finch, 1949), Mauna Loa (Finch, 1943; Jaggar, 1920), Krakatau and Paricutin (Finch, 1949), Vesuvius (Imbo, 1935), Meakan-dake (Sakuma, 1957), Kluchevskoi (Gorshkov & Dubik, 1970), Niragongo (Berg & Janessen, 1960), Ruapehu (Dibble, 1969), and many others.

Today it is known, with reasonable certainty, that volcanic tremor is characterized by some regularities such as: (1) stability in time (from 2-3 days to several months) (Omori, 1911; Jaggar, 1920; Finch, 1943; Finch, 1949), (2) stability of the period and the amplitude of tremor (Imbo, 1935; Finch, 1949; Sakuma, 1957), and (3) distinct resolution of registered tremor into a series of nonextinct harmonic oscillations (Finch, 1949; Sakuma, 1957).

Nowadays, however, despite having been observed so widely and investigated so deeply, the possible source mechanisms of the volcanic tremor are still uncertain and not physically grounded and only few hypotheses have been made. In most of the above-mentioned papers the authors have supposed that the generating mechanism of volcanic tremor (by analogy with other seismic phenomena) is the displacements of masses in the deep or near-surface parts of the volcano. Often referred to "rhythmic shock activity of rising lava" (Finch, 1949) or "internal eruptions of gases" (Sassa, 1935), "leakage of gases through the system of cracks" (Sakuma, 1957), and "movement of magma in the channel" as possible sources of volcanic tremor. Other authors suggest that such a time stationary phenomenon as volcanic tremor may be caused only by a stationary process that is the process of discharge of gases (Steinberg & Steinberg, 1975). Proposed source mechanisms, all including an effect of gases, are the i) Fluid-flow-induced oscillations (Scott & Stevenson, 1984); ii) Excitation of fluid filled cracks (Aki, et al., 1977); iii) hydrothermal boiling (Leet, 1988) or the iv) resonance of large magma bodies (Sassa, 1935).

Volcanic tremor described so far can be referred as "harmonic tremor", characterised by a constant period and continuous low frequencies (typically ranging from 1 to 5 Hz), sometimes single frequency, caused by complex interactions between magma, exsolved gases, and bedrock at volcanoes (McNutt, 2000). Spasmodic bursts of tremor, also referred to as spasmodic tremor, has a higher frequency and shows typically a pulsating and irregular envelope. This kind of tremor may precede and almost always accompanies eruptions, and was the most consistent short-term indicator of impending eruptions in a study of 200 calderas worldwide (McNutt, 2000).

More recently, the combined used of infrasound and seismic sensors, showed how on open conduit volcanoes, volcanic tremor is strictly related to volcanic degassing (Ripepe, 1996; Ripepe & Gordeev, 1999), thus pointing to a degassing nature of the process. Combined seismo-acoustic record at

Stromboli (Figure 16) and Etna volcanoes (Ripepe & Gordeev, 1999; Ripepe, et al., 2001), revealed indeed the existence of pressure transients repeating regularly in time every few seconds, matching amplitude fluctuations of volcanic tremor (Figure 17) and related to intermittent gas release from the active vents.

Based on the spectral characteristics of volcanic tremor and infrasound, it was proposed that the source function for the shallow volcanic tremor at Stromboli could be the viscoelastic reaction of the magma to the pressure decrease induced by gas bubble growth rate under constant depressurization (Ripepe & Gordeev, 1999). The spectrum of our source function is controlled by the time duration of the pressure pulse, which represents the viscoelastic relaxation time of the magma and gas bubble growth rate. The predicted asymptotic decay of the frequency contents fits the spectral behaviour of the volcanic tremor recorded at Stromboli, as well as on different volcanoes.

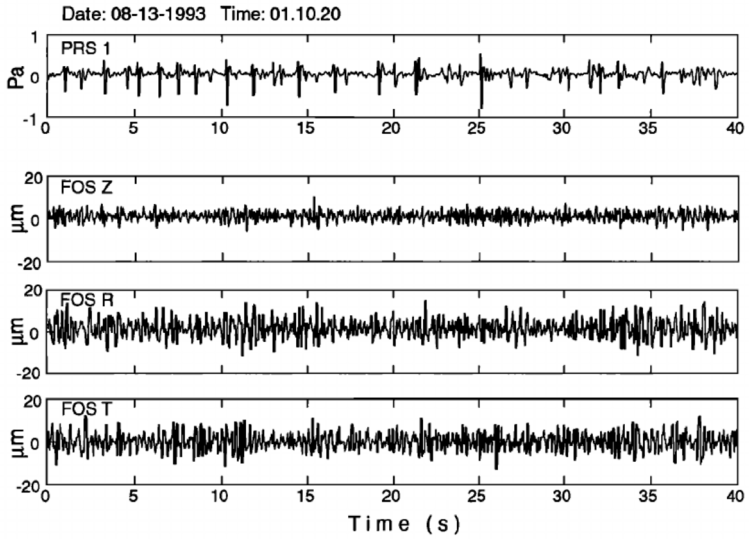

Figure 16. Infrasonic pressure (PRS) and ground displacement at (Z vertical, R radial, T tangential) recorded at Stromboli volcano. From Ripepe & Goordev, 1999.

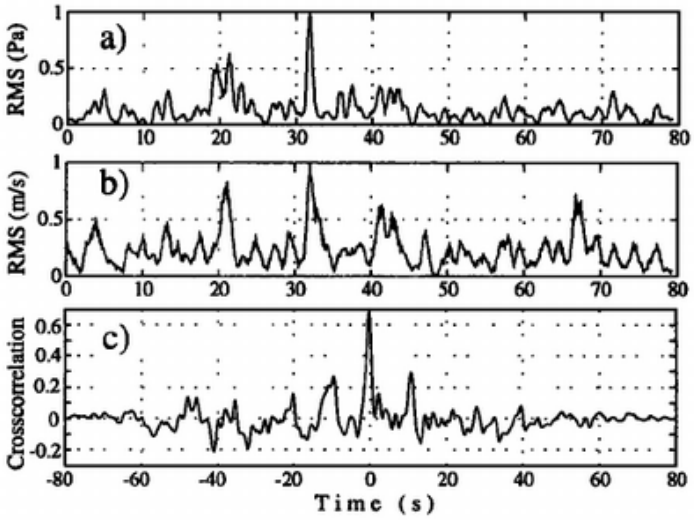

Figure 17. Root-mean-squared amplitude of infrasound (a) and seismic velocity (b) at Etna volcano. Cross-correlation (c) between the two rms time-series reveals suggests they are synchronous, thus indicating a degassing nature of volcanic tremor. From Ripepe et al., 2001.

Seismic array data analyses suggested that the origin of tremor at Stromboli is generally quite shallow and limited to <200 m below the craters (Chouet, et al., 1997) and it has been explained as the elastic response of the system to the continuous degassing (puffing) of the magma column (Chouet, et al., 1997; Ripepe & Gordeev, 1999).

Weather can also affect seismic signals. At Stromboli in particular, greater amplitude and lower frequency (~ 0.3 Hz) signal is superimposed to volcanic tremor during rough sea period, affecting mostly the stations deployed at lower elevation. Incoherent transients with higher frequency content, typically > 15 – 24 Hz, can be attributed to strong wind.
Tremor at Stromboli is generally characterized by a frequency content between 1–5 Hz with the largest energy concentrated at around 1.6 Hz (Chouet, et al., 1997; Falsaperla, et al., 1998), thus not really affected by these external source of noise. Because of the time persistency, occurring almost continuously, the peak frequency content (1-5 Hz), that is outside the main frequency band of noise related to rough sea and wind and its source mechanisms, being related to magmatic degassing, volcanic tremor at Stromboli is a perfect candidate to apply seismic interferometry to investigate changes of the signal characteristics possibly reflecting changes in the explosive regimes.

2.5. DYNAMIC MODEL

As described in section 2.2, since at least 3-7 AD (Rosi, et al., 2000), the activity of Stromboli volcano is characterized by persistent degassing punctuated by explosions of different amplitude scales, from weak explosions to major and paroxysmal events.

Strombolian activity requires a stable source mechanism that is persistent through time. This has been explained in terms of two models, the collapsing foam (CF) model (Jaupart & Vergniolle, 1989) and the rise speed dependent (RSD) model (Parfitt, 2004).

The Collapsing Foam model suggests that exsolved gas bubbles create a foam accumulating at a physical boundary. Different hypothesis on such a boundary have been made: a chamber roof (Jaupart & Vergniolle, 1989), a constriction at the dyke-to-conduit transition (Ripepe, et al., 2001), a change in magma viscosity (Thomas, et al., 1993), or a cool magma skin forming on the top of the magma column. The foam layer becomes unstable when it reaches a critical thickness and collapses to generate a gas slug. The rise and burst of this slug inside the conduit lead to a strombolian explosion (Blackburn, et al., 1976; Jaupart & Vergniolle, 1989).

The Rise Speed Dependent model involves large bubble that overtake and coalesce with small bubbles to eventually generate a gas slug (Wilson & Head III, 1981; Parfitt & Wilson, 1995) inside a slowly (0.1–1 cm s^{-1}) rising magma. Therefore, the activity level depends on factors such as the magma rise speed, gas content and magma viscosity (Parfitt & Wilson, 1995).

Such persistent and repetitive activity indicates an efficient conduit supply (Kazahaya, et al., 1994; Stevenson & Blake, 1998), calculated as occurring at a rate of 300–1300 kg s^{-1} (Francis, et al., 1993;

Allard, et al., 1994; Harris & Stevenson, 1997; Francalanci, et al., 1999). The occurrence of small (<1 Pa) infrasonic pulses associated with shallow volcanic tremor (Ripepe, 1996; Ripepe & Gordeev, 1999) suggest a gas-rich magma ascending, degassing and sinking within the conduit or a discrete batches of gas-rich magma or gas bubble layers rising at a rate of ~1 s^{-1}.

This gas-rich magma is likely a probable consequence of differential gas bubble velocity which produce instability waves in magma (Manga, 1996) or a natural variation in the coalescence of a foam trapped at the roof of a shallow reservoir (Jaupart & Vergniolle, 1989).

When the foam collapses, it radiates a seismic wavefield (Chouet, et al., 1999; Ripepe, et al., 2001) indicating that the explosive events are triggered by a pressure drop originating at a depth of ~100–200 m below the vents.

A stable and continuous convection generates degassing, foam layer formation, and explosive activity approximately constant. Otherwise, discrete pulses of fresh, gas-rich magma produce a variable degassing, foam layer formation, and explosive activity.

In any case, degassing at Stromboli cycles through periods of high and low magma supply rate and periods of high gas fluxes and puffing activity correlate with periods of increased explosion frequency. This correlation is also consistent with foam layer generation and collapse, where periods of high magma supply will increase the rate at which foam layers build. Moreover, magma increasing rise speed produce a decreasing in the time delays between strombolian events (Wilson & Head III, 1981; Parfitt & Wilson, 1995).

3. SEISMIC INTERFEROMETRY ANALYSIS

3.1. BASIC PRINCIPLES

Interferometry consists into the analysis of the interference between a pair of signals in order to obtain information about the signal source and/or the propagation media. In the specific case of seismic signals, interferometry allows to obtain an indirect description of the subsurface. The basic principle consists in evaluating the seismic responses of a propagation medium considering virtual sources by simply cross-correlating seismic observations at different receiver locations, where the cross-correlation function, is a numerical operator that expresses the degree of correlation between two time series as a function of the mutual time delay.

If we consider a seismic wavefield s(t), that is excited at the source location x_S at time $t = 0$ (Figure 18a), it will propagate and strike the receiver at location x_A at time $t = t_A = \frac{x_A - x_S}{c}$, where c is the propagation velocity and it will be recorded as a seismic displacement (u) defined as:

$$u(x_A, x_S, t) = G(x_A, x_S, t) * s(t) \qquad \text{Eq. 3.1}$$

where $G(x_A, x_S, t)$ is the Green's function of the propagation medium between the source (x_S) and the receiver (x_A) and the symbol $*$ denotes the convolution (Figure 18b). The Green's function of a propagation medium is a function that describes how a medium deforms a seismic wave, in terms of attenuation and scattering, while it propagates through it.

Similarly, the corresponding wavefield will be recorded at location x_B at time $t = t_B = \frac{x_B - x_S}{c}$ (Figure 18c), is given by

$$u(x_B, x_S, t) = G(x_B, x_S, t) * s(t) \qquad \text{Eq. 3.2}$$

The difference of the signal recorded at station A ($u(x_A, x_S, t)$) and at station B ($u(x_B, x_S, t)$) will be strongly affected by the complexity of the medium, and dependent of the frequency content of the original seismic wave (s(t)).

In the same way, equation Eq. 3.2 might be rewritten as

$$u(x_B, x_S, t) = G(x_B, x_A, t) * u(x_A, x_S, t) \qquad \text{Eq. 3.3}$$

and the signal recorded in B can be considered as being produced by a source in A, that propagated for a time $\delta t = t_B - t_A$ (Figure 18d).

If we consider that equation Eq. 3.1 is independent of the propagation direction:

$$u(x_A, x_S, -t) = G(x_A, x_S, -t) * s(-t) \qquad \text{Eq. 3.4}$$

we can combine equations from Eq. 3.1 and Eq. 3.4 to obtain:

$$u(x_B, x_S, t) * u(x_A, x_S, -t) = G(x_B, x_S, t) * s(t) * G(x_A, x_S, -t) * s(-t) \qquad \text{Eq. 3.5}$$

that, considering the time reversal, allows to turn the time convolution into a cross correlation and obtain the relation between the Green's function of the medium $G(x_A, x_B, t)$ and the cross correlation of the recorded signals as:

$$u(x_B, x_S, t) \bigotimes u(x_A, x_S, -t) = G(x_B, x_B, t) * S(t) \qquad \text{Eq. 3.6}$$

where S(t) is the auto-correlation function of the source term.

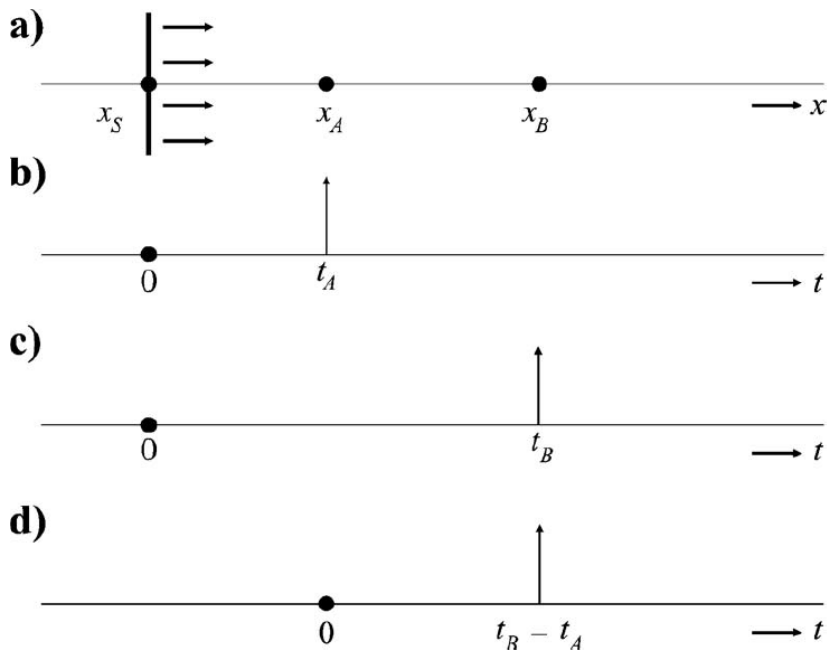

Figure 18. A 1D example of direct-wave interferometry. a) An impulsive source $x = x_s$ and $t = 0$ produce a plane wave traveling along the x-axis. b) The Green's function $G(x_A, x_S, t)$ i.e., the response observed by a receiver at x_A.. c)_As in b) but for a receiver at x_B. d) Cross-correlation of the responses at x_A and x_B. This is interpreted as the response of a source at x_A, observed at x_B, i.e., $G(x_B, x_A, t)$. From Wapenaar, et al., 2010.

A seismic signal recorded at a location A can be cross-correlated with the seismic signal recorded at the same time at the location B, and the result can be considered as being representative of the propagation medium between A and B for a point source located in A or B. Green's function convolved with a wavelet is the point-source response Eq. 3.6, which is why the seismic interferometry is often called Green's function retrieval.

Seismic interferometry is performed by several algorithms: cross-correlation (Claerbout, 1968; Bakulin & Calvert, 2004), deconvolution (Trampert, et al., 1993; Snieder & Safak, 2006), cross-coherence (Aki, 1957; Prieto, et al., 2009), and multidimensional deconvolution (Wapenaar, et al., 2008; Minato, et al., 2011).

3.2. STATE OF THE ART

After the pioneer theoretical studies performed in the 1950s (Aki, 1957), seismic interferometry experienced a dramatic increase in the last 15 years, and is now widely applied both to active sources and passive ambient noise to study subsurface structures spanning from a few hundred meters to tens of kilometres as well as source characteristics through time.

Seismic interferometry can be applied both in active and passive mode. The first application is used when signals used for interferometry are produced specifically by controlled active sources, such as man-made explosions, where the exact timing, location and spectral content is perfectly known. Such an approach often involves the stacking of correlations associated with the active source at different positions to obtain a mean representation of the propagation medium. The passive mode is applied to seismic signals generated by earthquakes or endogenous seismic noise and, in this latter case, it involves the implicit summation of signal resulting from the superposition of multiple sources, uncorrelated among each other and acting simultaneously.

Seismic interferometry has also been often classified depending on the type of seismic waves used for the analysis, and has been addressed in terms of direct-wave, reflected-wave or coda-waves interferometry. Seismic interferometry has been applied for long time mostly on coda waves of earthquakes, to characterize small changes over time. Despite the increased analysis complexity, compared to direct waves, coda waves contain conclusive information about regional scattering and attenuation properties (Aki, 1969; Aki & Chouet, 1975).

The seismic coda is the tail of scattered waves (Snieder, 2006). In 1985, Aki measured the scattering in the Earth evaluating the temporal decay of the seismic coda. He defined the code quality factor (Q) and related its changes to changes in the stress in the subsurface (Aki & Chouet, 1975; Jin & Aki, 1986). The method considers the amplitude of the coda waves only, neglecting the phase information. In a strongly-scattering medium, however, this method is highly sensitive to changes in the medium.

More recently, coda wave interferometry was based not only on the quality factor (Q) but also on phase information of coda waves (refer to Snieder, 2002 for a review). Coda waves are widely investigated in ultrasound experiments (Snieder, 2002; Grêt, et al., 2006) and to evaluate velocity changes in fault zones (Poupinet, et al., 1984), where the high sensitivity of their analyses is appreciated. Temporal changes in the coda waves have been observed in volcanic environment (Ratdomopurbo & Poupinet, 1995; Matsumoto, et al., 2001), even over short (few days) time intervals (Grêt, et al., 2005), thus revealing spatial and temporal resolution to investigate changes of the propagation medium characteristics.

(Ratdomopurbo & Poupinet, 1995), analysed shallow earthquakes recorded on Merapi volcano before the eruption of February 2nd, 1992. A gradual decrease in the arrival times of coda waves was observed, approaching the eruption, with coda waves becoming progressively faster, up to 1.2%.

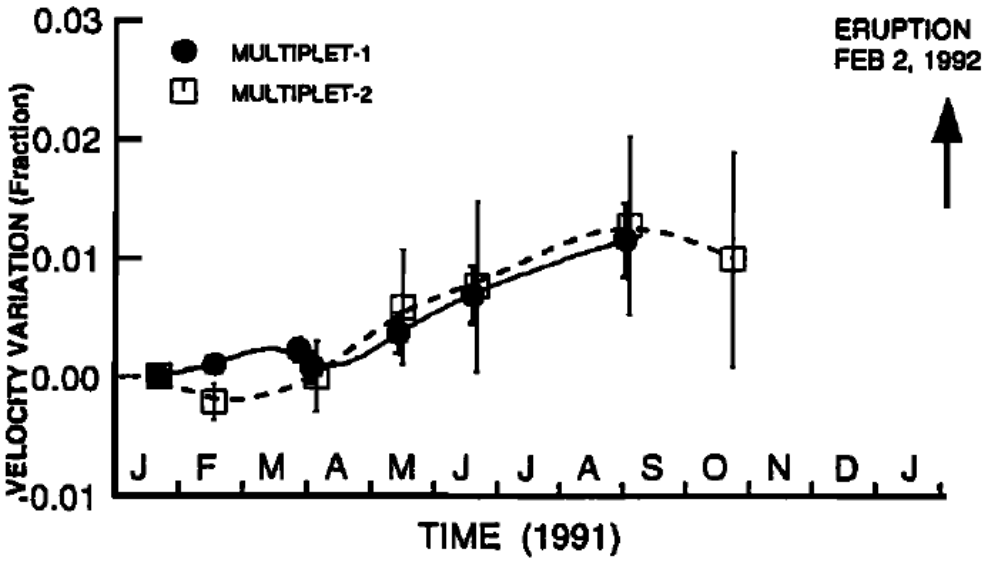

Figure 19. Plot of the S-velocity change measured at PUSV station, on Merapi volcano, as a function of time. The onset of the eruption is marked by the arrow. From Ratdomopurbo & Poupinet, 1995.

The increase in velocity, that was observed 4 months before the eruption, was inferred to be related to an increase in pressure in the magma chamber or in the conduits and to the resulting closure of the surrounding cracks (Ratdomopurbo & Poupinet, 1995).

Grêt, et al., 2006, achieved a similar result examining a repeating seismic source provided by impulsive Strombolian explosions at Erebus volcano. They showed how the seismic coda decorrelates rapidly over a period of several days indicating a rapid change in the scattering properties of the volcano. Changes in the shallow magma/conduit system would not be evaluable using others scattered seismic wave methods.

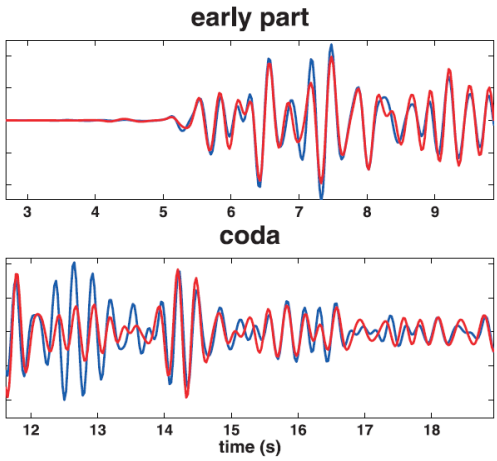

Figure 20. Two vertical–component seismograms recorded at E1S in Mount Erebus with a two–week time separation. The early seismogram correlates very well but there is a significant correlation decrease in the later waveform. From Grêt, et al., 2006.

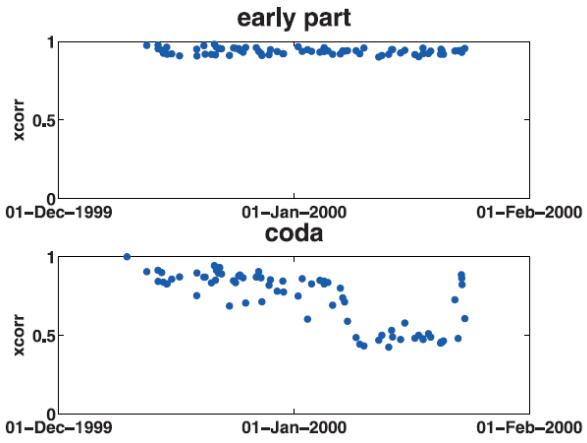

Figure 21. Correlation coefficients for vertical–component Strombolian explosion seismograms recorded at E1S station in Mount Erebus for the early (top) and later (bottom) time segments. All events are correlated with event number 1. From Grêt, et al., 2006.

The limitation of coda wave interferometry is the need of discrete seismic transients, related to natural or induced earthquakes as well as active seismic sources, thus limiting the analysis to well selected areas and/or time periods. To overcome this problem, many authors moved beyond the limitations of methods based on earthquakes, and recovered surface-wave dispersion data from ambient seismic noise.

Cross-correlation of a random isotropic wavefield computed between a pair of receivers will result in a waveform that differs only by an amplitude factor from the Green's function between the receivers. The relation is widely used in a variety of physical applications such helioseismology (Duvall, et al., 1993), acoustics (Weaver & Lobkis, 2001; Derode, et al., 2003; Roux & Kuperman, 2004; Larose, et al., 2004; Malcolm, et al., 2004) and seismology (Campillo & Paul, 2003; Shapiro & Campillo, 2004). Results suggest that such a statistical treatment can be applied to long series of ambient seismic noise, because the distribution of the ambient sources randomizes by scattering from heterogeneities within the Earth when averaged over long periods of times.

Cross-correlating one month of ambient seismic noise (Shapiro, et al., 2005) allowed the reconstruction of tomographic images of the main geological units of California, with low and high-speed anomalies which correspond respectively to the sedimentary basins and the igneous cores.

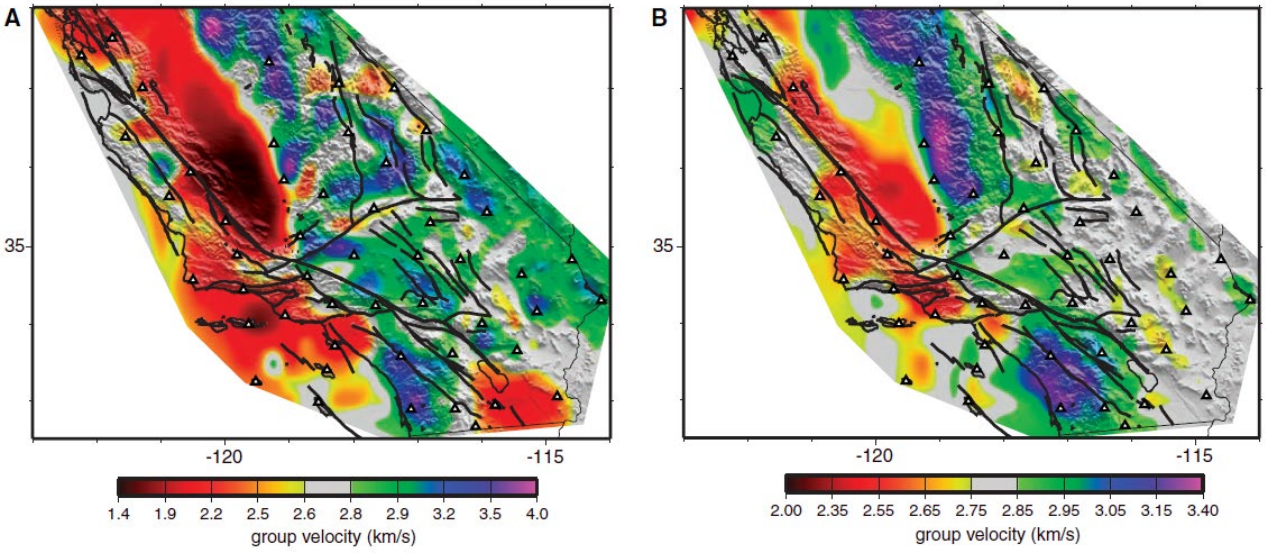

Figure 22. Group-speed maps of ambient noise (Rayleigh waves) interferometric analysis by cross-correlation between USArray stations. (A) 7.5-s-period. (B) 15-s-period. Black solid lines show active faults. White triangles show locations of USArray stations. From Shapiro, et al., 2005.

3.3. GREEN'S FUNCTION, MEDIUM PROPERTIES AND SOURCE LOCATION

In mathematics, a Green's function is defined as the impulse response of an inhomogeneous linear differential operator. The primary use of Green's functions in mathematics is therefore to solve non-homogeneous boundary value problems. In modern theoretical physics, Green's functions are usually used as propagators. In seismology and statistical field theory the term Green's function is often used for various types of correlation functions.

In seismic interferometry the Green's function describes the medium between two receivers through which waves propagate (Aki, 1957; Claerbout, 1968; Lobkis & Weaver, 2001; Roux & Fink, 2003; Schuster, et al., 2004; Wapenaar, 2004; Bakulin & Calvert, 2006; Snieder & Safak, 2006; Wapenaar & Fokkema, 2006). Seismic interferometry is used in a wide variety of applications: ambient noise (Hohl & Mateeva, 2006; Draganov, et al., 2007; Brenguier, et al., 2008; Stehly, et al., 2008; Draganov, et al., 2009; Lin, et al., 2009), traffic noise (Nakata, et al., 2011), production noise (Miyazawa, et al., 2008; Vasconcelos, et al., 2008), earthquake data (Larose, et al., 2006; Sens-Schönfelder & Wegler, 2006; Snieder & Safak, 2006; Ruigrok, et al., 2010) and active sources (Bakulin & Calvert, 2004; Mehta, et al., 2008).

The Fourier's transform is one of the most powerful methods to find Green's functions considering that it has the fundamental property of converting derivative operations into products, and therefore differential equations into algebraic equations.

For the Fourier convention $f(t) = \int F(\omega)e^{-i\omega t}d\omega$, where ω is the angular frequency, the extraction of the frequency domain Green's function for acoustic waves is formulated mathematically by (Snieder, et al., 2007) as:

$$G(x_A, x_B) - G^*(x_A, x_B) = 2i\omega \oint_{\partial V} \frac{1}{\rho(x_S)c(x_S)} G(x_A, x_S)\, G^*(x_B, x_S)\, dS \qquad \text{Eq. 3.7}$$

In this expression $G(x_A, x_B)$ is the Green's function that accounts for wave propagation from x_B to x_A, ρ the mass density, c the wave velocity, and the asterisk denotes complex conjugation.

The integration is over a closed surface ∂V that encloses receivers at x_B and x_A. Since a radiation boundary condition is used in this derivation (Wapenaar & Fokkema, 2005), the closed surface must be sufficiently far from the receivers.

3.4. NUMERICAL ANALYSIS

Along with physics, acoustics and engineering, geophysics rapidly began to employ the extraction of information from random field fluctuations. The widespread application of this idea lead to a variety of different names used for Green's function extraction. The mostly used name in the exploration seismology community is seismic interferometry (Curtis, et al., 2006).

In the next section, I present a preview of three of the main techniques used to perform seismic interferometry and the theory behind them. After that I present the workflow used to analyse data showing different calculation methods and their pros and cons.

3.4.1. THEORETICAL REFERENCES

MSNOISE

MSNoise is a Python package for monitoring seismic velocity changes using seismic ambient noise (Lecocq, et al., 2014). The standard workflow elaborates seismic data to obtain dv/v curves. The program is also used in monitoring frameworks computing the cross-correlation of continuous seismic records and looking for changes in the cross-correlation function relative to a reference. Authors made the program highly configurable keeping the need for coding to a minimum and avoiding being a black box. In this work I am interested only in cross-correlation computation method. Classic workflow leading to Green's function retrieval involves a waveform pre-processing phase and the cross-correlation computation that is the core of program.

Waveform pre-processing remove mean value, apply a taper and merge data to provide a 1-day long traces from different chunks. If the time of a chunk is not aligned, the chunk is phase-shifted in the frequency domain by tapering and fft/ifft. If there are gap between two chunks they can be filled with interpolated values. Each 1-day long trace is then high-passed, then if needed, low-passed and decimated/downsampled.

Once all traces are pre-processed, station pairs are processed. For each window and filter configured in a database, the traces are clipped to windsorizing times the RMS (or 1-bit converted). Data timeseries array are moved to frequency domain using fft and the amplitudes of the spectra are whitened between the frequency bounds. When both traces are ready, the cross-correlation function is computed returning data for time lags corresponding to maximum lag chosen in the acausal (negative lags) and causal (positive lags) parts. Results are saved and made available for further workflow steps starting from stacking.

CROSS-CORRELATION

Let consider random sources generating an acoustic or elastic wave field propagating in a loss-less media and recorded at two receivers. The Green's function extraction of the propagation can be retrieved by cross-correlating recorded signals. Derivations valid for open systems of acoustic waves have been developed using various techniques, among which representation theorems (Wapenaar & Fokkema, 2005; Wapenaar & Fokkema, 2006) that has been extended to elastic waves (Wapenaar, 2004).

Considering a closed surface ∂V that encloses receivers at x_B and x_A, a spatially uncorrelated source q at the boundary ∂V that excite field fluctuations satisfies the following equation:

$$\langle q(r_1)q^*(r_2)\rangle = \frac{|S(\omega)|^2}{\rho(r_1)\, c(r_1)}\delta(r_1 - r_2) \qquad \text{Eq. 3.8}$$

where $|S(\omega)|^2$ is the power spectrum of the noise and $\langle\cdots\rangle$ denotes an ensemble average. This average is replaced by a time average (Larose, et al., 2006) in real cases.

The integral in equation (Eq. 3.7) can be written as $\oiint\left(\rho(r_1)c(r_1)\right)^{-1} G(x_A, r_1)\,\delta(r_1 - r_2)\, G^*(x_B, r_2)dS_1 dS_2$. Together with equation (Eq. 3.8) this gives:

$$G(x_A, x_B) - G^*(x_A, x_B) = \frac{2i\omega}{|S(\omega)|^2}\langle p(x_A)p^*(x_B)\rangle \qquad \text{Eq. 3.9}$$

where $p(r_0) = \oint G(r_0, r)q(r)dS$ are the field fluctuations excited by the random sources on the bounding surface.

If we move from frequency domain to time domain, we can simplify calculations: superposing the causal and time-reversed causal Green's functions we transform complex conjugate to time-reversal, i.e., $G(x_A, x_B) - G^*(x_A, x_B)$ become $G(x_A, x_B, t) - G(x_A, x_B, -t)$. In addition, the product $p(x_A)p^*(x_B)$ becomes a correlation. Expression Eq. 3.9) thus relates the average field fluctuations to the Green's function.

Some considerations about the nature of the signal source are needed.

First, even though one does not need to know the noise spectrum $S(\omega)$, the power spectrum $|S(\omega)|^2$ of the excitation must be known. For the employed normalization the excitation in expression (Eq. 3.8) must be inversely proportional to the acoustic impedance ρc at each source location. For acoustic waves, $p/\rho c$ is proportional to the particle velocity v, hence $|p|^2/\rho c$ is proportional to $p * v$, which is the power flux (Morse & Ingard, 1968). The Green's function can be extracted only if the power flux from every point is constant. This is the property of equipartitioning

of the energy flow, which is shown to be necessary property for Green's function extraction from noise (Lobkis & Weaver, 2001; Snieder, et al., 2007).

Secondly, the noise sources must be placed all over the bounding surface (Eq. 3.7). Even if this constrain is necessary, only sources generating waves that propagate between the receivers contribute to the Green's function extraction. The integrand in expression (Eq. 3.7) is oscillatory indeed. One can show that the dominant contribution to the integral comes from the stationary source positions, where the integrand to first order does not vary with the source location (Snieder, 2004; Snieder & Safak, 2006). The contribution from sources at other locations integrates to zero (Wapenaar & Fokkema, 2005; Mehta, et al., 2008; Snieder, et al., 2008), provided that the source density is sufficiently high to sample the oscillatory contribution to the integral adequately.

In addition, it is useful to normalize the noise before cross-correlation to suppress its variation with time. The simplest method to perform such a normalization is to replace the recorded noise by its sign bit (Larose, et al., 2004), but a variety of other methods have been developed (Bensen, et al., 2007).

Finally, the extraction of the Green's function is not limited to loss-less acoustic waves and its generalization has been extended to elastic waves (Wapenaar, 2004). The principle can also be applied to the diffusion equation, the counterpart of expression (Eq. 3.7) for solutions of the diffusion equation $\partial p/\partial t = \nabla \cdot (D\nabla p)$ is given by (Snieder, 2006) as:

$$G(x_A, x_B) - G^*(x_A, x_B) = 2i\omega \int_V G(x_A, x_S) G^*(x_B, x_S)\, dV \qquad \text{Eq. 3.10}$$

Apart from the absence of the impedance $1/\rho c$ in the integrand, the main difference with expression (Eq. 3.7) is that the surface integral is replaced by a volume integral.

The Green's function extraction by cross-correlation holds for general scalar and vector systems (Wapenaar & Fokkema, 2006; Snieder, et al., 2007; Weaver, 2008). For systems that are invariant for time-reversal the correlation method requires random sources on a bounding surface only, but when time-reversal invariance is broken, for example by attenuation, a volume distribution of sources is needed.

In this thesis I consider two algorithms to perform the cross-correlation, both available in Matlab calculation environment: simple Cross-correlation (xcorr) and Cross Power Spectral Density (cpsd).

Cross-correlation and vector of lags by formula $[c, lags] = xcorr(a, b, maxlag)$, where maxlag is the maximum lag, specified as an integer scalar. The result of xcorr can be interpreted as an estimate of the correlation between the two input signals. The true cross-correlation sequence is given by

$$R_{ab}(m) = E\{a_{n+m} b_n^*\} = E\{a_n b_{n-m}^*\} \qquad \text{Eq. 3.11}$$

where $-\infty < n < \infty$, the asterisk denotes complex conjugation, and E is the expected value operator. By default, xcorr computes raw correlations with no normalization:

$$\widehat{R}_{ab}(m) = \begin{cases} \sum_{n=0}^{N-m-1} a_{n+m} b_n^*, & m \geq 0 \\ \widehat{R_{ab}^*}(-m), & m < 0 \end{cases} \qquad \text{Eq. 3.12}$$

The output vector, c, has elements given by

$$c(m) = \widehat{R}_{ab}(m - N), \qquad m = 1, 2, \ldots, 2N - 1 \qquad \text{Eq. 3.13}$$

The second algorithm provide the cross power spectral density ("cpsd") of two discrete-time signals using Welch's averaged, modified periodogram. Cross-correlation and vector of lags are calculated with formula $[c, lags] = cpsd\,(a, b, window, noverlap, f, fs, freqrange)$ where *window* divide the signal into segments of length *window* and windows each segment with a Hamming window of the same length, *noverlap* is the number of overlapped samples, *f* is the vector of frequencies (in hertz) at which cross-correlation *c* is estimated, *fs* is the sampling frequency specified in hertz and *freqrange* is the frequency range for cross power spectral density estimate.

The distribution of power per unit frequency (cross power spectral density) is defined as:

$$P_{ab}(\omega) = \sum_{m=-\infty}^{\infty} R_{ab}(m) e^{-j\omega m} \qquad \text{Eq. 3.14}$$

The cross-correlation sequence is defined as:

$$R_{ab}(m) = E\{a_{n+m} b_n^*\} = E\{a_n b_{n-m}^*\} \qquad \text{Eq. 3.15}$$

where a_n and b_n are jointly stationary random processes, $-\infty < n < \infty$, and $E \cdot$ is the expected value operator.

Despite which of the two algorithm is used the correlation technique requires a careful data preparation in order to obtain a clean correlation result. Crucial steps in data preparation are time-domain normalization and spectral whitening. The temporal normalization reduces the effect of

earthquakes, instrumental irregularities and non-stationary noise on the cross-correlation (Bensen, et al., 2007). Ambient noise is not spectrally white (i.e., is not flat in the frequency domain), but is peaked near certain frequency especially near microseism (15 s and 7.5 s period) and 50 s period referred to Earth "hum" (Rhie & Romanowicz, 2004). These frequencies can corrupt cross-correlation at correlation lag.

Temporal normalization and whitening, together with common procedures of filtering and trend removing, require a huge amount of time and computing resources so that elaborations over long periods are quite expensive and time consuming. In addition, cross-correlation technique not provides Green's function as well but his convolution with the source function (Eq. 3.6).

DECONVOLUTION

Deconvolution method was first applied to boreholes recordings (Trampert, et al., 1993). This has been extended later to downhole receiver functions (Mehta, et al., 2007). Let us assume that a field is excited with a source at location x_S with frequency spectrum $S(\omega)$. The field at locations x_A and x_B, respectively is given by $p(r_{A,B}) = G(r_{A,B}, x_S)S(\omega)$. The deconvolution of these fields in the frequency domain is given by:

$$V_{AB} = \frac{p(x_A)}{p(x_B)} = \frac{G(x_A, x_S)}{G(x_B, x_S)} = \frac{G(x_A, x_S)G^*(x_B, x_S)}{|G(x_B, x_S)|^2} \qquad \text{Eq. 3.16}$$

While in the correlation approach the power spectrum of the excitation must be known, the second identity of equation Eq. 3.16 shows that the deconvolution does not depend on the excitation at all and it is not necessary to know anything about the source signal. The numerator in the last term of equation Eq. 3.16 describes the correlation of the Green's function that is similar to the integrand of expression Eq. 3.7.

This suggests that correlation and deconvolution are closely related processes and give virtually the same results.

The decorrelation of deconvolution with source spectrum is desirable, but comes at a price. Consider the points x_A and x_B coincidence. In that case the deconvolution in equation Eq. 3.16 reduces to $V_{AA}(\omega) = 1$, which, in the time domain, corresponds to:

$$V_{AA}(t) = \delta(t) \qquad \text{Eq. 3.17}$$

This means that when the receivers are located in the same place, the field obtained by deconvolution vanishes for nonzero time. Physically this means that the deconvolved fields satisfy

a clamped boundary condition (Vasconcelos, et al., 2008) at one of the receivers. This tells us that deconvolution does not give the true Green's function, unless if Green's function also happens to satisfy a clamped boundary condition at that receiver. In that case there would be nothing to record because the field fluctuations would vanish as well at that receiver. Using a perturbation approach allow to bypass the clamped boundary condition.

Suppose that the medium can be divided in a reference medium with field p_0 and Green's function G_0, and a perturbation with associated perturbations p_S and G_S in the field and Green's function, respectively. Two cases may occur: A rough fluctuations of medium generating reflected waves respect a smoothly varying medium; a time-lapse change respect the medium before a time-lapse perturbation, that is a natural approach in monitoring applications (Snieder, 2007).

Suppose one can separate for each source at location x_S the field into the field perturbation and the unperturbed field, and that one deconvolves those fields:

$$V'_{AB} = \frac{p_S(x_A)}{p_0(x_B)} = \frac{G_S(x_A, x_S)}{G_0(x_B, x_S)} = \frac{G_S(x_A, x_S){G_0}^*(x_B, x_S)}{|G_0(x_B, x_S)|^2} \qquad \text{Eq. 3.18}$$

Integration over all sources gives:

$$\int_{\partial V} V'_{AB} dS = \int_{\partial V} \frac{G_S(x_A, x_S){G_0}^*(x_B, x_S)}{|G_0(x_B, x_S)|^2} dS \qquad \text{Eq. 3.19}$$

When the reference medium is smooth, G_0 does not consist of many interfering waves and it is usually a smooth function of frequency. The numerator in equation Eq. 3.19 gives the correlation between wavefield perturbations at x_A and unperturbed waves at x_B. When the source is at such a location that it launches direct waves to x_B that are then reflected by the medium perturbation to propagate to x_A, one retrieves the perturbed waves that propagate from x_B to x_A (Vasconcelos, et al., 2008). In practice one sums over a range of sources near the stationary phase region for these arrivals. This means that sources distributed over a large region include the stationary phase zones even if its precise location and extent is unknown.

In this approach the separation of the unperturbed field from the field perturbations needed. For waves a time gate that separates the direct waves from reflected waves is used. When the duration of the excitation is long, this is not valid and the direction of wave propagation may be used. For example, the direct wave may propagate downward and the reflected waves travel upward. For acoustic waves, the separation can be obtained by dual-sensor summation (Robinson, 1999), when both the pressure and displacement are measured. When multiple sensors are available, the separation can be made by frequency-wavenumber filtering. With a borehole array internal multiple can be used to illuminate a target above the downhole array to provide unique bottom-side images of, for example, a salt dome (Vasconcelos, et al., 2008). In that application the separation between unperturbed and perturbed waves is obtained by beam-steering, illuminating target regions.

Vasconcelos & Snieder (Vasconcelos, et al., 2008) showed results from interferometry obtained both with the correlation and the deconvolution approaches on synthetic data in which the seismic source is a drill bit noise. In the case of a long drill stem, it is difficult to retrieve excitation of waves due to vibrations reverberating in the drill stem itself. In the deconvolution interferometry, according to expression Eq. 3.16, however, the record of the vibrations in the drill stem is not necessary.

Figure 23 left panel shows a borehole geophones array detecting noise produced by a drill bit under the salt dome. Deconvolution interferometry is calculated referring to a different geophone each time. The motion at every geophone is deconvolved with the motion at the reference receiver. The underside reflections propagating from the target receiver to the others geophones of the array highlight the salt body as if physical sources were placed in the instrumented well. The resulting image, shown in the middle panel of Figure 23, clearly reveal the bottom and top of the salt body. Because to the limited aperture of the borehole array, only parts of the salt body are imaged.

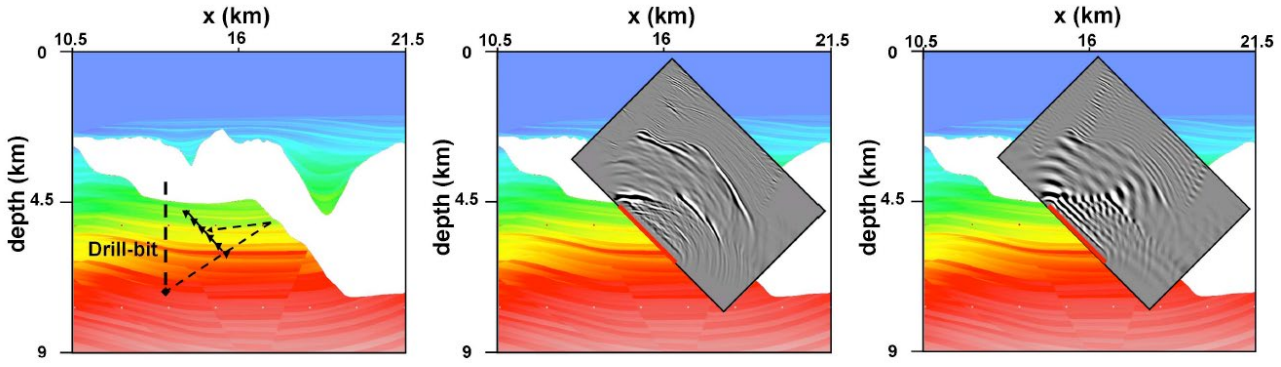

Figure 23. Left panel: subsoil model with a salt body shown in white. Triangles indicate the location of a drill bit receivers in a borehole. Middle panel: result of deconvolution interferometry. Right panel: results of correlation interferometry. From Vasconcelos, et al., 2008.

The right panel of Figure 23 shows what happens if the image is obtained by using correlation instead of deconvolution and using the waves thus obtained to create an image. The image obtained with this approach is dominated by strong reverberations. According to equation Eq. 3.9 one must divide by the power spectrum in the correlation approach to retrieve the Green's function. This division was not carried out in the data processing leading to the image in the right panel on Figure 23, because in practice the power spectrum of the drill bit noise often is poorly known. As a result, the waveforms obtained by cross-correlation are the Green's function convolved with the autocorrelation of the drill bit noise. The resulting image shows pronounced ringing because noise is narrow-band and autocorrelation is oscillatory.

In this thesis I have developed a Matlab algorithm to perform the deconvolution technique.

Let's assume that a and b are one hour of one component data vectors with a defined as reference station (ref). The Fourier transform (FFT) is calculated for both data vectors to move from time domain to frequency domain:

$$\mathrm{DN_{ref}} = \mathrm{fft(a)} \quad \text{and} \quad \mathrm{DN} = \mathrm{fft(b)} \qquad \text{Eq. 3.20}$$

As in rightmost side of Eq. 3.16, deconvolution is calculated as follow:

$$\mathrm{F} = \frac{\mathrm{DN} * \mathrm{conj}(\mathrm{DN_{ref}})}{|\mathrm{DN_{ref}}|^2 + \mathrm{stabilization}} \qquad \text{Eq. 3.21}$$

Where *conj* indicates the complex conjugate, and *stabilization* is the regularization parameter that stabilizes the deconvolution (Snieder & Safak, 2006; Mehta, et al., 2007) defined as

$$\mathrm{stabilization} = \mathrm{mean}(|\mathrm{DN_{ref}}|^2) * \mathrm{percent} \qquad \text{Eq. 3.22}$$

where *percent* is the percentage of stabilization required. In this work *percent* is set to be = 0.4.

All the deconvolved data are transposed back to time domain with the inverse Fourier transform (IFFT).

$$\mathrm{D} = \mathrm{ifft(F)} \qquad \text{Eq. 3.23}$$

3.4.2. DATA ANALYSIS WORKFLOW

Hereafter I describe the workflow used to elaborate data with cross-correlation method both in time and frequency domain and deconvolution method. All the elaboration and analysis were performed by Matlab, which is an environment for numerical calculation and statistical analysis written in C.

The algorithm involves a cycle through all the entire reference time period and acquiring station pair as shown in the following flowchart (Figure 24).

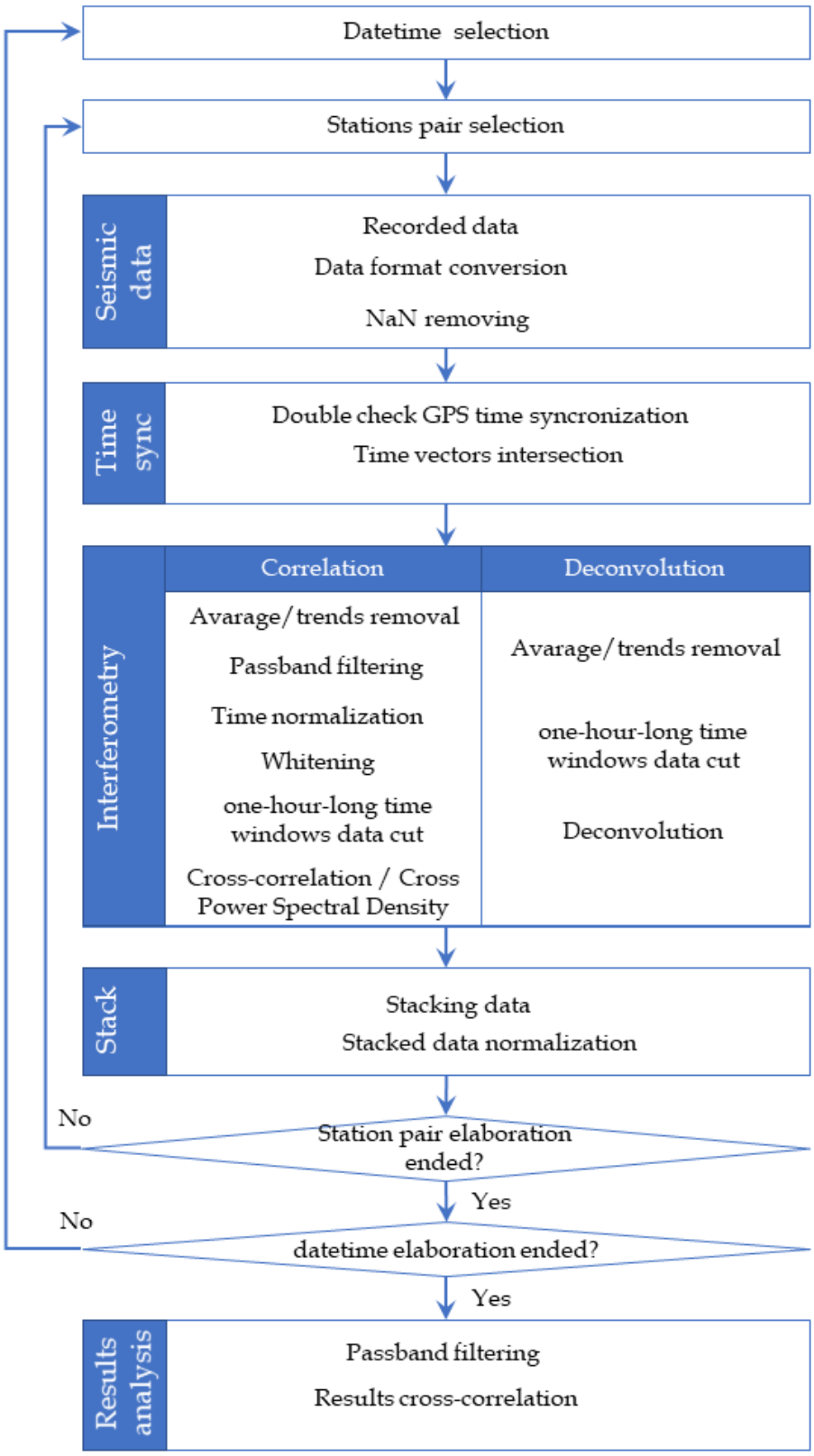

Figure 24. Flowchart of the proprietary software used to elaborate data with cross-correlation method both in time and frequency domain and deconvolution method.

Matlab is optimized to work with his own data format that is ".mat" file extension. Due to different data format for input data, a dedicated algorithm has been created to convert and merge together all those files in a structure of one day of all components data. During this elaboration step all non-numeric data (NaN) were removed.

Time accuracy is the most important issue of all processing algorithm. This is why all seismic stations need to be equipped with GPS receivers, providing not only geographical positioning but above all coordinated universal time. A time vector intersection between station pairs has been performed to double check time synchronization and, if necessary, to recover correct time of each data sample: time vectors for each station are compared to find common values. Extracted indices allow to find associated values for all seismic components.

At this point I applied two different algorithms to evaluate Green's function: Correlation, performed by both *xcor* and *cpsd* Matlab functions, and Deconvolution, performed by proprietary algorithm.

As described in section 3.4.1, correlation method requires some data pre-treatments: time domain normalization and spectral whitening are crucial to obtain a good cross-correlation. A dedicated algorithm has been created to prepare data to further elaboration. In this step averages and trends are removed and a passband filter is applied. Filter limits have been parametrized in order to allow a simple data management. Different methods can be applied to obtain temporal normalization. These include: i) "one-bit" normalization, ii) application of a clipping threshold equal to the RMS (Root Mean Square) amplitude of the signal for the given time period, iii) automated detection and data removal if the amplitude of the waveform is above a critical threshold, iv) running-absolute-mean normalization. In the algorithm developed within this research I apply the "one-bit" normalization. For each element of data vector, it returns 1 if the element is greater than zero, 0 if it equals zero and -1 if it is less than zero. This method that is the most aggressive method because it retains only the sign of the raw signal but it has been shown to increase signal-to-noise ratio and to be faster than other. After the time domain normalization, I apply a whitening function. This function generates flat Fourier spectrum for the input signal, either for the full range from 0 Hz to the Nyquist frequency, or for a user defined frequency band. In detail the process tapers the signal by applying a Hanning window, evaluates the Fourier Transform (FFT), normalises its magnitude and eventually applies the Inverse Fourier Transform (IFFT). This operation tends to sharpen both the signal and the noise. One hour of data are elaborated with two different correlation functions based on cross-correlation (xcorr) cross-power spectra density (cpsd), where both functions are integrated in Matlab. Analysis is performed in the time domain considering a 50% overlap (30 minutes) in the data time window.

Deconvolution technique in order to retrieve Green's function is a relatively new method that allows avoiding correlation technique constrains. This method allows to overlook data preparation requested for correlation but to watch out for single deconvolution stabilization parameter that works as a low pass filter. In addition, deconvolution method provides Green's function as well allowing constraining physical process developments (refer to section 3.4.1).

Correlated/deconvolved data are stacked together in order to highlight the Green's function peak and reduce noise. This procedure is basically a point-by-point summation of correlated data vectors. Elaborated data staking has been performed over 1 day. Stacked data have been normalized over number of windows.

3.4.3. METHODS COMPARISON – RESULTS ON MISTI DATASET

In this paragraph I compare cross-correlations in temporal and frequency domain with deconvolution on same data set. Deconvolution technique gives better results in terms of stability, signal to noise ratio and time of calculation.

After understanding the validity of both methods previously described, I verified the correspondence of the results provided by the two techniques to evaluate which was most performant in term of result quality and data processing speed for real time purposes. To do that, I wrote a program in Matlab and compared results with the output from MSNoise.

For this purpose, I analysed data recorded on the Misti volcano, in Perú, from 2011/05/30 to 2011/07/31 by two stations M04 and M23 (Figure 25), kindly provided by Prof. Denis Legrand and Diana López from UNAM (Universidad Nacional Autónoma de México).

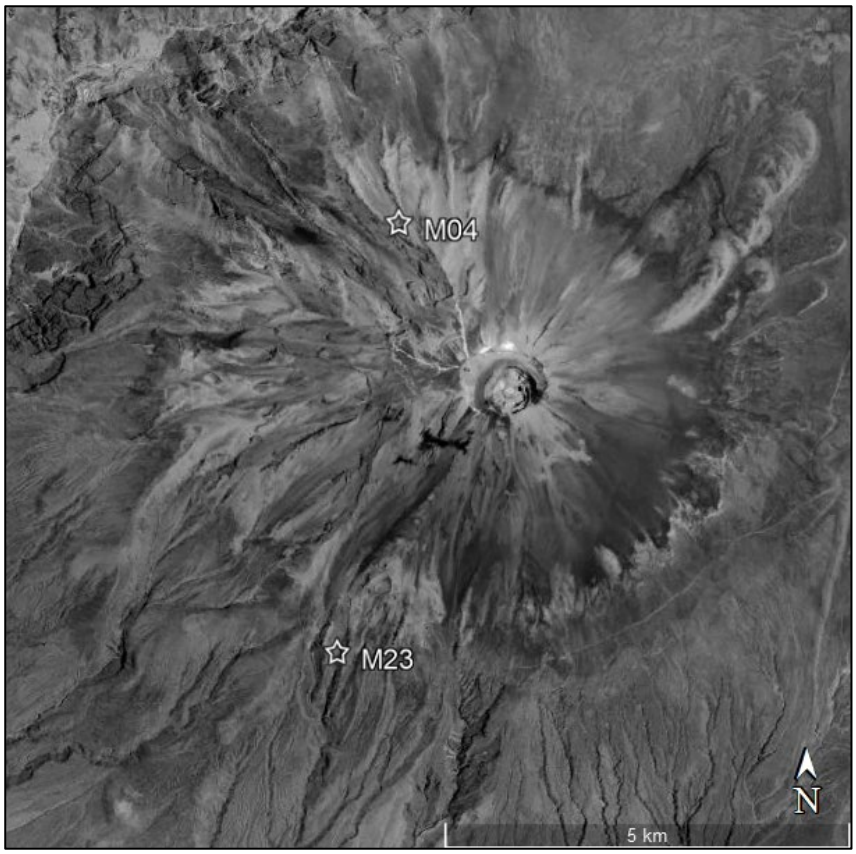

Figure 25. Location of stations deployed on Misti volcano.

The two stations M04 and M23 are located at 2 km North-West and 3.5 km South-West respectively from the crater (Figure 25). The two stations were equipped with three components broadband seismometers and data was sampled at 25 Hz and recorded in daily files.

Following the procedure described by Bensen (Bensen, et al., 2007), I first corrected the seismic data for the instrument response, and removed the mean and trend values. Data were divided into 900-second-long time windows with no overlap, band-pass filtered between 0.15 and 3 Hz, and were normalised by applying a one-bit normalization in time domain. Eventually, data were whitened and cross-correlated and all windows were stacked together.

Input data format and my personal experience using Matlab computing environment led me to develop a proprietary Matlab software benchmarked against the widely-used and well-established reference package for ambient noise interferometry MSNoise software. The developed software reproduces steps of MSNoise in cross-correlation calculation.

As previously discussed (section 3.4.1), I use two different type of correlation: xcorr function to analyse correlation in time domain, and cpsd to analyse correlation in frequency domain.

Results obtained from these three techniques are fairly comparable (Figure 26).

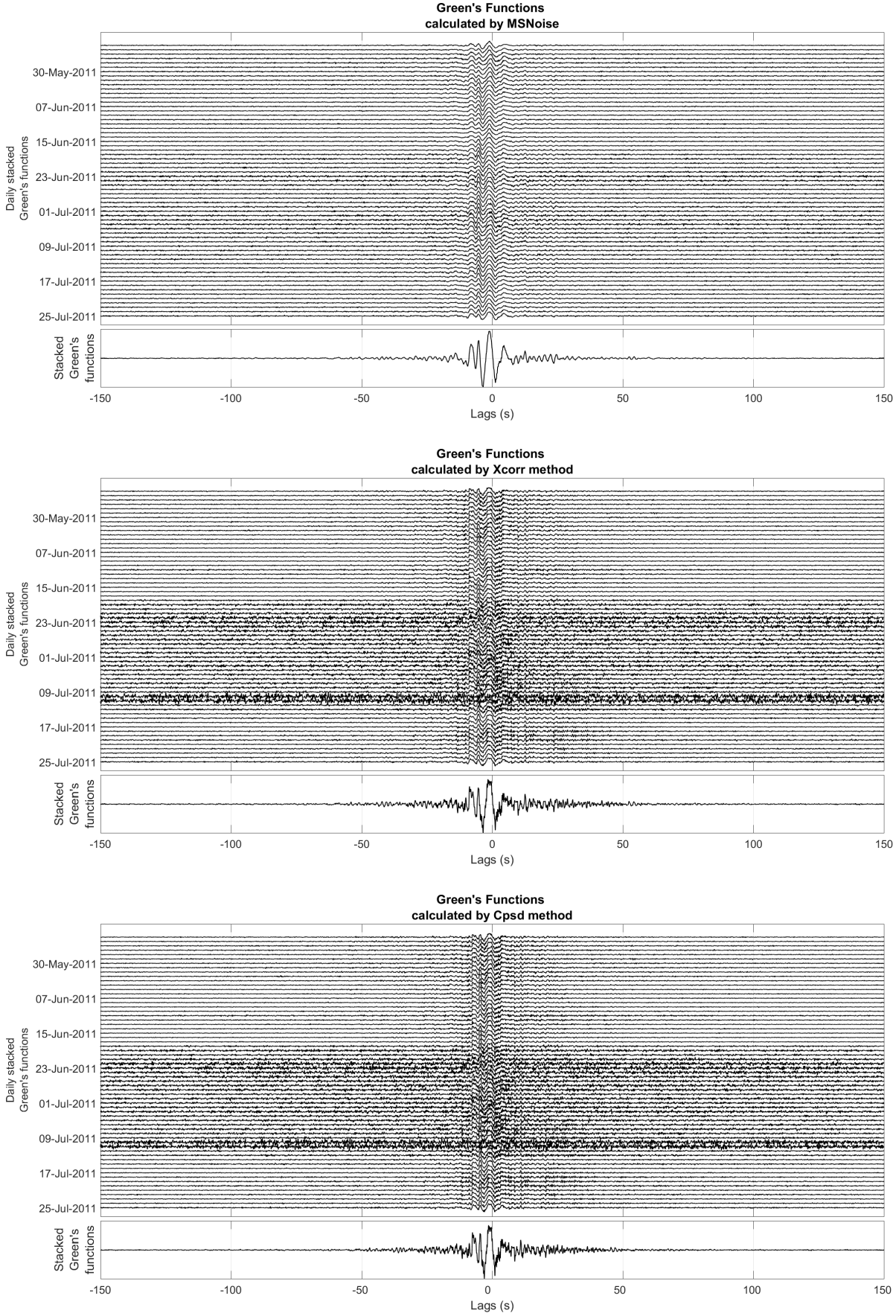

Figure 26. Daily stacked Green's functions and stacked Green's Function over available data, calculated by MSNoise, Xcorr and Cpsd methods.

The percentage of similarity between results of techniques is 97.3% ± 0.3%. The main differences concern the Green's function amplitude, mainly for data over ±25 seconds lag where the amplitude provided by my Matlab algorithm results higher than MSNoise, resulting in a noise increase. This effect could be due to the fact that MSNoise data is decimated/downsampled, resulting in a smooth input signal. However, the Green's function main peak is the same both in amplitude and shape (Figure 27).

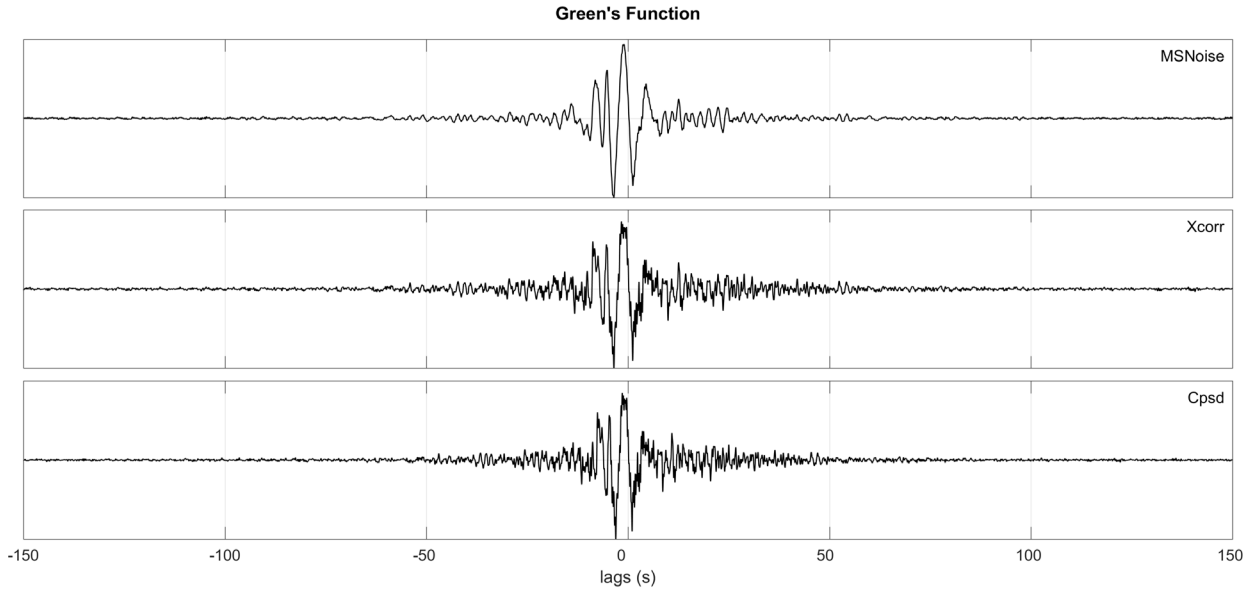

Figure 27. Comparison between all stacked Green's Function calculated by MSNoise, Xcorr and Cpsd.

This peak indicates the maximum of the correlation and the corresponding lag time. In this case, the lag time of the Green's function maximum is −3.52 s, which corresponds to the time difference for the seismic wave to arrive to M23 station with respect to M04 station.

Interferometric studies by Dr. Diana López (University of Mexico City, UNAM, Master Thesis), confirmed by previous geophysical a geochemical studies, show a low velocity anomaly at southwest of the crater interpreted as result of a hydrothermal system. This study shows also a shallow low velocity anomaly probably due to different materials between the two sides of an active fault with northwest direction that leads to volcanic crater. In this work I am interested mostly in comparing methodologies so that no distinction has been made in depth and all frequencies have been processed together.

Additionally, I processed the same data-set with the deconvolution algorithm. Differently from the cross-correlation method, no data treatment is required before elaboration except the correction of instrument response, the removal of the mean and trend values and the division into 900-second-long time windows. Filtering, one bit normalization and data whitening is not required, thus making the analysis much faster. All windows are processed and stacked together in a single result, as it was done with the previous techniques (Figure 28 and Figure 29).

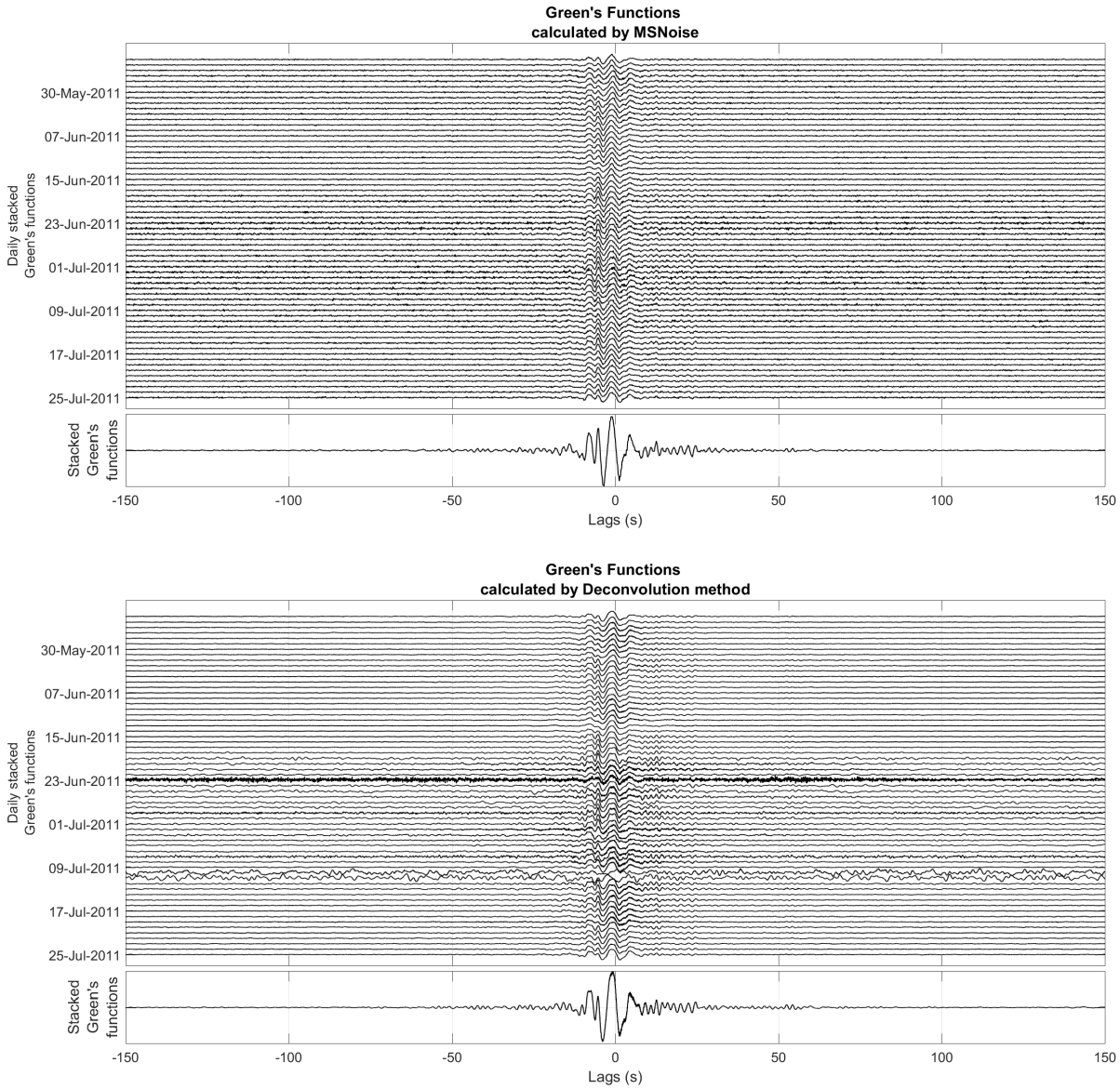

Figure 28. Daily stacked Green's functions and stacked Green's Function over available data, calculated by MSNoise and Deconvolution methods.

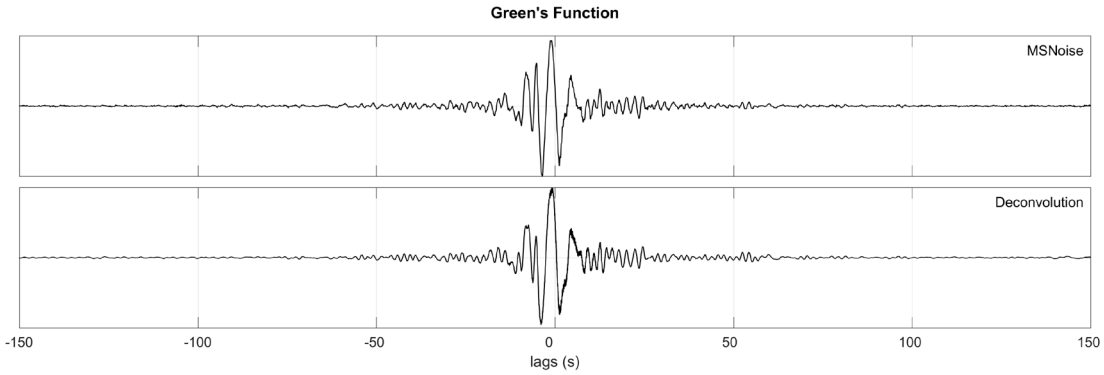

Figure 29. Comparison between all stacked Green's Function calculated by MSNoise and Deconvolution.

In this case, the percentage of similarity between the results of the two techniques is 98.6%, which is better than that of the time cross-correlation (Figure 27). Similarly to what obtained for the cross-correlation approach, the main differences with results obtained from MSNoise concern the amplitude of the Green's function, mainly for data over ± 25 seconds lag, where the amplitude of Matlab deconvolution algorithm results lower than MSNoise reducing noise. The Green's function main peak is the same both in amplitude and function form (Figure 29).

Figure 27 and Figure 29 clearly show that both approaches (cross-correlation and deconvolution) provide extremely good results. Therefore, I performed an efficiency test to consider the computing time, which is critical when the procedure is applied to real-time data analysis. To do that, I select one day of data and I calculate how much time is needed to process raw data in Green's function output. For each method, I run the algorithm 10 times and I calculate a mean computing time. The efficiency of the method was computed via Eq. 3.24 setting 100% of efficiency for the fastest method.

$$\text{efficiency} = \frac{\text{mean}_\text{m} - \text{dev}_\text{m}}{\text{mean}_\text{f} - \text{dev}_\text{f}} \qquad \text{Eq. 3.24}$$

I found that deconvolution method is at least twice faster than other methods (Table 2)

Method	Min (sec)	Max (sec)	Mean (sec)	Deviation (sec)	Efficiency (%)
Xcorr	1,695803	2,057073	1,830707	0,150897	47%
Cpsd	2,044772	2,448425	2,181918	0,168793	39%
Deconvolution	0,780255	0,829909	0,801158	0,015715	100%

Table 2. Algorithm efficiency comparison.

Considering the quality of the results (Figure 29) and the fast execution time (Table 2), I think that the deconvolution method is the best to retrieve Green's function, particularly in the perspective of real-time monitoring purposes. Therefore, results presented in this work are achieved by using the deconvolution method developed in Matlab.

4. SEISMIC INTERFEROMETRY AND TREMOR ANALYSIS APPLIED TO DATA COLLECTED AT STROMBOLI VOLCANO

4.1. INTERFEROMETRIC ANALISYS ON STROMBOLI DATASET

According to the results presented and discussed in section 3.4.3 where the different techniques used for seismic interferometry have been compared using seismic data collected on Misti volcano, I use deconvolution method for the rest of my study the seismic.

Since the deployment of the geophysical network in early 2003, the continuously recorded datasets allowed to follow the evolution of the activity of Stromboli volcano. During this period, the volcanic activity of Stromboli experienced dramatic changes, with three effusive eruptions (2002-2003, 2007 and 2014), four paroxysms (April 5, 2003, March 15, 2007, July 3 and August 28, 2019), tens of major explosions and several overflows alongside ordinary activity that counts hundreds of small explosions per day and continuous degassing. This unique dataset allows to describe Strombolian activity in all its variability and to discuss transition between different explosive regimes.

The analysis is applied to data collected by the seismic network of Stromboli volcano over a period of 4 years between 2016 and 2020.

Within analysis workflow described in section 3.4.2, data are analysed and compared. In order to highlight main Green's function peak, a span of 10 seconds is defined around the peak. Stacked data have been clipped according to the chosen span. In this step it is also possible to apply a filter. The choice to apply the filter only at this stage allows to have all data information up to this point.

Changes in Green's function through time are expressed in terms of changes of the Green's function obtained from deconvolution at a given time, with respect to a reference Green's function. There are different possible choices of a reference Green's function: stack of the entire period, the first Green's Function in the period considered, stack of a time period before the study period, linear inversion that does not depend on the choice of a specific period for calculating the reference Green's Function and so on.

I analysed many methods to choose which one is the most performing, in particular I compared the first Green's function in the period considered and that one retrieved stacking the entire period: the two Green's function appear to be very similar with some minor noise that is obviously reduce in the last one (Figure 30). This means the substantial stability of the Green's function in time and is also reflected in the outcome results of the interferometric analysis that are fairly comparable (Figure 31).

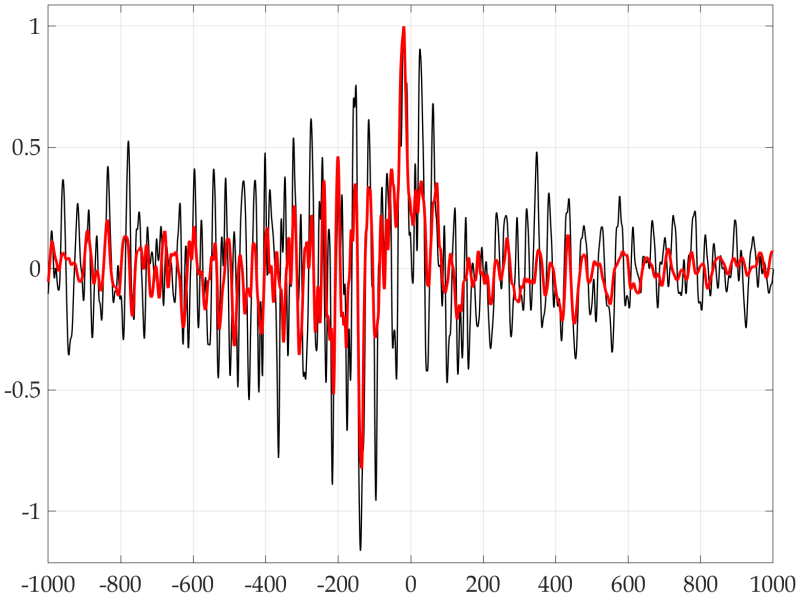

Figure 30. Reference Green's functions comparison: the Green's function of the first day (black) is fairly comparable with that one calculated for the entire 4 year long period (red) where the noise is obviously reduced. Both Green's function are normalized for comparison.

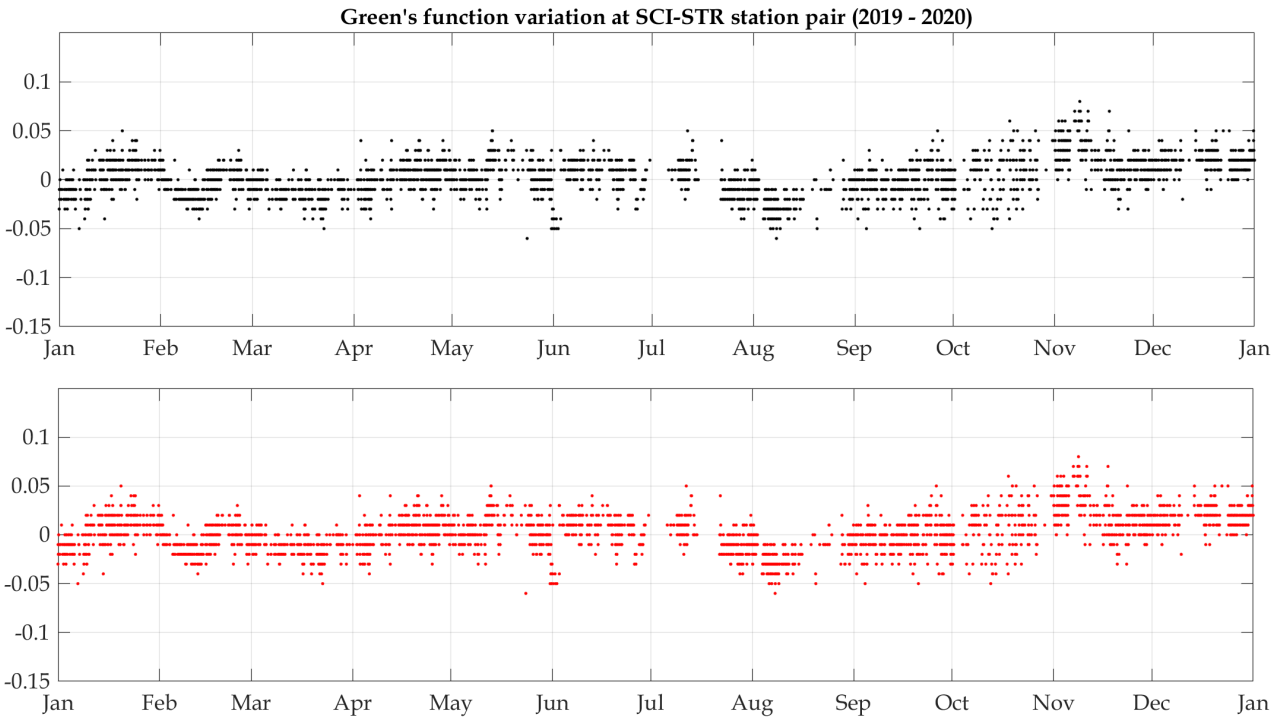

Figure 31. Green's function variation for 2019 dataset evaluated respect the first Green's function of the series (black) and the "mean" Green's function over 4 years long dataset (red). Both analysis show same results.

Ease and computational speed led me to evaluate changes in Green's function through time in terms of changes of the Green's function obtained from deconvolution at a given time, with respect to the Green's function calculated for the first available time window.

Again, there are different methods to measure changes in the Green's functions, like cross-correlation, moving-window cross- correlation, stretching, dynamic time warping (Mikesell, et al., 2015). In this work I choose the cross-correlation method.

Cross-correlation analysis highlights the absolute degree of correlation and the corresponding time lag. Indeed, I express discrepancies in terms of differences in lags of Green's functions, i.e., Δt. Here I show results of Green's functions correlation for station pairs taking SCI (Figure 32) and SDK (Figure 33) as reference stations. Such stations have been chosen because of their position within the monitoring network operated by L.G.S. of the University of Florence on Stromboli volcano: SCI in particular is deployed at the lowest elevation and thus allows us to evaluate the highest inter-station distance (SCI – STR station pair), whereas SDK is the only seismic station located on the southern side of Sciara del Fuoco and allows us to evaluate possible variation across the feeding system area.

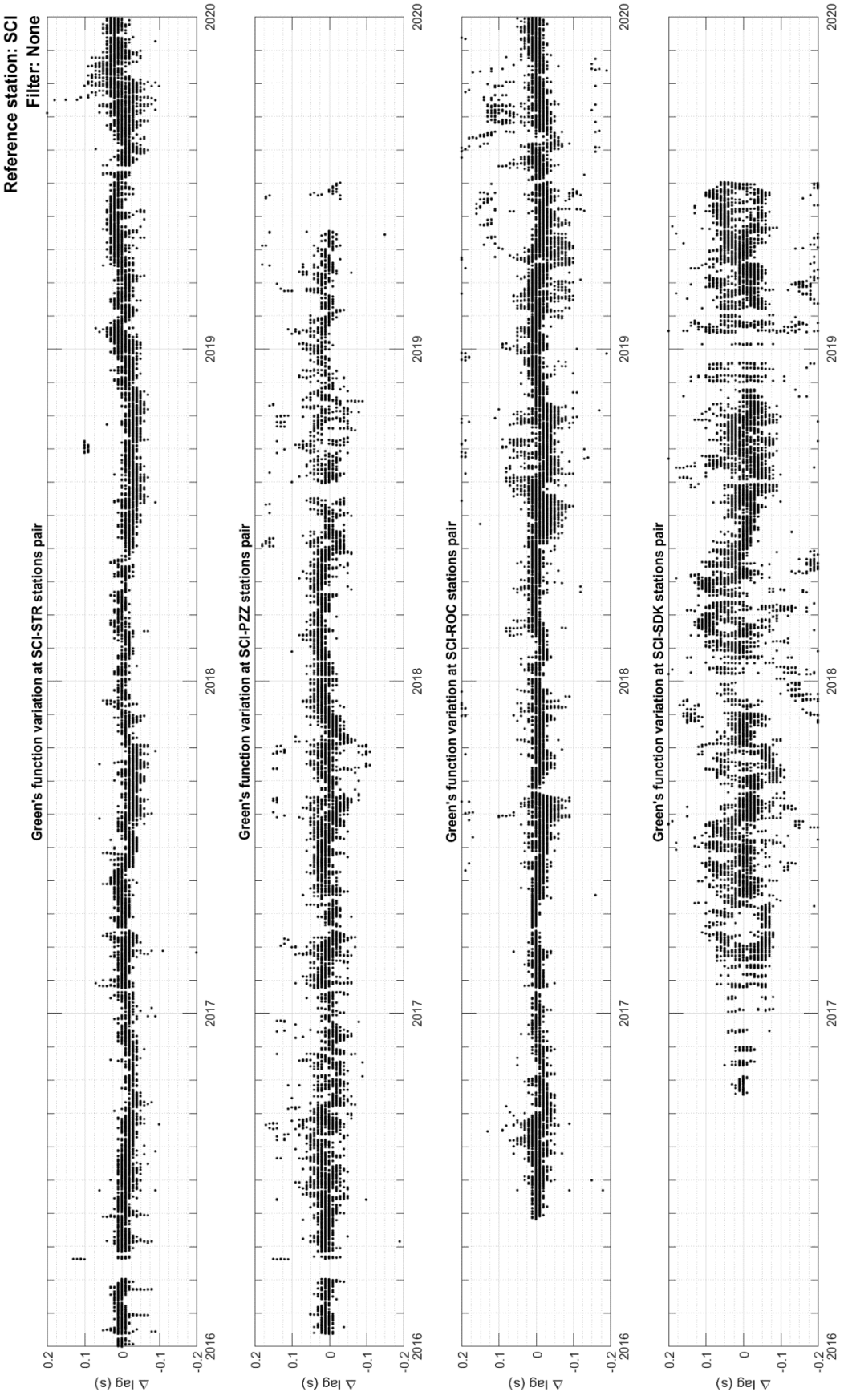

Figure 32. Green's functions variations at stations pairs a) SCI-STR, b) SCI-PZZ, c) SCI-ROC, d) SCI-SDK over a time period of 4 years (2016-01-01 - 2019-31-12). Reference station is SCI.

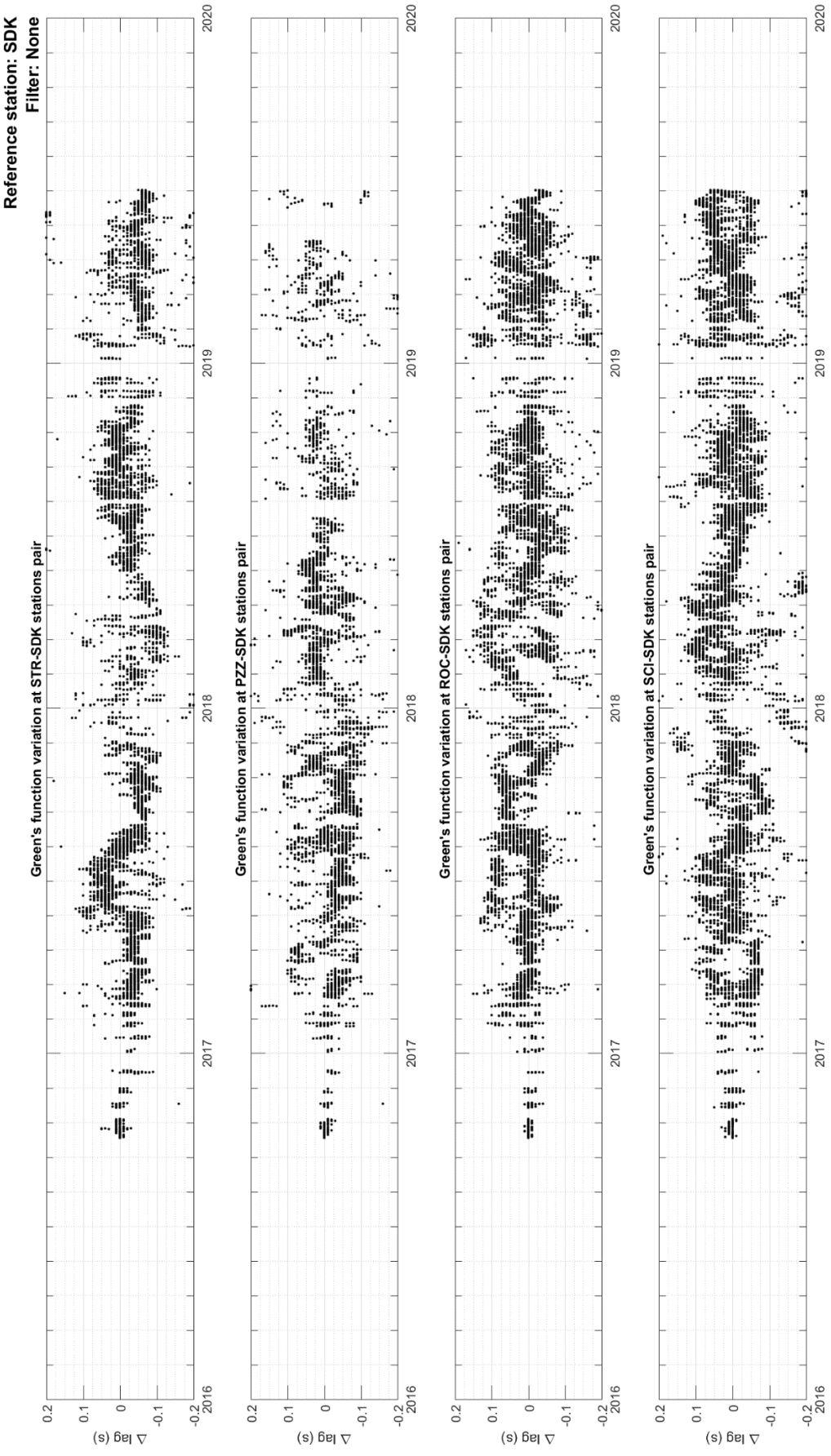

Figure 33. Green's functions variations at stations pairs a) SCI-STR, b) SCI-PZZ, c) SCI-ROC, d) SCI-SDK over a time period of 4 years (2016-01-01 - 2019-31-12). Reference station is SDK.

4.2. TREMOR ANALISYS

In this study I considered volcanic tremor recorded at Stromboli volcano over a period of 4 years and analysed that in order to fully characterize its amplitude, spectral content and possible variation with time. Data were provided by all available stations that are equipped with a Guralp CMG/40T broadband seismometer (see section 2.3).

4.2.1. TREMOR AMPLITUDE BY ROOT MEAN SQUARE (RMS)

Tremor amplitude has been calculated with the Root Mean Square (RMS) method. It is formally defined as the square root of the arithmetic sum of the square of the components (x_i) of seismic velocity recorded through time, divided by the number (n) of components.

$$\mathrm{RMS} = \sqrt{\frac{x_1^2 + x_2^2 + x_3^2 + \cdots + x_n^2}{n}} \qquad \text{Eq. 4.1}$$

A Matlab dedicated algorithm has been created to calculate tremor amplitude. First of all, the program converts and merges together all ".gcf" files into a structure of one day of all data components. During this elaboration step all non-numeric data (NaN) are removed. Averages and trends are also removed and a bandpass filter is applied. Data are divided in one-hour-long windows and amplitude is calculated according to Eq. 4.1 for every window.

For the specific case of volcanic tremor at Stromboli, which is characterized by a mean frequency of 1.6 Hz, I calculated the RMS considering n=360000 samples that corresponds, considering the sampling frequency of 100 Hz, to a time window of 1 hour. RMS is calculated on data band-pass filtered between 0.9 and 10 Hz, in order to include the tremor peak amplitude and to reduce the contribution of low frequency signal, commonly associated to rough sea and bad weather, and high frequency signal, commonly produced by wind.

The window was shifted minute by minute producing a time series of 1440 samples per day, that is representative of time evolution of volcanic tremor amplitude over a period of one day. Eventually the time series is smoothed and down sampled to 1 sample every 15 minutes to highlight variation of volcanic tremor over a longer time period of 4 years (Figure 34).

Figure 34 shows that tremor is very consistent at the different stations of the monitoring network and fluctuated in amplitude over various time scales. A general increase of volcanic tremor was recorded in the winter of 2018 and 2019, yet this could be affected to some degree by rough sea conditions typical of the winter months. An increased volcanic tremor is however recorded also in the summer of 2017 and in the summer of 2019, during period of increased volcanic activity. The phase of increased volcanic activity recorded in 2019 in particular was punctuated by the most recent paroxysmal explosions.

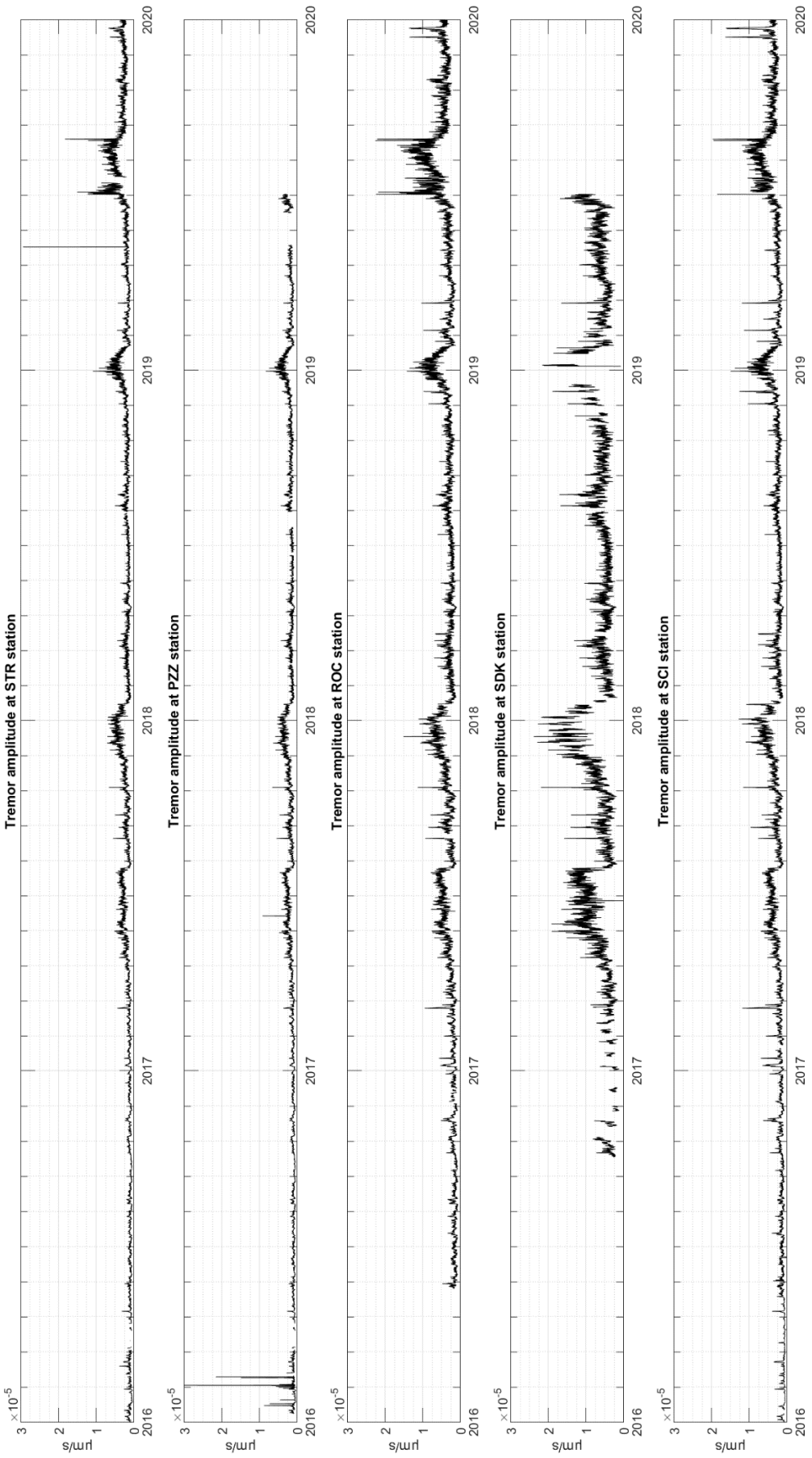

Figure 34. Tremor amplitude at all available stations over a time period of 4 years (2016-01-01 - 2019-31-12).

4.2.2. TREMOR FREQUENCIES BY ZERO-CROSSING

RMS shown in Figure 34 is only showing the amplitude variation of volcanic tremor, while it is lacking any information on its spectral component. The only constraint is indeed the band-pass filtering applied to the data before the RMS is calculated by equation Eq. 4.1, that is limiting the analysis to a limited frequency band but is not providing indication on the precise frequency component. Such an information can be derived with spectral analysis. For the long term analysis, I applied a zero-crossing.

In this work I calculate fundamental frequency of volcanic tremor using zero-crossing method applied to auto-correlation function instead of spectral analysis. A zero-crossing is a point where the sign of a mathematical function changes (e.g., from positive to negative), represented by an intercept of the axis (zero value) in the graph of the function. It is a commonly used in electronics, mathematics, acoustics, and image processing. It is possible to retrieve fundamental frequency of a time domain function by applying zero-crossing function: I used this technique to derive the most representative frequency in the variations of tremor amplitude.

In order to give an example of this technique, I analysed a window of one week of seismic data filtered in tremor frequency band (1 – 10 Hz) (Figure 35). I calculated the autocorrelation function of this window and I detected every time that the function crossed the zero value (Figure 35, b). I counted the values of zero-crossing over time and I obtained a linear fit (Figure 35, c). The angular coefficient of the fit line is the zero-crossing frequency representative of the tremor frequency.

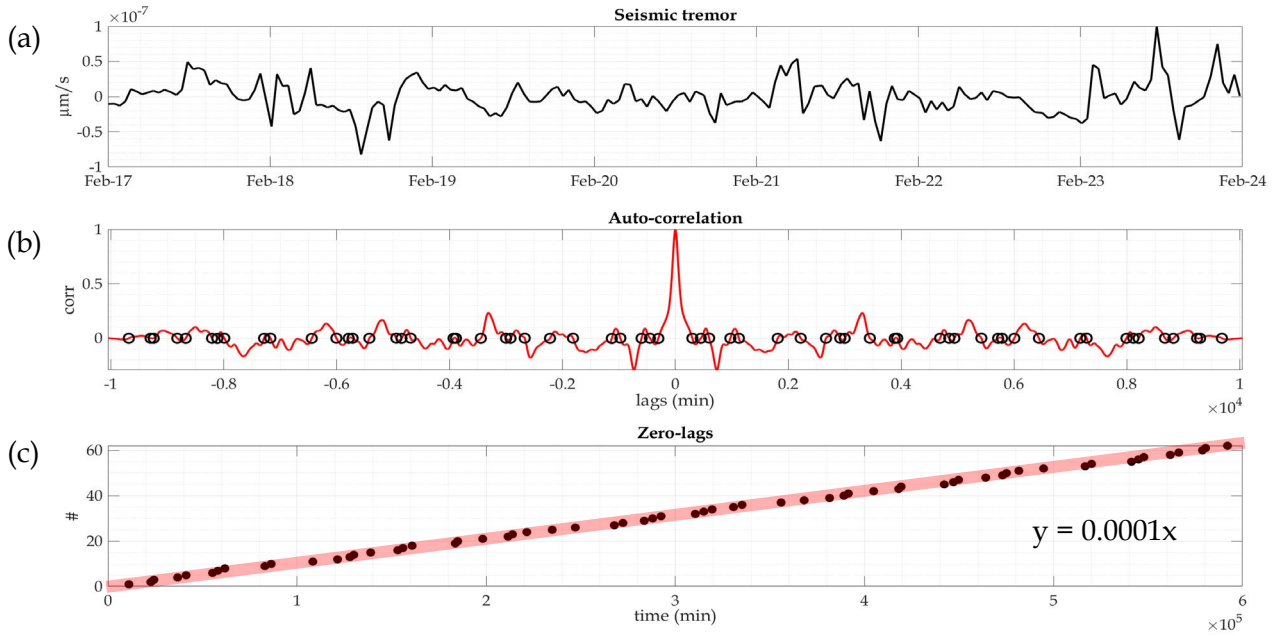

Figure 35. Tremor fundamental frequency calculated by zero-crossing technique. (a) Tremor amplitude of one-hour long window. (b) Auto-correlation function of tremor data: black circles indicate where the auto-correlation function crosses zero. (c) Zero-lags plot: red line is a linear fitting and its slope represent tremor frequency.

I applied this technique to represent the entire dataset with elaboration windows of one week. Volcanic tremor appears to have a quite constant frequency content, that is similar at the different seismic stations (Figure 36).

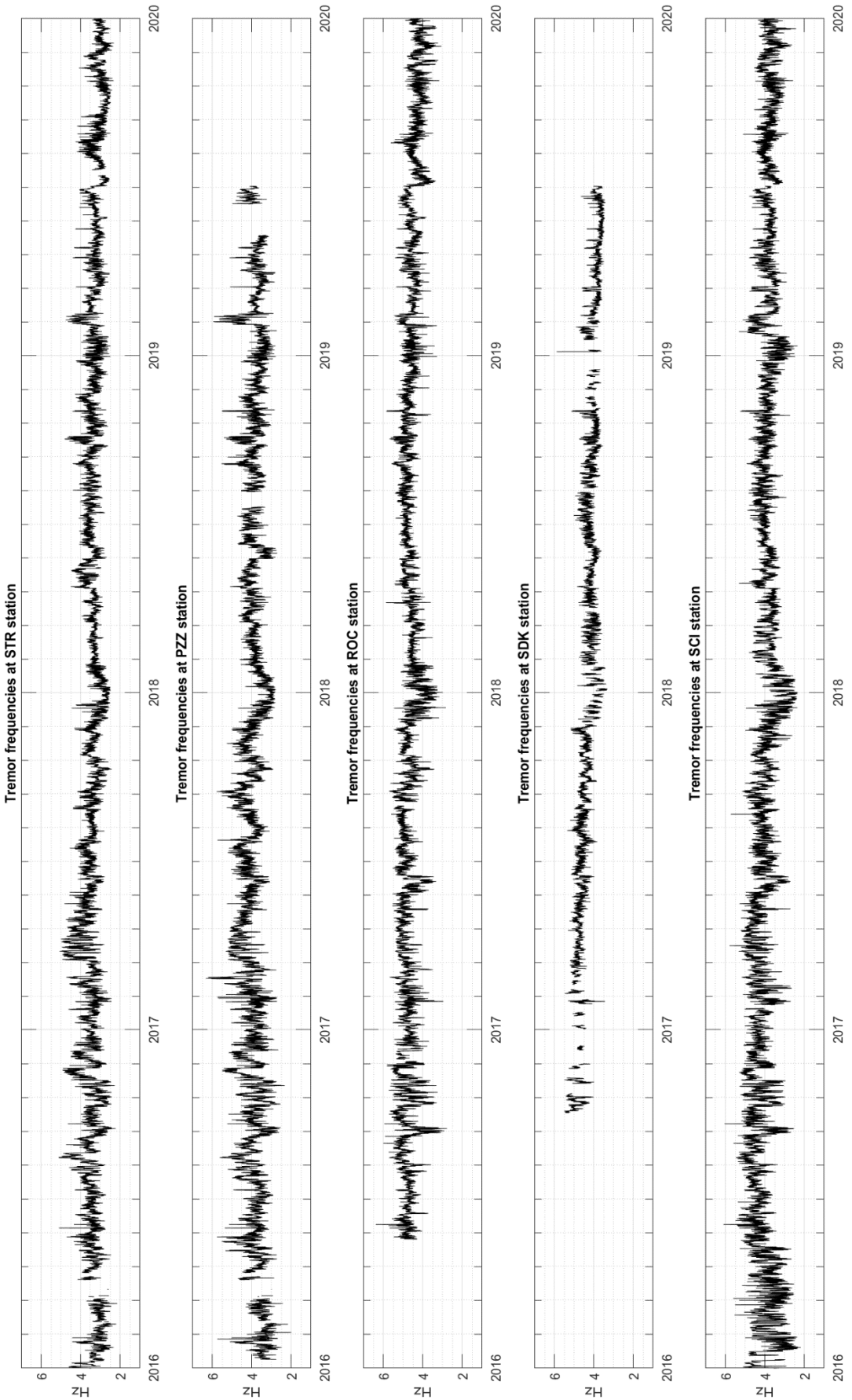

Figure 36. Tremor frequencies at all available stations over a time period of 4 years (2016-01-01 - 2019-31-12).

5. DISCUSSION

5.1. SEISMIC INTERFEROMETRY

According to previous studies (Grêt, et al., 2006), by applying seismic interferometry it is possible to evaluate changes in source position or in medium properties depending on which part of the seismic signal is analysed: respectively the early part (i.e., delay time of firsts arrival) or the coda (see section 3.2). Given the recurrence of VLP signals in the seismic record at Stromboli volcano, usually 10 – 12 events/hour, I studied the influence of such kind of signal on the interferometry results.

I found that the delay-time of noise-coda waves on both frequency bands are strongly affected by local seismicity. I therefore suggest that at Stromboli volcano changes in the time lags between the Green's functions are reflecting changes in the delay times between the seismic events rather than changes in seismic velocity. In this case, interferometric analysis is rather reflecting changes in the position of the VLP source.

In order to investigate the entire dataset, I applied the proposed interferometric analysis to all 5 seismic stations of the monitoring network and over a period of 4 years, spanning from January 2016 to December 2019. In this thesis I always refer to SCI and STR station both showing data results and data comparison. This choice depends on the continuity of the data set for this station pair. However, all discussions are valid for all the other data processed.

The Green's function variation presented in Figure 32 and Figure 33, have been filtered in two different frequency bands: low frequency band (0.03 – 0.3 Hz) (Figure 37 and Figure 38) and high frequency band (1 – 10 Hz) (Figure 39 and Figure 40). Those two filter bands seem to be the best to perform evaluations of source position and medium characteristics variations.

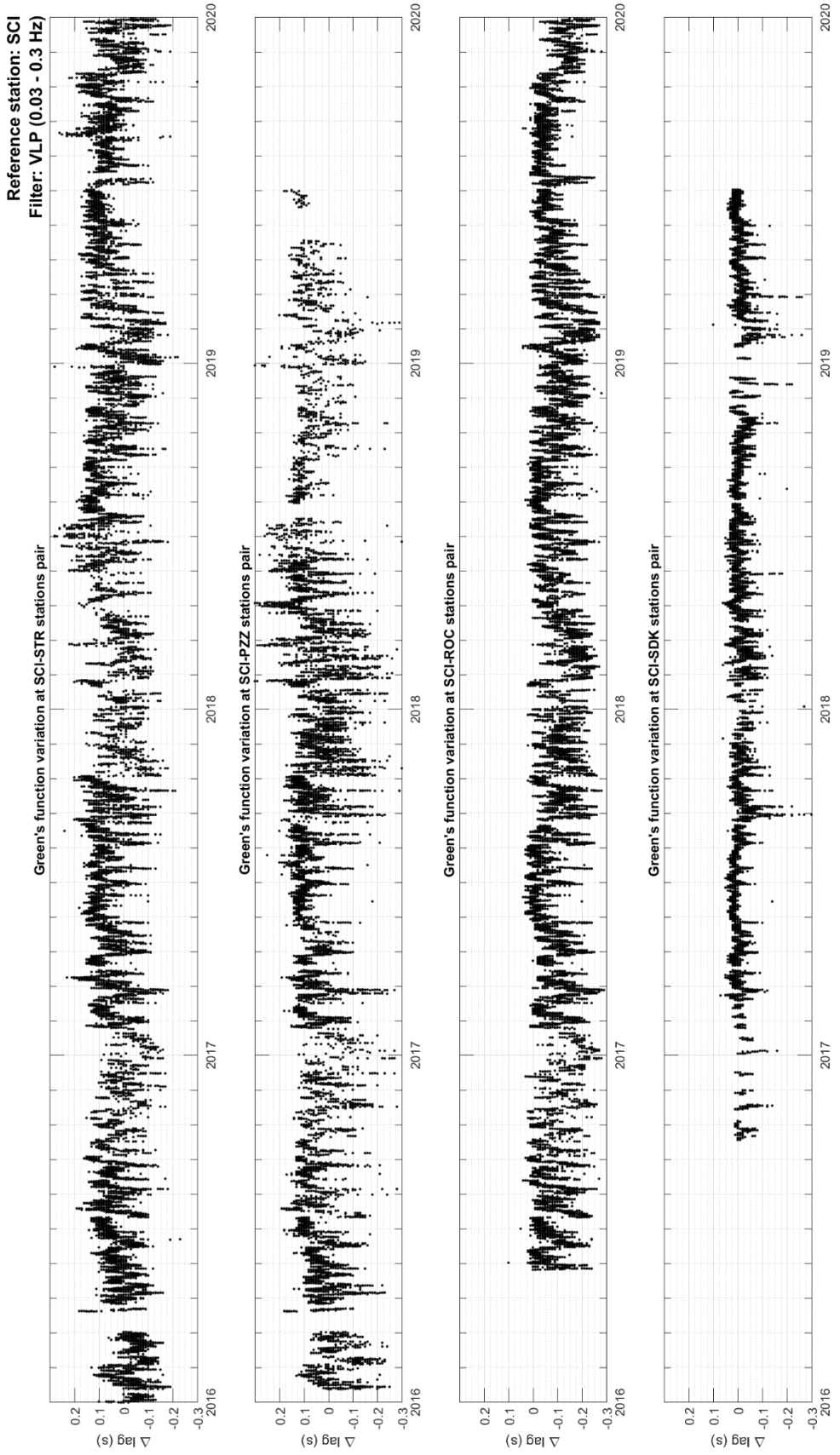

Figure 37. Green's functions variations filtered in low frequency band (0.03 - 0.3 Hz) at stations pairs a) SCI-STR, b) SCI-PZZ, c) SCI-ROC, d) SCI-SDK over a time period of 4 years (2016-01-01 - 2019-31-12). Reference station is SCI.

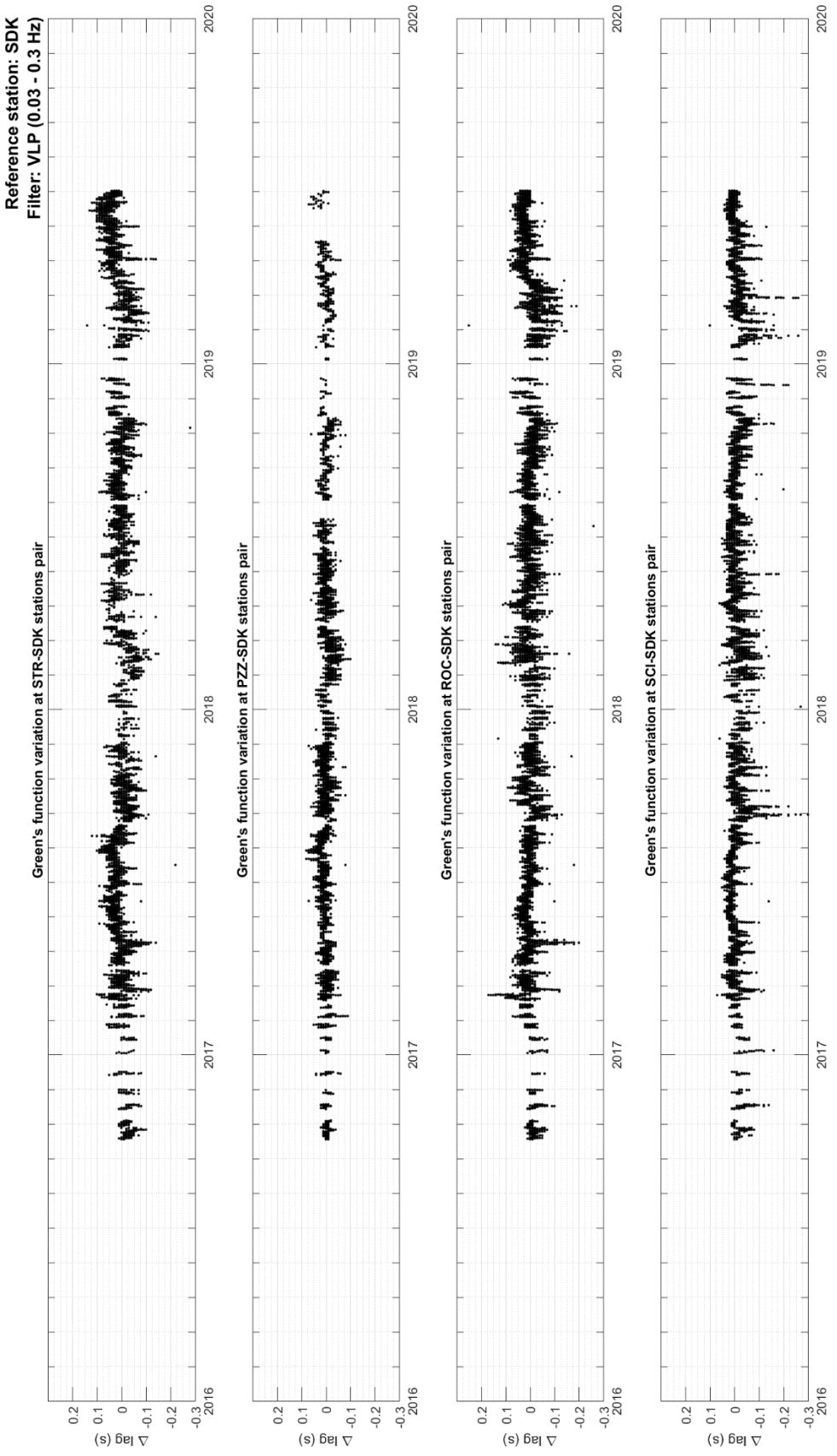

Figure 38. Green's functions variations filtered in low frequency band (0.03 - 0.3 Hz) at stations pairs a) STR-SDK, b) PZZ-SDK, c) ROC-SDK, d) SCI-SDK over a time period of 4 years (2016-01-01 - 2019-31-12). Reference station is SDK.

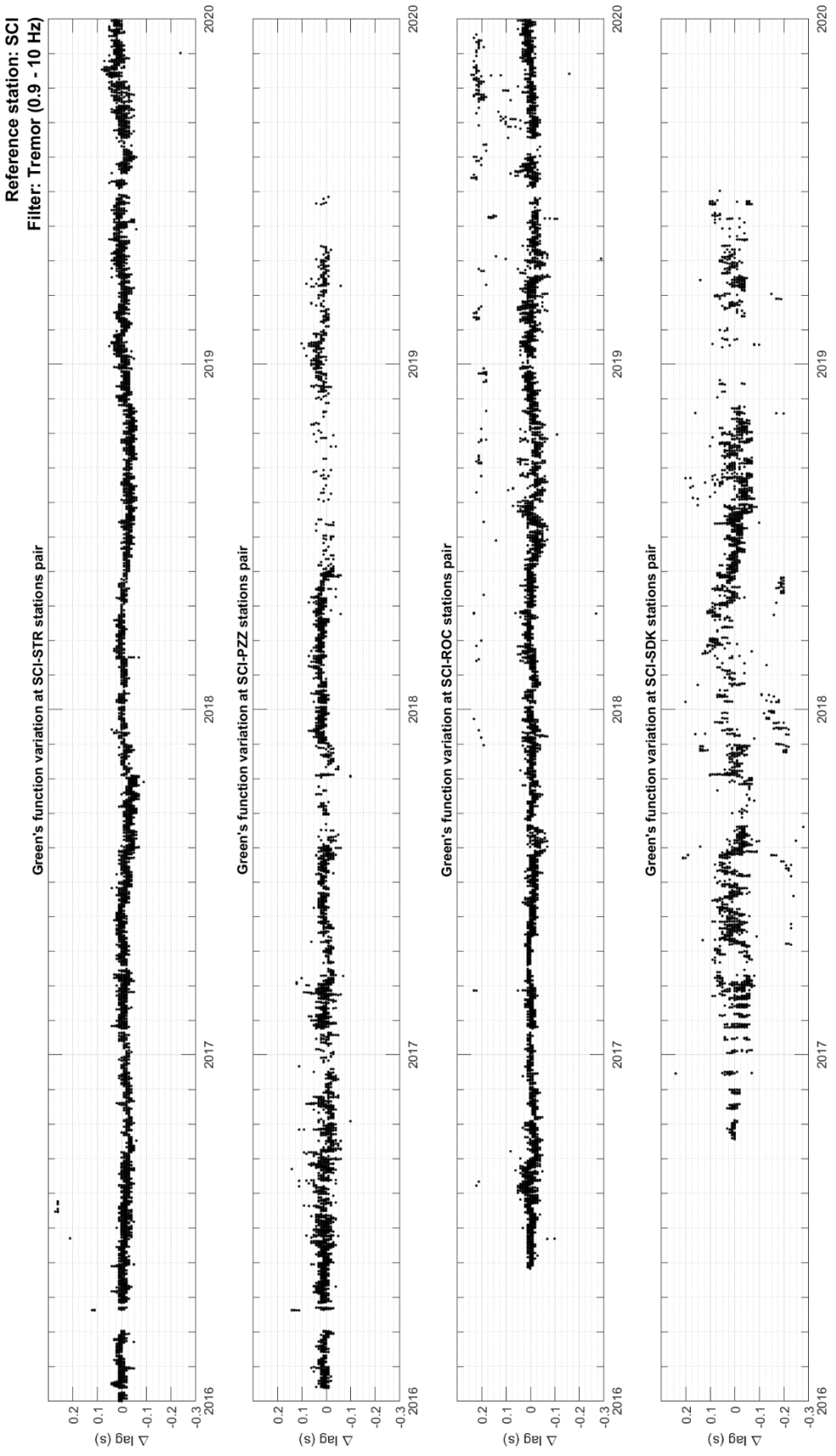

Figure 39. Green's functions variations filtered in high frequency band (0.9 - 10 Hz) at stations pairs a) SCI-STR, b) SCI-PZZ, c) SCI-ROC, d) SCI-SDK over a time period of 4 years (2016-01-01 - 2019-31-12). Reference station is SCI.

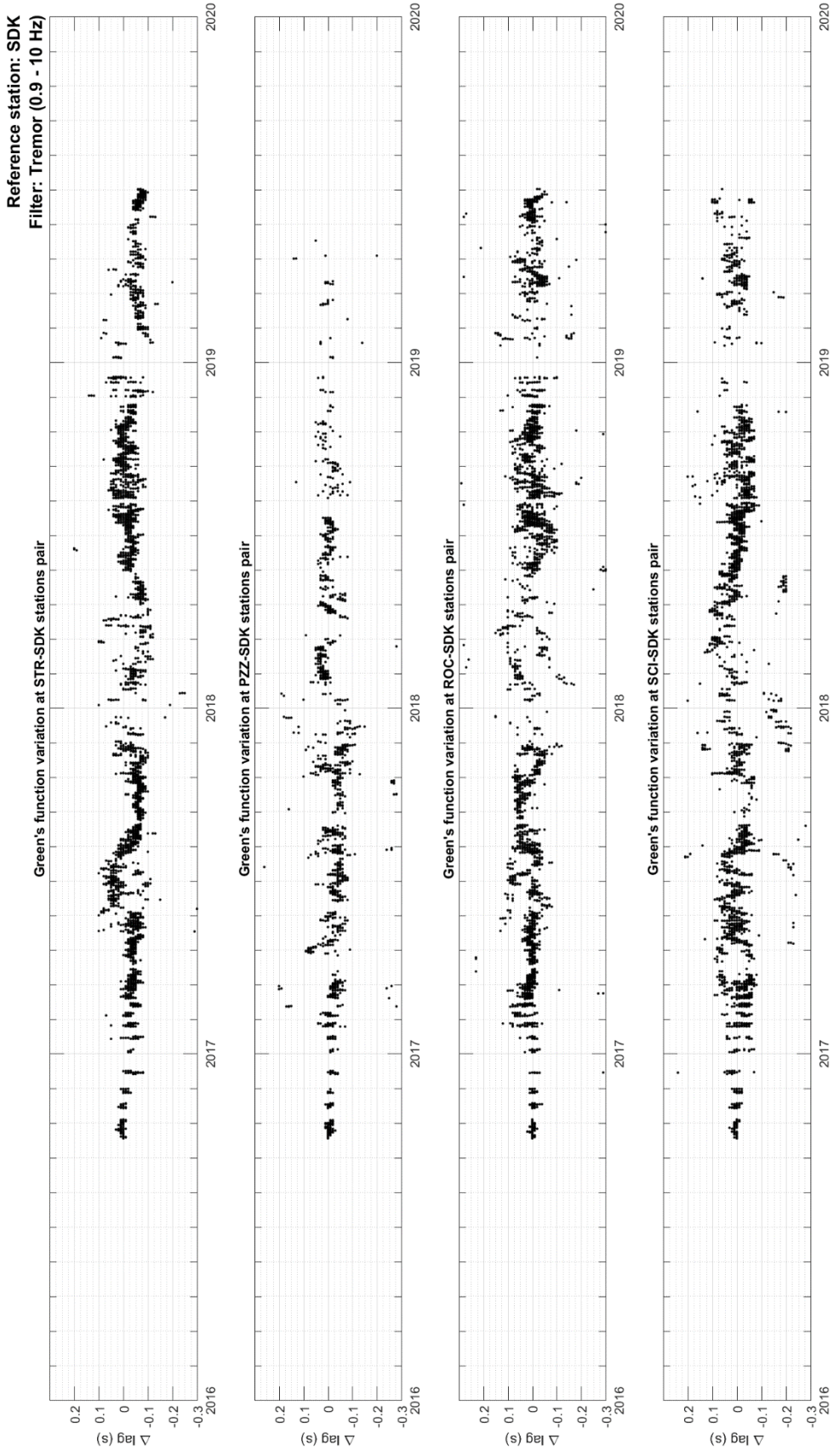

Figure 40. Green's functions variations filtered in high frequency band (0.9 - 10 Hz) at stations pairs a) STR-SDK, b) PZZ-SDK, c) ROC-SDK, d) SCI-SDK over a time period of 4 years (2016-01-01 - 2019-31-12). Reference station is SDK.

The delay times resulting from the proposed interferometric analysis, once applied to the low frequency band (0.03-0.3 Hz) (Figures 33, 34) is showing long term fluctuations for both reference stations. In order to highlight and further investigate this aspect, results have been smoothed over 2400 samples, which corresponds roughly to 100 days, considering one data point every hour resulting from the interferometric analysis (Figure 41).

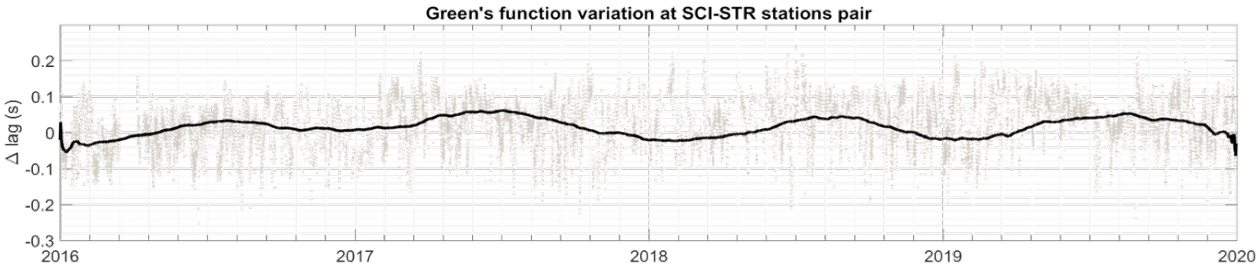

Figure 41. Smoothed time series of Green's function variations filtered in low frequency band. Gray dots shows hourly Green's function variations.

Figure 41 shows that delay times is actually experiencing a very low frequency oscillation, occurring with a seasonal pattern, with increased time delays (up to 0.05 s) recorded typically in the summer period, and reduced time delays (down to -0.02 s) recorded typically in the winter times. Such a seasonal variation appears to match quite nicely the trend of external atmospheric temperature (Figure 42).

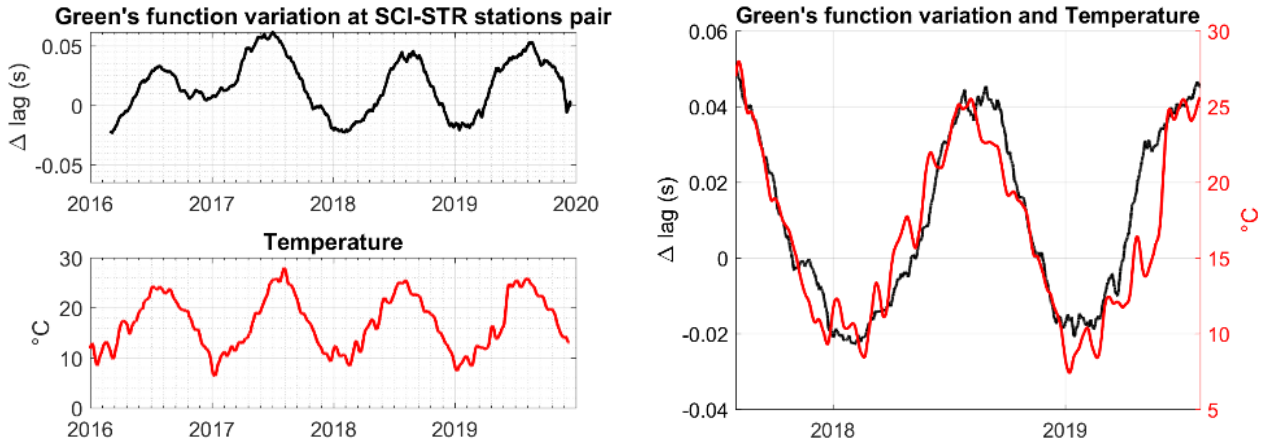

Figure 42. Comparison between Green's function variations filtered in low frequency band (black) and atmospheric temperature (red). Temperature data were recorded in Catania–Fontanarossa Airport.

In order to explain the match between interferometry and temperature (Figure 42), I propose two main hypotheses: the influence of temperature on instrumentation sensors, and the effect of temperature on the propagation medium. I excluded the first hypothesis considering that the two

stations are too close to be affected by a differential temperature effect. In any case, even if was present, influence of temperature over sensors should affect all the sensors in the same way, being not visible indeed in deconvolution results. I therefore favour the second hypothesis. Similar results have already been reported in previous studies (Richter, et al., 2014), and were explained as resulting from partial changes in seismic velocity induced by the ambient temperature affecting the shallowest ground layers.

In any case the strong correlation between interferometry and ambient temperature is a strong evidence of the high sensitivity and reliability of the developed technique.

In order to compare this dataset with additional data sets representative of the volcanic activity, I provide to remove the atmospheric temperature effect.

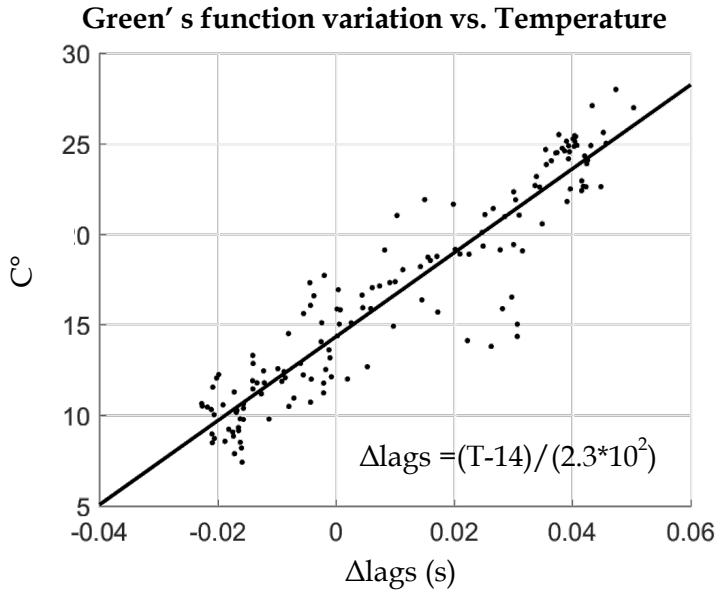

Figure 43. Linear relationship between atmospheric temperature and Green's function variation.

Therefore I interpolated data of the Green's function variation and temperature data (Figure 43) to derive the following equation

$$\Delta lags = \frac{(\mathrm{T} - 14)}{2.3 * 10^2} \qquad \text{Eq. 5.1}$$

where T is the atmospheric temperature in Celsius degrees.

I calculated delta-lags due to temperature from the temperature itself with the derived formula, and removed them from preliminary results (Figure 44).

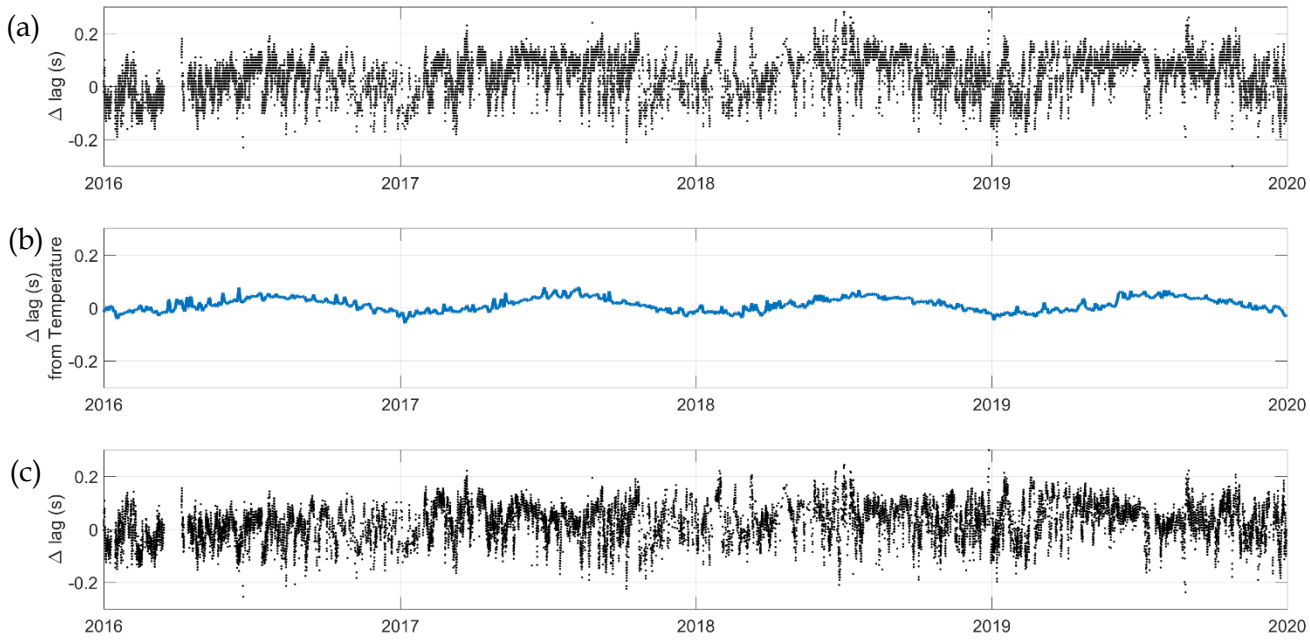

Figure 44. Green's function variation filtered in low frequency band before (a) and after (c) correction by factor (b) due to atmospheric temperature effect on the shallower ground layers.

Afterwards this data set can be compared with additional data sets representative of the volcanic activity.

In Figure 45 I compare delay times obtained from the proposed seismic interferometry analysis, with the take-off angle (dip) of the polarization ellipsoid of the VLP seismic displacement. This angle can be considered as being representative of the depth of the source process of the VLP seismic signal, once applied to compressional "p" waves. Both datasets (interferometry and dip) are smoothed to highlight similarities over the long period (Figure 45).

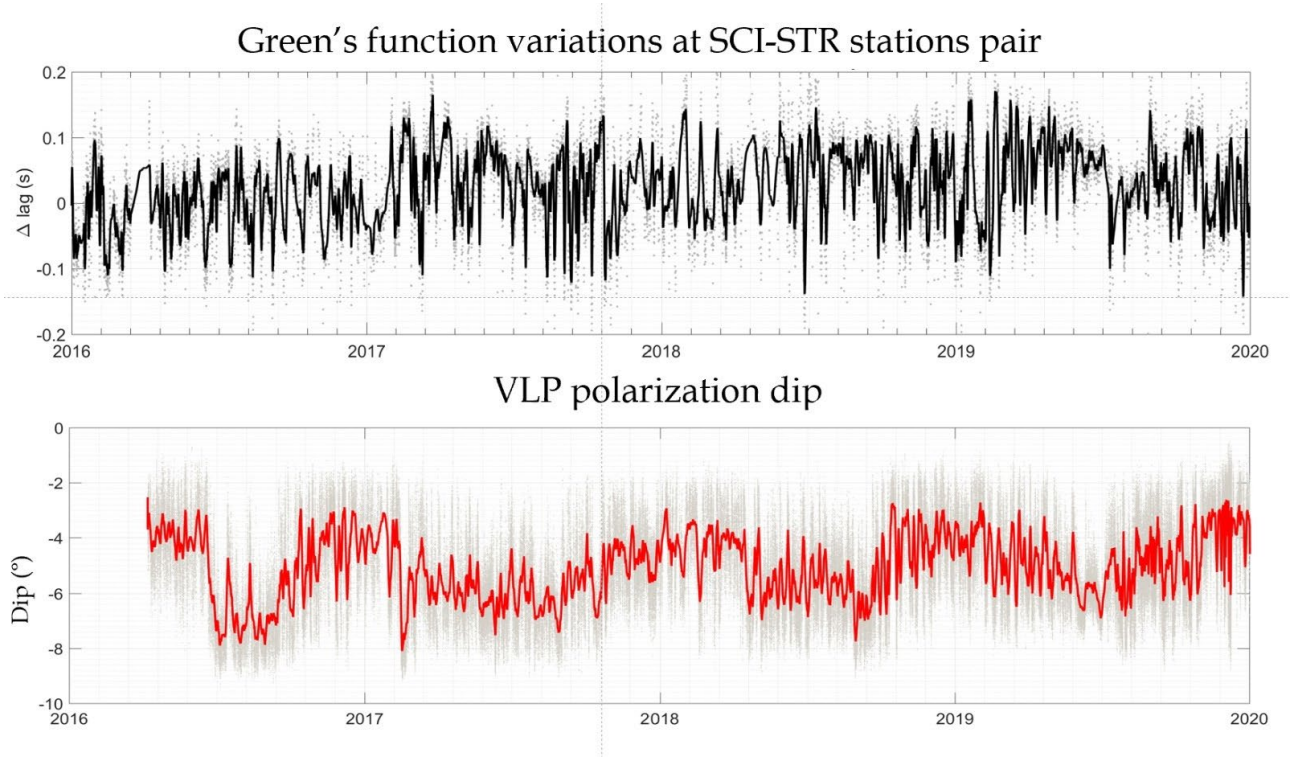

Figure 45. Comparison between Green's function variations at SCI-STR stations pair (black line) and VLP seismic signal polarization dip (red line).

I found that interferometry shows a good anti-correlation with changes in the dip of the polarization ellipsoid of the VLP seismic displacement, revealing a strong link to changes in relative position of the seismic VLP source over time.

In order to test the relationship between delay times derived from interferometry and relative source position, and hence relative onset time at different seismic stations, I realized a synthetic test. Here two seismic time series have been created as responding to recurrent seismic sources, recorded as Gaussian waveforms and repeating in time with variable source position. This is modelled considering the signal recorded at the reference station A (blue in Figure 46 a) that is progressively delayed in time at station B (red in Figure 46 a). This might reflect a source that is getting closer to station A or further away from station B through time. Once the interferometric analysis is applied to the two datasets, delay times (Δlags) is observed to increase progressively with time (Figure 46 b). This is showing how a variation in the source position will affect the resulting delay time.

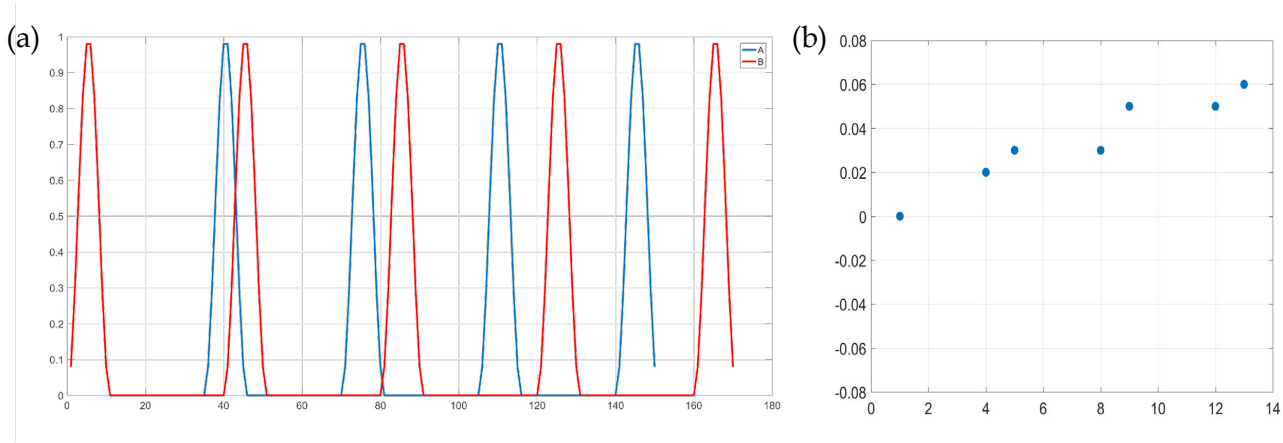

Figure 46. Synthetic test showing increasing Δlags in Green's function variation (b) linked to increasing delay in arrival times (a) of an impulsive function at a receiver B (red line) respect a reference station A (blue line).

Considering SCI as the reference station and STR as the station of analysis, I can image the variation of the source depth of VLP seismic signal, STR and SCI stations being located on the same flank of the volcano at different elevations. Following the synthetic test presented in Figure 42, an increase in the delay time resulting from the interferometric analysis is consistent with a deeper VLP source, as confirmed by dip of the polarization ellipsoid calculated from the VLP seismic displacement (Figure 47).

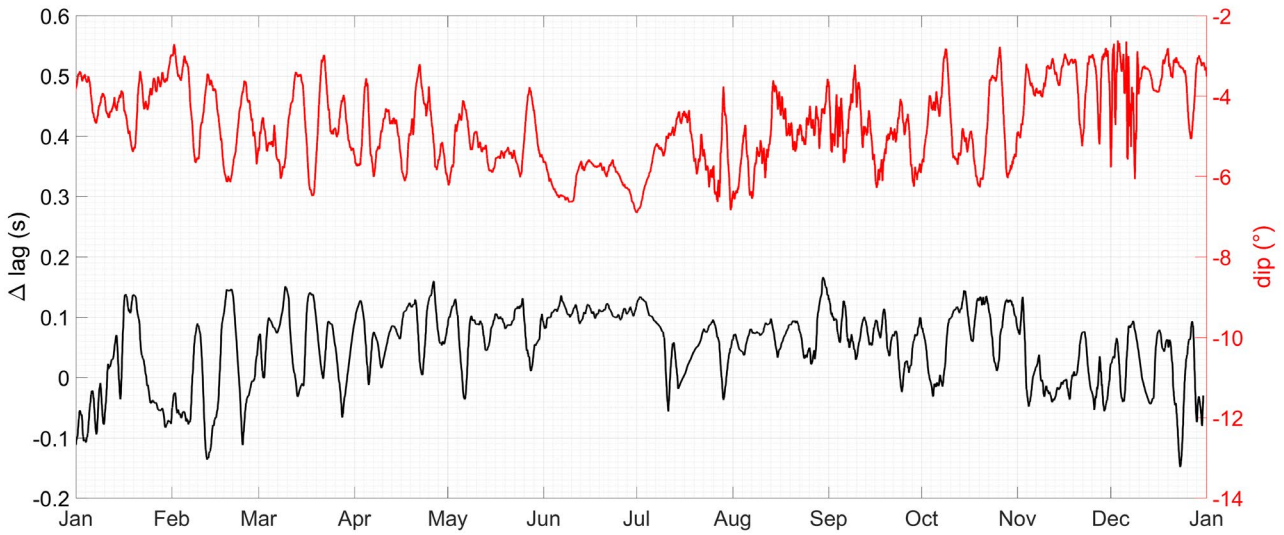

Figure 47. Correlation between Green's function variation (black line) and VLP polarization dip (red line).

Unlike for the low frequency (0.003-0.3 Hz) band of analysis, where interferometry might reflect changes in the source position, no clear evidence of substantial variations in all analysed time period have been found in high frequency band analysis (Figure 48), except for the long term seasonal variation due to atmospheric temperature effect already described (Figure 41).

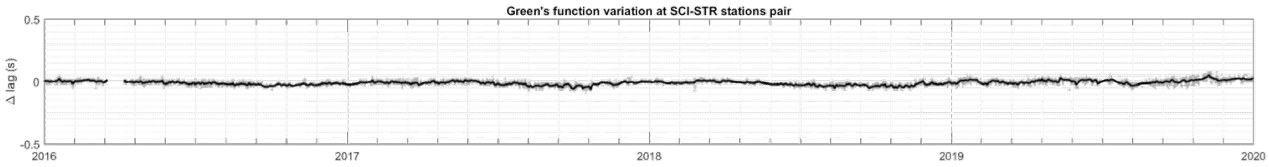

Figure 48. Green's function variation filtered in high frequency band without temperature effect.

From Figure 48, I conclude that interferometry, once applied to the high frequency band, is not highlighting any changes of the seismic source.

However, I cannot exclude that any variation might be possible. Indeed, the efficiency of the proposed interferometry depends on network geometry and dimension, as well as on the characteristics of the source. In this case the seismic network might be too small and too close to the summit region, or the source of tremor might possibly be an extended source acting all along the magmatic column rather than as a point source. Therefore, further analysis will be required to better constrain the use of interferometry for tremor.

In any case I conclude that interferometry in low frequency band (i.e., VLP frequency band) on Stromboli volcano is a fast, reliable and sensitive method to track VLP source position changes, whilst no significative results can be retrieved from the high frequency filter (tremor frequency band) data analysis.

5.2. VOLCANIC TREMOR

Although seismic interferometry shows no results in the tremor frequency band, a careful analysis of the tremor dataset of the year 2019 reveals a change in the tremor behaviour 14 days before the 03 July 2019 paroxysm.

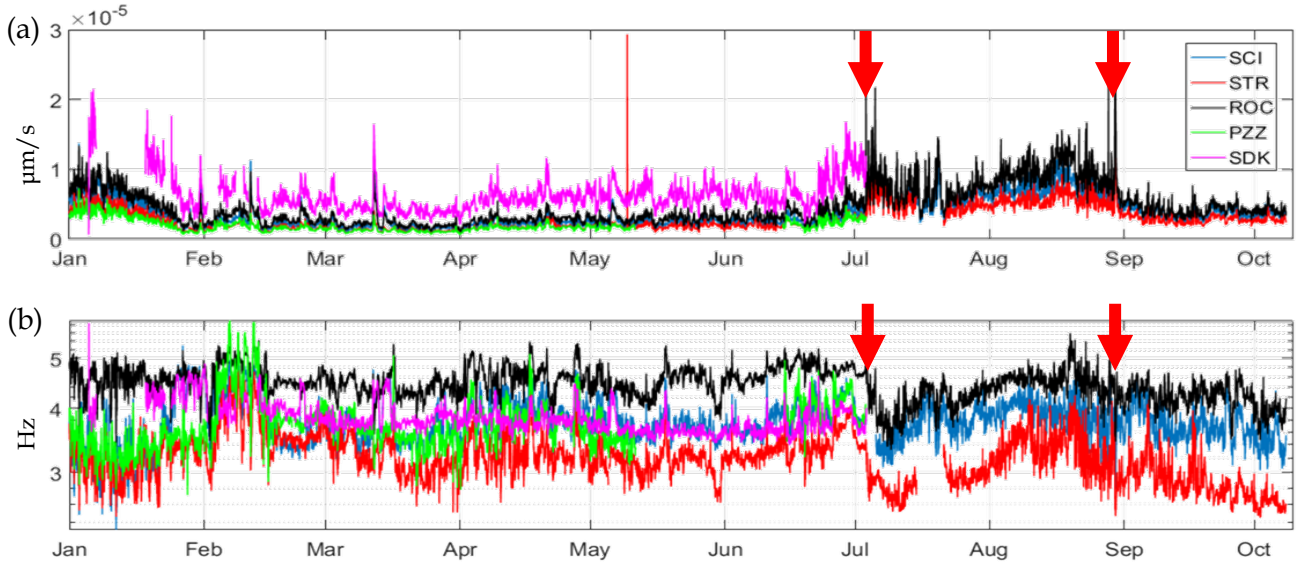

Figure 49. Tremor amplitude (a) and frequencies (b) between January the 1st 2019 and October the 4th 2019. Red arrows indicate the two paroxysmal explosions occurred on July the 3rd and August the 28th. Notice that changes in frequency content happen only after the first paroxysmal explosion. Before the explosive event only large oscillation in tremor amplitude may be considered a notable variation.

On July 3rd and August 28th 2019 two paroxysmal events occurred in Stromboli volcano. The July 3rd event, occurred abruptly, without showing any evident changes in the standard monitored parameters like infrasonic pressure of explosions, rate of VLP seismic signals, thermal activity evaluated by thermal cameras and SO_2 flux. All those information were kindly provided by Laboratorio di Geofisica Sperimentale (L.G.S) on Florence University.

Tremor data analysis carried out with interferometric techniques showed no significant variations (Figure 48), as discussed above. However, I tried to extract more information about volcano dynamic processes, by considering seismic tremor data both in terms of amplitude and fundamental frequency content (Figure 49). The frequency analysis of volcanic tremor performed by zero-crossing technique (see section 4.2.2) shows indeed a sudden variation after the July 3rd paroxysmal explosion with a shift towards a lower fundamental frequency content. This shift persisted for several weeks and required almost 40 days before getting back to previous values (Figure 49 b). A similar shift is not clear after the August 28th paroxysm, and in both cases, no clear variations seem to occur before the explosive event.

Several source mechanisms of volcanic tremor have been proposed in the literature (refer to Konstantinou, 2003 for a review) both related to magma migration within the conduits or two-phase

flow dynamic of gas rising in the magma (for a brief description of volcanic tremor source models see section 2.4.2).

Regarding the volcanic tremor models related to the resonance of fluid-filled cracks and conduits (Chouet, et al., 1997), a decrease of the frequency content of recorded tremor is expected for an increase of the conduit length or for an increase of the gas content in the magma that causes a decrease of the propagation velocity. SO_2 flux analysis suggests an increase in the gas content in the magma column after the July 3rd paroxysm. However, the observed SO_2 increase is delayed from the decrease of the frequency content of volcanic tremor, suggesting that the two parameters are likely decoupled.

Observations at Stromboli volcano showed that volcanic tremor is linked to the intermittent busting of gas pockets, repeating almost every 1 second, at the magma free surface, radiating small amplitude infrasonic transients called puffing. Therefore, among the other possible source mechanism of volcanic tremor, I consider (*i*) the viscoelastic reaction of the magma to pressure drops induced by gas bubble growth rate under constant depressurization (Ripepe & Gordeev, 1999) and (*ii*) the variable degassing rate cycling between vigorous and weak degassing phases (Ripepe, et al., 2002); (Kondo, et al., 2019).

Tremor spectra is considered to be determined by viscoelastic characteristics of the magma to pressure drops related to the coalescence and growth of gas pockets (Ripepe & Gordeev, 1999). Here the spectral content of the recorded volcanic tremor is controlled by the duration of the pressure drop that represents the viscoelastic relaxation time of the magma and the gas bubble growth rate. Therefore, changes of tremor frequency are related to changes of the viscosity of the magma, with lower relaxation time for lower magma viscosity. However, viscosity changes in the magma at Stromboli volcano immediately after the paroxysm and related to gas depletion in the shallow feeding system, if present, would be too small to explain a significant variation of the relaxation time and hence of the tremor frequency. Indeed, I believe that the observed frequency decrease immediately after the July 3rd paroxysm, is most likely related to changes of the gas emission dynamics.

Changes in the gas dynamics is considered by analysing the way infrasound pressure transients related to puffing activity are behaving before (15th June 2019) and after (15th July 2019) the July 3rd paroxysms that marked a decrease of the tremor frequency.

Before the paroxysm, when tremor was characterized by a higher frequency content, infrasonic pulses were repeating at a rate of ~ 1 event every second and had a duration of ~0.5 sec. After the paroxysm infrasonic pulses related to puffing activity were recorded at a lower rate of ~ 1.5 seconds and pulses had a longer duration of ~ 0.7 sec (Figure 50 and Figure 51). Such a variation of the duration of pressure pulses is matching the change of frequency of seismic signals.

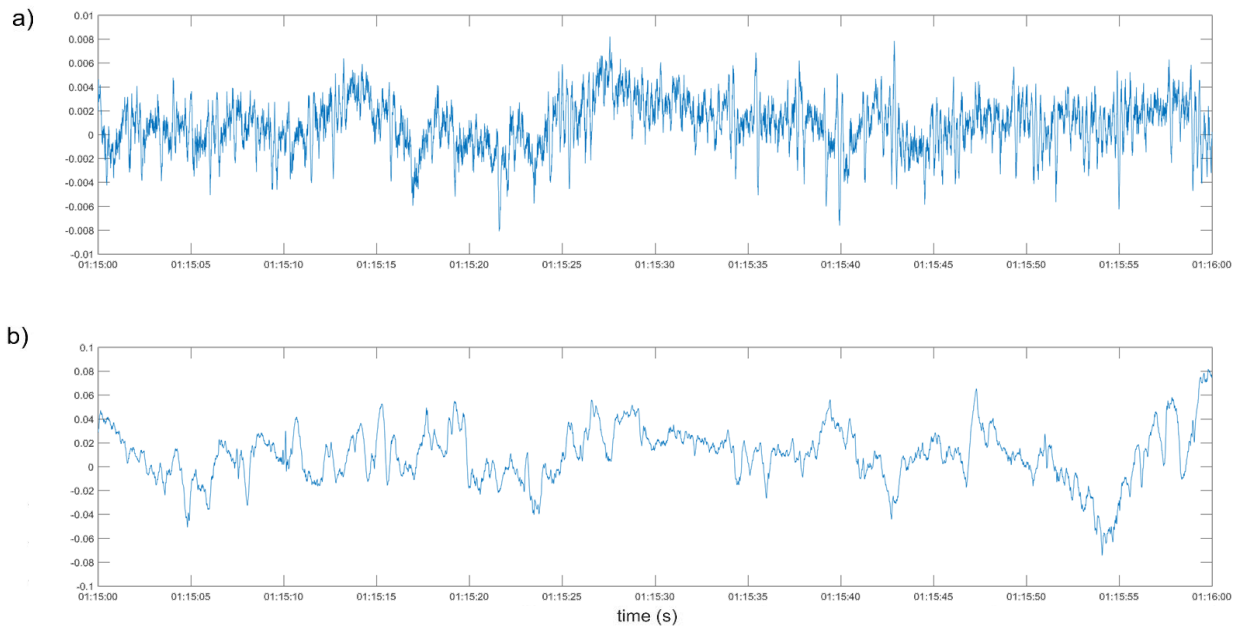

Figure 50. 15 minutes raw data time series of infrasonic pressure on (a) 15th June 2019 and (b) 15th July 2019. Frequency and duration of infrasonic pressure transients of puffing pulse show clear differences.

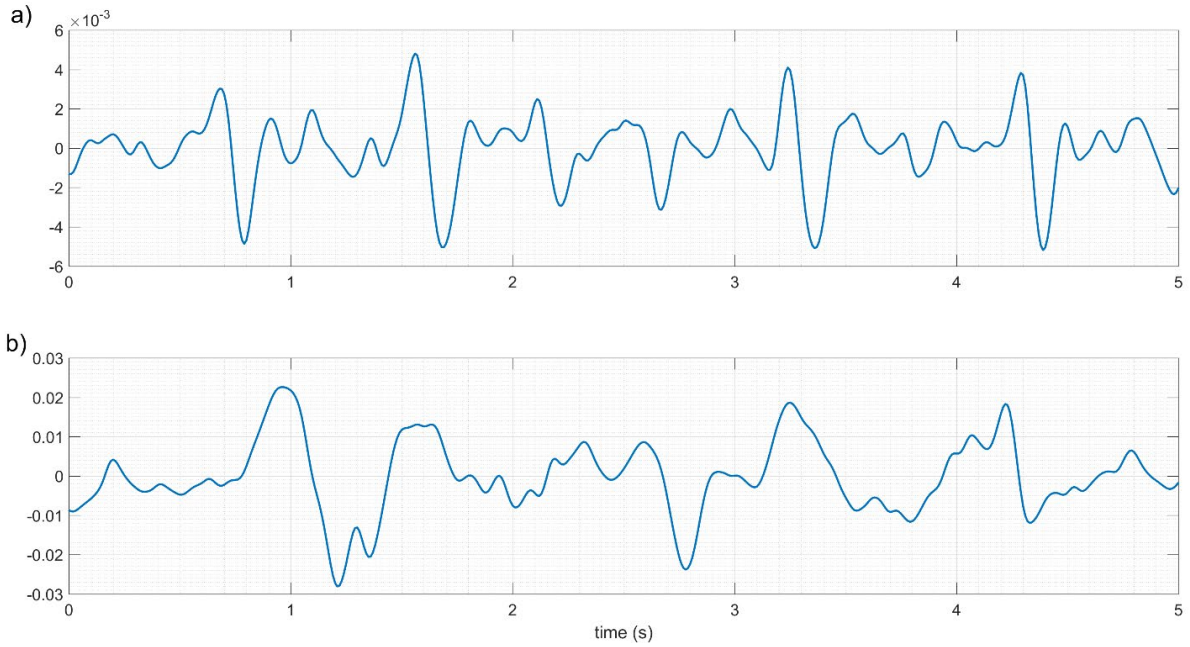

Figure 51. 5 seconds raw data time series of infrasonic pressure showing differences in frequency and duration of infrasonic pressure transient related to puffing pulse on (a) 15th June 2019 and (b) 15th July 2019.

Seismic, infrasound and thermal analysis of degassing and explosive activity at Stromboli volcano (Ripepe, et al., 2002) showed that puffing is somehow related to magma level within the conduit. Enhanced magma supply is driving both an increase in the free surface level within the conduit and a high degassing rate. During this phase, the period between consecutive gas enriched magma layers is short (about 1.5 – 2 seconds) resulting in higher tremor amplitude and explosion frequency. Similarly, periods of reduced magma supply results in lower level of the magma surface that is

marked by gas enriched magma layers more spaced in time (about 3 – 4 seconds), resulting in a lower rate of explosion and lower tremor frequency (Figure 52).

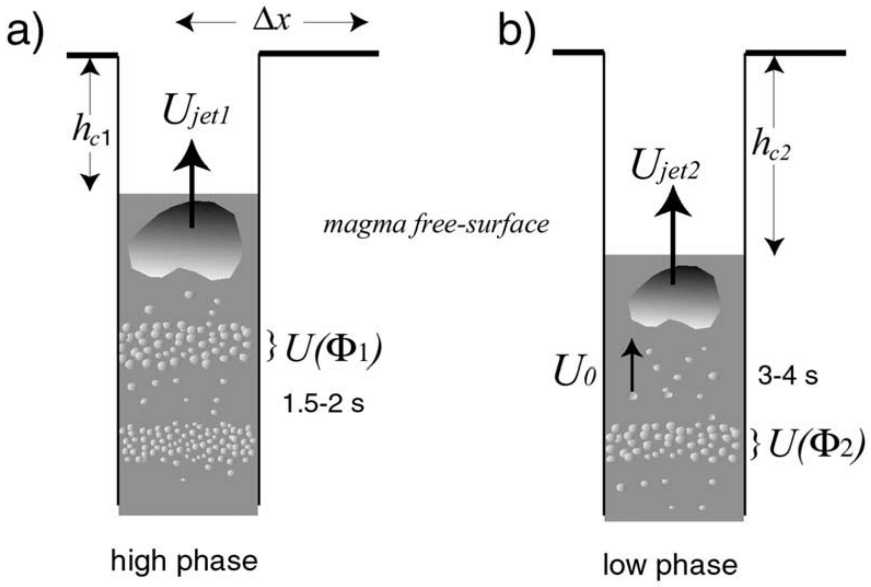

Figure 52. Sketch of the degassing models during (a) high degassing phase and (b) low degassing phase. Positions of the magma free surface are indicated by hc1 and hc2, Δx is the distance of the sensors from the vent, Ujet1 and Ujet2 are the gas jet velocities. High and low degassing phases are characterized by a different gas bubble concentration (φ) which controls the bubble layer velocity U(φ). U_0 represents the velocity of a single bubble, where U_0>U(φ). From Ripepe, et al., 2002.

According to this model, the reduced frequency content of volcanic tremor should have been related to a lower magma level within the conduits and a lower explosion rate. Such a scenario is in good agreement with a decrease of magma column inside the conduit revealed by the deepening of VLP source position and a general deflation of volcanic edifice. However, the observed activity after the July 3rd paroxysm, marked by a high rate of explosive events, seems to be at odds whit such a model. Whichever model I choose, it does not seem able to take into account all available data features and their mutual evolutions at the same time. Therefore, the origin of the frequency shift of the volcanic tremor remains still a debated question.

Looking at tremor amplitude, calculated by root mean square (see section 4.2.1), I notice a small amplitude increase that is punctuated by sudden and frequent phases of amplitude increase occurring almost every 2 hours during the 14 days before the July 3rd paroxysm. I refer to "spasmodic tremor" (Figure 49 a, Figure 53) for such an anomalous behaviour.

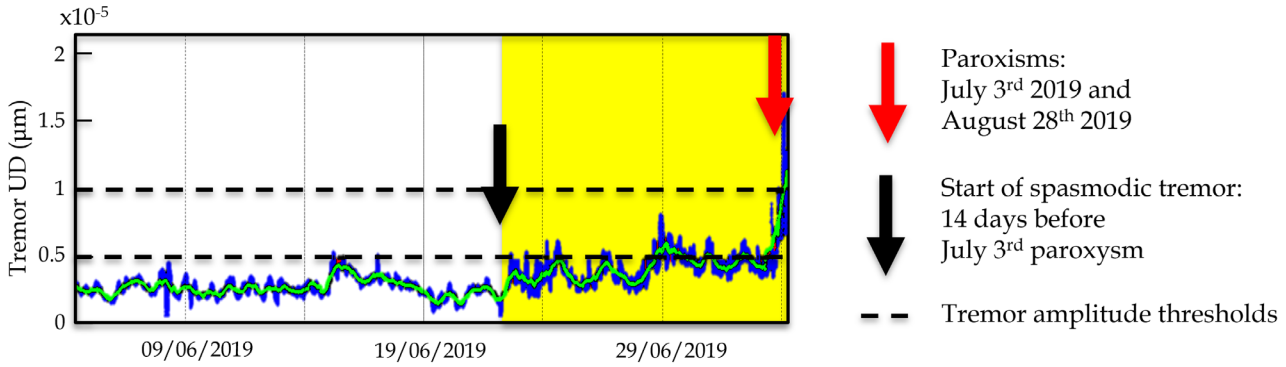

Figure 53. Tremor amplitude (RMSA) between June 4th and July 4th 2019. Blue line shows hourly amplitude variations. Green line shows 12 hours amplitude variation. Spasmodic behaviour of tremor amplitude starts 14 days before the paroxysmal event of July 3rd 2019.

The variations discussed above, despite being atypical for Stromboli volcano, are difficult to be identified from raw data and standard analysis. Therefore, in order to consider simultaneously amplitude and frequency of volcanic tremor, I performed a frequency analysis on the RMS amplitude variation of seismic tremor using again the zero-crossing technique. In this case the input dataset is tremor amplitude so that the elaboration provides the frequency of amplitude fluctuations. Results show sudden and clear increase close to phases of intense activity related to major gas release. In particular this increase seems to precede about 10 days the two paroxysms of July and August (Figure 54).

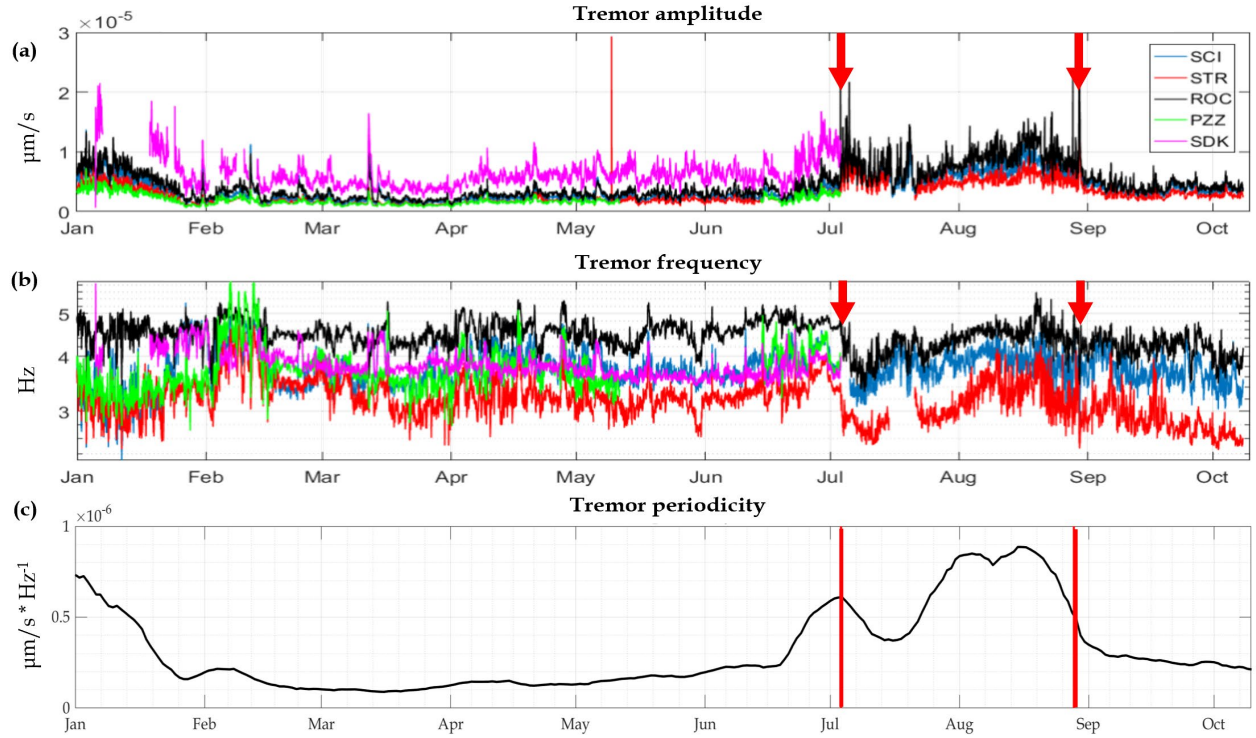

Figure 54. Analysis of frequency of amplitude increasing (c) compared with tremor amplitude (a) and tremor fundamental frequency (b). Red arrows in plot (a) and (b) and red vertical bar in plot (c) indicate paroxysmal explosion. Analysis shows sudden and clear increase close to phases of intense activity related to a major gas release during paroxysmal explosion of July the 3rd and August the 28th, 2019.

I extended the analysis to the 4 years long dataset (Figure 55). Throughout the entire dataset the tremor periodicity reaches high values before paroxysms and increases during period punctuated by major explosions.

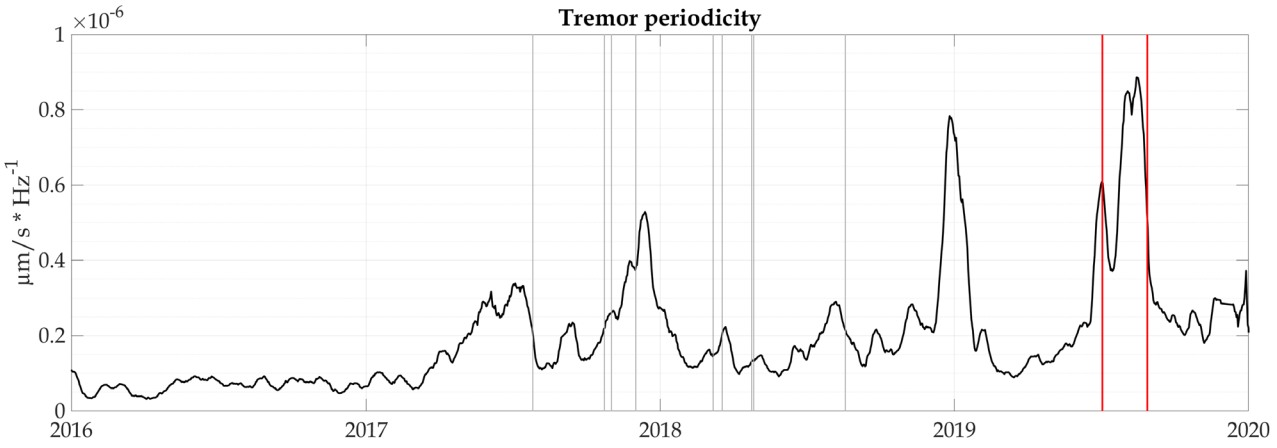

Figure 55. Long-term analysis of Tremor periodicity. Thick red vertical bars indicate paroxysmal explosions. Thin grey vertical bars indicate major explosions.

As already discussed by other authors, spasmodic tremor, with large amplitude fluctuations is likely produced as a consequence of increased magma flow (Konstantinou & Schlindwein, 2003).

(Kondo, et al., 2019) show that small transient pulses were evident in the seismic records in the period preceding an effusive eruption associated with an increase in ground deformation. They suggest an increase in gas flux leading to a progressive pressurization of the magma column before the explosion. After the occurrence of the explosion the seismic pattern repeated in cycles of variable durations during which only small puffing occurs. These seismicity cycles are also in agreement with gas flux measurements recorded using UV camera imaging.

Referring to the effusive eruption which started on 7 August 2014, they show that characteristic cycle in the seismic signal was observed only in the period preceding the effusive eruption. The signal disappeared after the transition from the summit activity to the flank eruption. They suggest that seismicity cycles represent cyclic changes of the gas flux regime in the shallow magma column, associated with increases in the magma-gas supply input rate before the effusive eruption.

I consider that this kind of behaviour also occurred during the 2019 paroxysmal explosions and during phases of intense explosive activity in the winter of 2017-2018.

Those evidences suggest that this method seems to be a promising technique to track changes in the magmatic input rate coming from deep portions of the volcanic conduit.

6. CONCLUSIONS

In this study I developed a seismic interferometric analysis based on deconvolution. The proposed procedure appears to be much more efficient and stable than the standard interferometric approaches based on cross-correlation analysis, both in terms of noise level and computing time.

The analysis was applied to data recorded by the local seismic network of L.G.S. deployed on Stromboli volcano for a period of 4 years, spanning from January 2016 to December 2019, looking for variations in the source mechanisms of seismic energy or variations within the propagation medium. The analysis was applied to two frequency bands, which are best representative of volcanic tremor and VLP seismic transients, that represent the main features of seismic signals at Stromboli.

Delay times obtained by interferometry show a seasonal variation strongly correlated with external atmospheric temperature, suggesting an effect of temperature on the shallowest ground layers and revealing the high sensibility and reliability of the developed technique. The maximum effect of the temperature on the lag (0.07 s) is however limited compared to real observed variations and was successfully removed.

The proposed interferometric analysis, once applied to the low frequency band (0.03 – 0.3 Hz), shows a very good correlation with the relative position of the seismic VLP, thus suggesting that it might be used efficiently for relative source positioning. However, no clear evidence of significative variations is obtained from interferometric analysis applied to the high frequency (1 - 10 Hz) band for all analysed time period.

Nevertheless, I cannot exclude variations of the source characteristics of volcanic tremor. The frequency analysis, performed by the zero-crossing technique, on amplitude changes of volcanic tremor shows indeed a clear increase before paroxysmal events, likely reflecting an increased magma and/or gas flux. This analysis, fast and easy to be performed, showed to be a promising technique to track changes in the magmatic input rate from the deep portions of the volcanic conduit, and could be used efficiently as a precursor at Stromboli or other open-conduit systems elsewhere in the world where tremor variations are limited.

7. REFERENCES

Aki, K., 1957. Space and time spectra of stationary stochastic waves, with special reference to micro-tremors. *Bulletin of the Earthquake Research Institute,* Issue 35, pp. 415-457.

Aki, K., 1969. Analysis of seismic coda of local earthquake as scattered waves.. *Journal of Geophysical Research,* 80(23), pp. 615-631.

Aki, K., 1985. Theory of earthquake prediction with special reference to. *Earthquake Prediction Res.,* Volume 3, pp. 219-230.

Aki, K. & Chouet, B., 1975. Origin of coda waves: Source, attenuation and scattering effects.. *Journal of Geophysical Research,* 80(23), pp. 3322-3342.

Aki, K., Fehler, M. & Das, S., 1977. Source mechanism of volcanic tremor: fluid-driven crack models and their application to the 1963 kilauea eruption. *Journal of Volcanology and Geothermal Research,* 2(3), pp. 259-287.

Allard, P. et al., 1994. Sulphur output and magma degassing budget of Stromboli volcano. *Nature,* 368(6469), pp. 326-330.

Andronico, D., Corsaro, R., Cristaldi, A. & Polacci, M., 2008. Characterizing high energy explosive eruptions at Stromboli volcano using multidisciplinary data: An example from the 9 January 2005 explosion. *Journal of Volcanology and Geothermal Research,* 176(4), pp. 541-550.

Aster, R. et al., 2003. Very long period oscillations of Mount Erebus Volcano. *Journal of Geophysical Research: Solid Earth,* 108(B11).

Bakulin, A. & Calvert, R., 2004. Virtual source: new method for imaging and 4D below complex overburden. *SEG Expanded Abstracts,* Issue 23, pp. 112-115.

Bakulin, A. & Calvert, R., 2006. The virtual source method: Theory and case study. *Geophysics,* 71(4), pp. SI139-SI150.

Barberi, F., Rosi, M. & Sodi, A., 1993. Volcanic hazard assessment at Stromboli based on review of historical data. *Acta vulcanologica,* Volume 3, pp. 173-187.

Bensen, G. et al., 2007. Processing seismic ambient noise data to obtain reliable broad-band surface wave dispersion measurements. *Geophysical Journal International,* 169(3), pp. 1239-1260.

Berg, E. & Janessen, T., 1960. Microséismes et séismes précédant l'éruption du Nyanmragira-Kitsimbanyi (Afrique Centrale) 1958. *Bulletin of Volcanology,* Volume 23, pp. 63-68.

Bertagnini, A., Métrich, N., Landi, P. & Rosi, M., 2003. Stromboli volcano (Aeolian Archipelago, Italy): An open window on the deep-feeding system of a steady state basaltic volcano. *Journal of Geophysical Research: Solid Earth,* 108(B7\).

Blackburn, E. A., Wilson, L. & Sparks, R. S. J., 1976. Mechanism and dynamics of Strombolian activity. *Journal of the Geological Society,* Volume 132, pp. 429-440.

Brenguier, F. et al., 2008. Postseismic relaxation along the San Andreas fault at Parkfield from continuous seismological observations. *Science,* 321(5895), pp. 1478-1481.

Campillo, M. & Paul, A., 2003. Long-range correlations in the diffuse seismic coda. *Science,* 299(5606), pp. 547-549.

Chouet, B. et al., 2013. Upper Conduit Structure and Explosion Dynamics at Stromboli. In: *The Stromboli Volcano: An Integrated Study of the 2002–2003 Eruption.* s.l.:American Geophysical Union (AGU), pp. 81-92.

Chouet, B. et al., 2003. Source mechanisms of explosions at Stromboli Volcano, Italy, determined from moment-tensor inversions of very-long-period data. *Journal of Geophysical Research: Solid Earth,* 108(81), pp. ESE 7-1-ESE 7-25.

Chouet, B. et al., 1999. Broadband measurements of the sources of explosions at Stromboli Volcano, Italy. *Geophysical Research Letters,* 26(13), pp. 1937-1940.

Chouet, B. et al., 1997. Source and path effects in the wave fields of tremor and explosions at Stromboli Volcano, Italy. *Journal of Geophysical Research: Solid Earth,* 102(B7), pp. 15129-15150}.

Claerbout, J. F., 1968. Synthesis of a layered medium from its acoustic transmission response. *Geophysics,* Issue 33, pp. 264-269.

Cole, P., Neri, A. & Baxter, P., 2015. Hazards from Pyroclastic Density Currents. In: *The Encyclopedia of Volcanoes.* s.l.:s.n., pp. 943 - 956.

Corazzato, C. et al., 2008. What controls sheet intrusion in volcanoes? Structure and petrology of the Stromboli sheet complex, Italy. *Journal of Volcanology and Geothermal Research,* Volume 173, pp. 26-54.

Curtis, A. et al., 2006. Seismic interferometry - turning noise into signal. *The Leading Edge,* Volume 25, pp. 1082-1092.

De Astis, G., Ventura, G. & Vilardo, G., 2003. Geodynamic significance of the Aeolian volcanism (Southern Tyrrhenian Sea, Italy) in light of structural, seismological, and geochemical data. *Tectonics,* 22(40).

Delle Donne, D. et al., 2006. Monitoring Explosive Volcanic Activity Using Thermal Images, Stromboli Volcano, Italy. *AGU Fall Meeting Abstracts,* Volume 79, p. 1795.

Delle Donne, D. & Ripepe, M., 2012. High-Frame Rate Thermal Imagery of Strombolian Explosions: Implications for Explosive and Infrasonic Source Dynamics. *Journal of Geophysical Research (Solid Earth),* Volume 117, pp. 9206-.

Derode, A., Larose, E., Campillo, M. & Fink, M., 2003. How to estimate the Green's function of a heterogeneous medium between two passive sensors? Application to acoustic waves. *Applied Physics Letters,* 83(15), pp. 3054-3056.

Dibble, R. R., 1969. Seismic power recordings during hydrothermal erupions from Ruapehu crater lake in Aprii 1968. *Journal of Geophysical Research,* 74(27), p. 6545–6551.

Douze, E. J. & Sorrells, G. G., 1972. Geothermal ground-noise surveys. *Geophysics,* 37(5), pp. 813-824.

Dpuze, E. Y. & Sorrells, G. G., 1972. Geothermal ground noise surveys. *Geophysics,* 37(5), pp. 813-824.

Draganov, D. et al., 2009. Reflection images from ambient seismic noise. *Geophysics,* 74(5), pp. A63-A67.

Draganov, D. et al., 2007. Retrieval of reflections from seismic background-noise measurements. *Geophysical Research Letters,* 34(4).

Duvall, T. L., Jeffferies, S. M., Harvey, J. W. & Pomerantz, M. A., 1993. Time–distance helioseismology. *Nature,* 362(6419), pp. 430-432.

Eaton, I. P. & Richter, D. H., 1960. The 1959 eruption of Kilauea. *Geotimes,* 4(5), pp. 24-27.

Einarsson, P., 2018. Short-Term Seismic Precursors to Icelandic Eruptions 1973–2014. *Frontiers in Earth Science,* Volume 6, p. 45.

Falsaperla, S., Langer, H. & Spampinato, S., 1998. Statistical analyses and characteristics of volcanic tremor on Stromboli Volcano (Italy). *Bulletin of volcanology,* 60(2), pp. 75-88.

Finch, R. H., 1943. The seismic prelude to the 1942 eruption Mauna Loa. *Bulletin of the Seismological Society of America,* Volume 33, pp. 237-241.

Finch, R. H., 1949. Volcanic tremor. *Bulletin of the Seismological Society of America,* Volume 39, pp. 73-78.

Francalanci, L., 1987. *Evoluzione vulcanologica e magmatologica di Stromboli (Isole Eolie): relazioni fra magmatismo calc-alcalino e shoshonitico.* Firenze: s.n.

Francalanci, L., Manetti, P. & Peccerillo, A., 1989. Volcanological and magmatological evolution of Stromboli volcano (Aeolian Islands): The roles of fractional crystallization, magma mixing, crustal contamination and source heterogeneity. *Bulletin of Volcanology,* 51(5), pp. 355-378.

Francalanci, L., Manetti, P., Peccerillo, A. & Keller, J., 1993. Magmatological evolution of the Stromboli volcano (Aeolian Arc, Italy): inferences from major and trace element and Sr isotopic composition of lavas and pyroclastic rocks. *Acta Vulcanologica,* Volume 3, pp. 127-151.

Francalanci, L., Tommasini, S. & Conticelli, S., 2004. The volcanic activity of Stromboli in the 1906–1998 AD period: mineralogical, geochemical and isotope data relevant to the understanding of the plumbing system. *Journal of Volcanology and Geothermal Research,* 131(1), pp. 179-211.

Francalanci, L., Tommasini, S., Conticelli, S. & Davies, G. R., 1999. Sr isotope evidence for short magma residence time for the 20th century activity at Stromboli volcano, Italy. *Earth and Planetary Science Letters,* 167(1-2), pp. 61-69.

Francis, P., Oppenheimer, C. & Stevenson, D., 1993. Endogenous growth of persistently active volcanoes. *Nature,* 366(6455), pp. 554-557.

Gambino, S. & Scaltrito, A., 2018. Volcanic-tectonic seismicity at Stromboli (2005–2016). *Journal of Volcanology and Geothermal Research,* Volume 350, pp. 1-6.

Genco, R. & Ripepe, M., 2010. Inflation-deflation cycles revealed by tilt and seismic records at Stromboli volcano. *Geophysical Research Letters,* 37(12).

Genco, R. et al., 2014. Acoustic Wavefield and Mach Wave Radiation of Flashing Arcs in Strombolian Explosion Measured by Image Luminance.. *Geophysical Research Letters,* Volume 41.

Gillot, P. Y. & Keller, J., 1993. Age dating of Stromboli. *Acta Vulcanologica,* Volume 3, pp. 69-77.

Goes, S. et al., 2004. A recent tectonic reorganization in the south-central Mediterranean. *Earth and Planetary Science Letters,* 226(3-4), pp. 335-345.

Gorshkov, G. & Dubik, Y., 1970. Gigantic directed blast at Shiveluch volcano (Kamchatka). *Bulletin of Volcanology,* Volume 34, pp. 261-288.

Gorshkov, G. S. & Dubik, Y. M., 1970. Gigantic directed blast at Shiveluch volcano (Kamchatka). *Bulletin Volcanologique,* 34(1), pp. 261-288.

Grêt, A., Snieder, R., Aster, R. C. & .Kyle, P. R., 2005. Monitoring rapid temporal change in a volcano with coda wave interferometry. *Geophysical Research Letters,* 32(6).

Grêt, A., Snieder, R. & Scales, J., 2006. Time-lapse monitoring of rock properties with coda wave interferometry. *Journal of Geophysical Research: Solid Earth,* 111(B3), pp. 0148-0227.

Haney, M. M. et al., 2014. Tracking Changes in Volcanic Systems with Seismic Interferometry. In: M. Beer, I. A. Kougioumtzoglou, E. Patelli & I. S. Au, eds. *Encyclopedia of Earthquake Engineering.* Berlin, Heidelberg: Springer Berlin Heidelberg, pp. 1-23.

Harris, A. J. L. & Stevenson, D. S., 1997. Magma budgets and steady-state activity of Vulcano and Stromboli. *Geophysical Research Letters,* 24(9), pp. 1043-1046.

Hohl, D. & Mateeva, A., 2006. Passive seismic reflectivity imaging with ocean-bottom cable data. In: *SEG Technical Program Expanded Abstracts 2006.* s.l.:Society of Exploration Geophysicists, pp. 1560-1564.

Hornig-Kjarsgaard, I. et al., 1993. Geology, stratigraphy and volcanological evo- lution of the island of Stromboli, Aeolian arc, Italy. *Acta Vulcanologica,* Volume 3, pp. 21-68.

Imbo, G., 1935. Agitazione asmonica Vesuviano. *Annali dell'Osservatorio Vesuviano,* p. 163.

Jaggar, T. A., 1920. Seismometric investigations of the Hawaiian lava column. *Bulletin of the Seismological Society of America,* Volume 10, p. 204.

James, M., Lane, S. J., Chouet, B. & Gilbert, J. S., 2004. Pressure changes associated with the ascent and bursting of gas slugs in liquid-filled vertical and inclined conduits. *Journal of Volcanology and Geothermal Research,* 129(1), pp. 61-82.

Jaupart, C. & Vergniolle, S., 1989. The generation and collapse of a foam layer at the roof of a basaltic magma chamber. *Journal of Fluid Mechanics,* Volume 203, pp. 347-380.

Jin, A. & Aki, K., 1986. Temporal change in coda Q before the Tangshan Earthquake of 1976 and the Haicheng Earthquake of 1975. *Journal of Geophysical Research: Solid Earth,* 91(B1), pp. 665-673.

Kazahaya, K., Shinohara, H. & G., S., 1994. Excessive degassing of Izu-Oshima volcano: magma convection in a conduit. *Bulletin of Volcanology,* 56(3), pp. 207-216.

Kokelaar, P. & Romagnoli, C., 1995. Sector collapse, sedimentation and clast population evolution at an active island-arc volcano: Stromboli, Italy. *Bulletin of Volcanology,* 57(4), pp. 240-262.

Kondo, G. et al., 2019. Gas flux cyclic regime at an open vent magmatic column inferred from seismic and acoustic records. *Scientific Reports,* 9(1), pp. 2045-2322.

Konstantinou, K. & Schlindwein, V., 2003. Nature, wavefield properties and source mechanism of volcanic tremor: A review. *Journal of Volcanology and Geothermal Research,* Volume 119, pp. 161-187.

Larose, E., Derode, A., Campillo, M. & Fink, M., 2004. Imaging from one-bit correlations of wideband diffuse wave fields. *Journal of Applied Physics,* 95(12), pp. 8393-8399.

Larose, E. et al., 2006. Correlation of random wavefields: An interdisciplinary review. *Geophysics,* 71(4), pp. SI11-SI21.

Lecocq, T., Caudron, C. & Brenguier, F., 2014. MSNoise, a Python package for monitoring seismic velocity changes using ambient seismic noise. *Seismological Research Letters,* 85(3), pp. 715-726.

Leet, R. C., 1988. Saturated and subcooled hydrothermal boiling in groundwater flow channels as a source of harmonic tremor. *Journal of Geophysical Research: Solid Earth,* 93(B5), pp. 4835-4849.

Lin, F., Ritzwoller, M. H. & Snieder, R., 2009. Eikonal tomography: surface wave tomography by phase front tracking across a regional broad-band seismic array. *Geophysical Journal International,* 177(3), pp. 1091-1110.

Lobkis, O. I. & Weaver, R. L., 2001. On the emergence of the Green's function in the correlations of a diffuse field. *Journal of the Acoustical Society of America,* Issue 110, pp. 3011-3017.

Malcolm, A. E., Scales, J. A. & van Tiggelen, B. A., 2004. Extracting the Green function from diffuse, equipartitioned waves. *Physical Review E,* 70(1), p. 015601.

Ma, M. et al., 2008. Change of Patterns of Diseases and Medical Rescuing Measurement after Earthquake [J]. *Journal of Sun Yat-Sen University (Medical Sciences),* Volume 4.

Manga, M., 1996. Waves of bubbles in basaltic magmas and lavas. *Journal of Geophysical Research: Solid Earth,* 101(B8), pp. 17457-17465.

Marchetti, E. & Ripepe, M., 2005. Stability of the seismic source during effusive and explosive activity at Stromboli Volcano. *Geophysical Research Letters,* 32(3).

Marsella, M., Baldi, P., Coltelli, M. & Fabris, M., 2012. The morphological evolution of the Sciara del Fuoco since 1868: Reconstructing the effusive activity at Stromboli volcano. *Bulletin of Volcanology,* 74(1), pp. 231-248.

Matsumoto, S. et al., 2001. Temporal change in P-wave scatterer distribution associated with the M6.1 earthquake near Iwate volcano, northeastern Japan. *Geophysical Journal International,* 145(1), pp. 48-58.

McNutt, S. R., 2000. *Volcanic Seismicity, Chapter 63 of Encyclopedia of Volcanoes, Sigurdsson, H., B.* San Diego: Academic Press.

Mehta, K., Sheiman, J. L., Snieder, R. & Calvert, R., 2008. Strengthening the virtual-source method for time-lapse monitoring. *Geophysics,* 73(3), pp. S73-S80.

Mehta, K., Snieder, R. & Graizer, V., 2007. Extraction of near-surface properties for a lossy layered medium using the propagator matrix. *Geophysical Journal International,* 169(1), pp. 271-280.

Métrich, N., Bertagnini, A. & Di Muro, A., 2009. Conditions of Magma Storage, Degassing and Ascent at Stromboli: New Insights into the Volcano Plumbing System with Inferences on the Eruptive Dynamics. *Journal of Petrology,* 51(3), pp. 603-626.

Métrich, N., Bertagnini, A., Landi, P. & Rosi, M., 2011. Crystallization Driven by Decompression and Water Loss at Stromboli Volcano (Aeolian Islands, Italy). *Journal of Petrology,* 42(8), pp. 1471-1490.

Mikesell, T. D., Malcolm, A. E., Yang, D. & Haney, M. M., 2015. A comparison of methods to estimate seismic phase delays: numerical examples for coda wave interferometry. *Geophysical Journal International,* 202(1), pp. 347-360.

Minato, S. et al., 2011. Seismic interferometry using multidimensional deconvolution and crosscorrelation for crosswell seismic reflection data without borehole sources. *Geophysics,* 76(1), pp. SA19-SA34.

Miyazawa, M., Snieder, R. & Venkataraman, A., 2008. Application of seismic interferometry to extract P-and S-wave propagation and observation of shear-wave splitting from noise data at Cold Lake, Alberta, Canada. *Geophysics,* 73(4), pp. D35-D40.

Morse, P. M. & Ingard, K. U., 1968. Theoretical Acoustics. In: *McGraw-Hill.* New York: McGraw-Hill, pp. 582-588.

Nakata, N. et al., 2011. Shear wave imaging from traffic noise using seismic interferometry by cross-coherenceShear wave imaging from traffic noise. *Geophysics,* 76(6), pp. SA97-SA106.

Neuberg, J., Luckett, R., Ripepe, M. & Braun, T., 1994. Highlights from a seismic broadband array on Stromboli Volcano. *Geophysical Research Letters,* 21(9), pp. 749-752.

Nicholls, H. R. & Rinehart, J. S., 1967. Geophysical study of geyser action in Yellowstone National Park. *Journal of Geophysical Research,* 72(18), pp. 4651-4663.

Nishimura, T. et al., 2000. Source process of very long period seismic events associated with the 1998 activity of Iwate Volcano, northeastern Japan. *Journal of Geophysical Research: Solid Earth,* 108(B8), pp. 19135-19147.

Omori, F., 1911. On the eruption of U-su volcano. *Journal of the Meteorological Society of Japan. Ser. I,* 30(1), pp. 1-5.

Parfitt, E. A., 2004. A discussion of the mechanisms of explosive basaltic eruptions. *Journal of Volcanology and Geothermal Research,* 134(1), pp. 77-107.

Parfitt, E. A. & Wilson, L., 1995. Explosive volcanic eruptions—IX. The transition between Hawaiian-style lava fountaining and Strombolian explosive activity. *Geophysical Journal International,* 121(1), pp. 226-232.

Pasquarè, G., Francalanci, L., Garduno, V. H. & Tibaldi, A., 1993. Structure and geologic evolution of the Stromboli volcano, Aeolian Islands, Italy. *Acta Vulcanologica,* Volume 3, pp. 79-89.

Patrick, M. et al., 2007. Strombolian explosive styles and source conditions: Insights from thermal (FLIR) video. *Bulletin of Volcanology,* Volume 69, p. 769–784.

Patrick, M. R. et al., 2007. Strombolian explosive styles and source conditions: insights from thermal (FLIR) video. *Bulletin of Volcanology,* 69(7), pp. 769-784.

Perret, F. A., 1916. The lava eruption of Stromboli, summer-autumn, 1915. *American Journal of Science,* 42(4), pp. 443-463.

Pioli, L. et al., 2008. Explosive dynamics of violent Strombolian eruptions: The eruption of Parícutin Volcano 1943–1952 (Mexico). *Earth and Planetary Science Letters,* 271(1-4), pp. 359-368.

Pistolesi, M. et al., 2011. The 15 March 2007 explosive crisis at Stromboli volcano, Italy: Assessing physical parameters through a multidisciplinary approach. *Journal of Geophysical Research: Solid Earth,* 116(12).

Poupinet, G., Ellsworth, W. & Frechet, J., 1984. Monitoring Velocity Variations in the Crust Using Earthquake Doublets: An Application to the Calaveras Fault, California. *Journal of Geophysical Research,* Volume 89, pp. 5719-5831.

Prieto, G. A., F., L. J. & Beroza, G. C., 2009. Anelastic earth structure from the coherency of the ambient seismic field. *Journal of Geophysical Research,* Volume 114, p. B07303.

Ratdomopurbo, A. & Poupinet, G., 1995. Monitoring a temporal change of seismic velocity in a volcano: Application to the 1992 eruption of Mt. Merapi (Indonesia). *Geophysical Research Letters,* 22(7), pp. 0094-8276.

Rhie, J. & Romanowicz, B., 2004. Excitation of Earth's continuous free oscillations by atmosphere-ocean-seafloor coupling. *Nature,* 431(7008), pp. 552-556.

Richter, T., Sens-Schönfelder, C., Kind, R. & Asch, G., 2014. Comprehensive observation and modeling of earthquake and temperature-related seismic velocity changes in northern Chile with passive image interferometry. *Journal of Geophysical Research: Solid Earth,* 119(6), pp. 4747-4765.

Ripepe, M., 1996. Evidence for gas influence on volcanic seismic signals recorded at Stromboli. *Journal of volcanology and geothermal research,* 70(3-4), pp. 221-233.

Ripepe, M., Ciliberto, S. & Della Schiava, M., 2001. Time constraints for modeling source dynamics of volcanic explosions at Stromboli. *Journal of Geophysical Research: Solid Earth,* 106(B5), pp. 8713-8727.

Ripepe, M. et al., 2001. Seismic and infrasonic evidences for an impulsive source of the shallow volcanic tremor at Mt. Etna, Italy. *Geophysical Research Letters,* 28(6), pp. 1071-1074.

Ripepe, M. et al., 2015. Volcano seismicity and ground deformation unveil the gravity-driven magma discharge dynamics of a volcanic eruption. *Nature Communications,* 6(1), p. 6998.

Ripepe, M. et al., 2009. The onset of the 2007 Stromboli effusive eruption recorded by an integrated geophysical network. *Journal of Volcanology and Geothermal Research,* Volume 182, pp. 131-136.

Ripepe, M. & Gordeev, E., 1999. Gas bubble dynamics model for shallow volcanic tremor at Stromboli. *Journal of Geophysical Research: Solid Earth,* 104(B5), pp. 10639-10654.

Ripepe, M., Harris, A. & Carniel, R., 2002. Thermal, seismic and infrasonic evidences of variable degassing rates at Stromboli volcano. *Journal of Volcanology and Geothermal Research,* 118(3), pp. 285-297.

Ripepe, M. & Harris, A. J. L., 2008. Dynamics of the 5 April 2003 explosive paroxysm observed at Stromboli by a near-vent thermal, seismic and infrasonic array. *Geophysical Research Letters,* 35(7).

Ripepe, M. et al., in press. Ground deformation reveals the scale-invariant conduit dynamics driving explosive basaltic eruptions. *Nature Communications.*

Ripepe, M. et al., 2004. Seismic, acoustic, and thermal network monitors the 2003 eruption of Stromboli Volcano. *Eos, Transactions American Geophysical Union,* 85(35), pp. 329-332.

Ripepe, M. et al., 2005. Effusive to explosive transition during the 2003 eruption of Stromboli volcano. *Geology,* 33(5), pp. 341-344.

Ripepe, M. et al., 2017. Forecasting Effusive Dynamics and Decompression Rates by Magmastatic Model at Open-vent Volcanoes. *Scientific Reports,* Volume 7, p. 3885.

Robinson, S. P., 1999. Review of methods for low frequency transducer calibration in reverberant tanks.

Romagnoli, C., Kokelaar, P., Rossi, P. L. & Sodi, A., 1993. The submarine extension of Sciara del Fuoco feature (Stromboli isl.): morphologic characterization. *Acta Vulcanologica,* Volume 3, pp. 91-98.

Rosi, M., 1980. The Island of Stromboli. *Rendiconti Societa Italiana di Mineralogia e Petrologia,* Volume 36, pp. 345-368.

Rosi, M. et al., 2006. A case history of paroxysmal explosion at Stromboli: Timing and dynamics of the April 5, 2003 event. *Earth and Planetary Science Letters,* 243(3), pp. 594-606.

Rosi, M., Bertagnini, A. & Landi, P., 2000. Onset of the persistent activity at Stromboli Volcano (Italy). *Bulletin of Volcanology,* 62(4), pp. 294-300.

Rosi, M., Bertagnini, A. & Landi, P., 2000. Onset of the persistent activity at Stromboli Volcano (Italy). *Bulletin of Volcanology,* 62(4), pp. 294-300.

Rosi, M. et al., 2013. Stromboli Volcano, Aeolian Islands (Italy): Present eruptive activity and hazards. *Geological Society, London, Memoirs,* Volume 37, pp. 473-490.

Roux, P. & Fink, M., 2003. Green's function estimation using secondary sources in a shallow water environment. *Journal of the Acoustical Society of America,* Issue 113, pp. 1406-1416.

Roux, P. & Kuperman, W. A., 2004. Extracting coherent wave fronts from acoustic ambient noise in the ocean. *The Journal of the Acoustical Society of America,* 116(4), pp. 1995-2003.

Ruigrok, E., Campman, X., Draganov, D. & Wapenaar, K., 2010. High-resolution lithospheric imaging with seismic interferometry. *Geophysical Journal International,* 183(1), pp. 339-357.

Sakuma, S., 1957. Volcanic tremor at eruption Meakan-dake. *Journal of the Faculty of Science, Hokkaido University. Series 7,* 1(1).

Sassa, K., 1935. Volcanic micro-tremors and eruption-earthquakes. *Memoirs of the College of Science; Kyoto Imperial University, Series A,* Volume 18, pp. 255-293.

Schuster, G. T., Yu, J., Sheng, J. & Rickett, J., 2004. Interferometric/daylight seismic imaging. *Geophysical Journal International,* Issue 157, pp. 838-852.

Scott, D. R. & Stevenson, D. J., 1984. Magma solitons. *Geophysical Research Letters,* 11(11), pp. 1161-1164.

Self, S., 2006. The effects and consequences of very large explosive volcanic eruptions. *Philosophical Transactions of the Royal Society A: Mathematical, Physical and Engineering Sciences,* 364(1845), pp. 2073-2097.

Sens-Schönfelder, C. & Wegler, U., 2006. Passive image interferometry and seasonal variations of seismic velocities at Merapi Volcano, Indonesia. *Geophysical research letters,* 33(21).

Shapiro, N. M. & Campillo, M., 2004. Emergence of broadband Rayleigh waves from correlations of the ambient seismic noise. *Geophysical Research Letters,* 31(7).

Shapiro, N. M., Campillo, M., Stehly, L. & Ritzwoller, M. H., 2005. High-resolution surface-wave tomography from ambient seismic noise. *Science,* 307(5715), pp. 1615-1618.

Snieder, R., 2002. Coda wave interferometry and the equilibration of energy in elastic media. *Physical Review E,* 66(4), p. 046615.

Snieder, R., 2004. Extracting the Green's function from the correlation of coda waves: A derivation based on stationary phase. *Physical Review E,* 69(4), p. 046610.

Snieder, R., 2006. The Theory of Coda Wave Interferometry. *Pure and Applied Geophysics,* 163(2-3), pp. 455-473.

Snieder, R., 2007. Extracting the Green's function of attenuating heterogeneous acoustic media from uncorrelated waves. *The Journal of the Acoustical Society of America,* 121(5), pp. 2637-2643.

Snieder, R. & Safak, E., 2006. Extracting the building response using seismic interferometry: Theory and application to the Millikan Library in Pasadena, California. *Bulletin of the Seismological Society of America,* Volume 96, pp. 586-598.

Snieder, R., Van Wijk, K., Haney, M. & Calvert, R., 2008. Cancellation of spurious arrivals in Green's function extraction and the generalized optical theorem. *Physical Review E,* 78(3), p. 036606.

Snieder, R., Wapenaar, K. & Wegler, U., 2007. Unified Green's function retrieval by cross-correlation; connection with energy principles. *Physical Review E,* 75(3), p. 036103.

Stehly, L., Campillo, M., Froment, B. & Weaver, R. L., 2008. Reconstructing Green's function by correlation of the coda of the correlation (C3) of ambient seismic noise. *Journal of Geophysical Research: Solid Earth,* 113(B11).

Steinberg, G. S. & Steinberg, A. S., 1975. On possible causes of volcanic tremor. *Journal of geophysical research,* 80(11), pp. 1600-1604.

Stevenson, D. & Blake, S., 1998. Modelling the dynamics and thermodynamics of volcanic degassing. *Bulletin of Volcanology,* Volume 60, pp. 307-317.

Thomas, N., Tait, S. & Koyaguchi, T., 1993. Mixing of stratified liquids by the motion of gas bubbles: application to magma mixing. *Earth and Planetary Science Letters,* 115(1), pp. 161-175.

Tibaldi, A., 2001. Multiple sector collapses at stromboli volcano, Italy: how they work. *Bulletin of Volcanology,* 63(2), pp. 112-125.

Tibaldi, A., 2003. Influence of cone morphology on dykes, Stromboli, ItalyTibaldi. *Journal of Volcanology and Geothermal Research,* 126(1-2), pp. 79-95.

Tibaldi, A., Corazzato, C., Marani, V. & Gamberi, F., 2009. Subaerial-submarine evidence of structures feeding magma to Stromboli Volcano, Italy, and relations with edifice flank failure and creep. *Tectonophysics,* 469(1-4), pp. 112-136.

Tibaldi, A., Pasquarè, G., Francalanci, L. & H., G. V., 1994. *Collapse type and recurrence at Stromboli volcano, associated volcanic activity, and sea level changes.* Roma, Accademia Nazionale Dei Lincei, pp. 143-151.

Tommasi, P. et al., 2005. The Landslide Sequence Induced by the 2002 Eruption at Stromboli Volcano. In: *Landslides..* Berlin: Springer, pp. 251-258.

Trampert, J., Cara, M. & Frogneux, M., 1993. SH propagator matrix and Qs estimates from borehole- and surface- recorded earthquake data. *Geophysical Journal International,* 112(2), pp. 290-299.

Valade, S. et al., 2016. Tracking dynamics of magma migration in open-conduit systems. *Bulletin of Volcanology,* Volume 78.

Vasconcelos, I. et al., 2008. Drill bit noise illuminates the San Andreas Fault. *Eos, Transactions American Geophysical Union,* 89(38), pp. 349-349.

Ventura, G., 2013. Kinematics of the Aeolian volcanism (Southern Tyrrhenian Sea) from geophysical and geological data. In: *The Aeolian Islands Volcanoes.* s.l.:Geological Society, London, Memoirs, pp. 3-11.

Vergniolle, S., Brandeis, G. & Mareschal, J.-C., 1996. Strombolian explosions: 2. Eruption dynamics determined from acoustic measurements. *ournal of Geophysical Research: Solid Earth,* 101(89), pp. 20449-20466.

Wapenaar, .. & Fokkema, J. a. S. R., 2005. Retrieving the Green's function in an open system by cross correlation: A comparison of approaches (L). *The Journal of the Acoustical Society of America,* 118(5), pp. 2783-2786.

Wapenaar, K., 2004. Retrieving the elastodynamic Green's function of an arbitrary inhomogeneous medium by cross correlation. *Physical review letters,* 93(25), p. 254301.

Wapenaar, K. et al., 2010. Tutorial on seismic interferometry: Part 1 - Basic principles and applications. *Geophysics,* 75(5), pp. 195-209.

Wapenaar, K. & Fokkema, J., 2006. Green's function representations for seismic interferometry. *Geophysics,* 71(4), pp. SI33-SI46.

Wapenaar, K., Slob, E. & Snieder, R., 2008. Seismic and electromagnetic controlled-source interferometry in dissipative media. *Geophysical Prospecting,* Volume 56, pp. 419-434.

Weaver, R. L., 2008. Ward identities and the retrieval of Green's functions in the correlations of a diffuse field. *Wave Motion,* 45(5), pp. 596-604.

Weaver, R. L. & Lobkis, O. I., 2001. Ultrasonics without a Source: Thermal Fluctuation Correlations at MHz Frequencies. *Physical Review Letters,* 87(13), pp. 134301-134305.

Wilson, L. & Head III, J. W., 1981. Ascent and eruption of basaltic magma on the Earth and Moon. *Journal of Geophysical Research: Solid Earth,* 86(B4), pp. 2971-3001.

Wunderman, R., 2014. Global Volcanism Program, 2014. Report on Kelut (Indonesia). *Bulletin of the Global Volcanism Network,* 39(2).